NTNU – Trondheim
Norwegian University of
Science and Technology

Model-based stochastic-deterministic State and Force Estimation using Kalman filtering with Application to Hanko-1 Channel Marker

Øyvind Wiig Petersen

Civil and Environmental Engineering
Submission date: June 2014
Supervisor: Ole Andre Øiseth, KT
Co-supervisor: Torodd Skjerve Nord, BAT

Norwegian University of Science and Technology
Department of Structural Engineering

MASTEROPPGAVE 2014

Modellbasert stokastisk-deterministisk tilstand- og kraftidentifisering ved bruk av Kalmanfilter for leilykten Hanko-1

Model-based stochastic-deterministic state and force estimation using Kalman filtering with application to Hanko-1 channel marker

Konstruksjoner utsatt for is i bevegelse kan bli satt i isinduserte svingninger. Dette skyldes at knusingen av isen mot konstruksjonen gir en dynamisk last. Denne lasten er avhengig av en rekke parametere, som tårnets geometri, isens hastighet, isens tykkelse, og klimatiske forhold. Det eksisterer ingen modeller som gir en fullstendig beskrivelse av den dynamiske islasten. Direkte måling av islasten er vanskelig siden utsiden av konstruksjonen blir utsatt for store krefter og mye slitasje.

Denne oppgaven dreier seg om å bruke et Kalmanfilter til å bestemme kreftene som virker på konstruksjonen.

Oppgaven bør inneholde følgende temaer:

- Grunnleggende teori for invers kraftidentifisering
- Modellering av leilykten
- Identifisering av islaster

Veiledere: Torodd Skjerve Nord, Ole Andre Øiseth

Besvarelsen skal leveres til Institutt for konstruksjonsteknikk innen 10. juni 2014.

Abstract

Force identification in structural dynamics is an inverse problem concerned with finding loads from measured structural response. The main objective of this thesis is to perform and study state (displacement and velocity) and force estimation by Kalman filtering. Theory on optimal control and state-space models are presented, adapted to linear structural dynamics. Accommodation for measurement noise and model inaccuracies are attained by stochastic-deterministic coupling. Explicit requirements for discrete time-invariant steady filter convergence are derived. From a finite element model and measurement data, unbiased estimation of state and force history is performed by an augmented Kalman filter, based on minimizing error variance.

A numerical example on a system with two degrees of freedom displays adequate filtering capabilities. Experimental validation is performed on a simply supported beam instrumented with accelerometer and three strain gauges. The studies demonstrate successful identification of impact forces with both collocated and non-collocated sensors. The corresponding state estimation displays good accuracy. Limiting the number of measurements is tested. The minimal observation setup (one accelerometer and one strain gauge) is analytically stable, but results are found to be significantly deteriorated, even with collocation. Moreover the influence of model errors is investigated, imposed as random contributions in mass and stiffness matrices. The estimation of impact forces and states show fair robustness against moderate mass and stiffness deviations.

A short case study on the offshore Hanko channel marker is presented, exposed to moving sea ice. A finite element model is created, instrumented with a tiltmeter and three accelerometers. Numerical simulations show identification of ice forces is viable, but heavily relies on the model representation accuracy.

Sammendrag

Kraftidentifisering i konstruksjonsdynamikk er et invers problem hvor laster finnes fra målt konstruksjonsrespons. Hovedformålet i denne avhandlingen er å studere estimering av kraft og tilstand (forskyvning og hastighet) ved bruk av Kalmanfilter. Optimal kontrollteori og tilstandsrom-modeller presenteres, tilpasset lineær konstruksjonsdynamikk. Målestøy og unøyaktighet i modeller imøtekommes med innføring av en stokastisk-deterministisk systembeskrivelse. Eksplisitte kriterier for stabil konvergens i et diskret tids-invariant filter utledes. En elementmodell sammen med måledata gir via et utvidet Kalmanfilter forventningsrette estimat av tilstands- og krafthistorikk. Estimatet er basert på minimum varians i forventet feil.

Numeriske eksempler på et to-frihetsgradsystem viser adekvat effektivitet i filtrering. Eksperimentell verifisering av metoden er gjort på en fritt opplagt bjelke, instrumentert med akselerometer og tre strekklapper. Undersøkelsene demonstrerer vellykket identifisering av støtkrefter både med kolokaliserte og ikke-kolokaliserte sensorer. Tilhørende tilstandsestimat har høy nøyaktighet. Effekten av å redusere antall målinger studeres. I en minimal konfigurasjon (ett akselerometer og én strekklapp) er identifiseringen fortsatt analytisk stabil, men resultatene er signifikant forringet, selv med kolokaliserte sensorer. Videre undersøkes påvirkningen av modellfeil på resultatene. Manipulering av masse- og stivhetsmatrisene utføres ved bruk av tilfeldig støy. Filteret viser robusthet mot modellfeil av moderat størrelse, estimert støtkraft samt tilstand er i liten grad påvirket.

Til slutt presenteres en saksstudie av leilykten Hanko utenfor Finlands kyst, utsatt for krefter fra is i bevegelse. En elementmodell etableres, instrumentert med ett tiltmeter og tre akselerometer. Numeriske simuleringer viser at identifisering av iskreftene på lykten er mulig, men er svært avhengig av elementmodellens nøyaktighet.

Preface

This master thesis is the final dissertation for the M.Sc. degree at the Department of Structural Engineering at the Norwegian University of Science and Technology (NTNU), completing the five year study program in spring 2014.

Throughout the semester I have received generous support from PhD Candidate Torodd Skjerve Nord. My results would not have been possible without his helpful assistance, source code contributions and constructive discussions on the subject.

I would like to thank Associate Professor Ole Andre Øiseth for his guidance and also convincing me to continue my education further in a PhD program. I look forward to starting and advancing my work further.

Øyvind Wiig Petersen

June 10, 2014

Contents

Acronyms

DOF degree of freedom

FE finite element

FRF frequency response function

LS least squares

MDOF multi degree of freedom

MIMO multiple input multiple output

MLE maximum likelihood estimation

MSE mean square error

MVU minimum-variance unbiased

ODE ordinary differential equation

PDF probability density function

RMS root mean square

SDOF single degree of freedom

SG strain gauge

SSE sum of squared errors

Nomenclature

Variables

$m,\ c,\ k$	Mass, damping and stiffness coefficients
$\boldsymbol{M},\ \boldsymbol{C},\ \boldsymbol{K}$	Mass, damping and stiffness matrices
$\boldsymbol{A},\ \boldsymbol{B},\ \boldsymbol{G},\ \boldsymbol{J},\ \boldsymbol{F}$	State-space system matrices
$\boldsymbol{A}_a,\ \boldsymbol{G}_a$	Augmented state-space system matrices
$\boldsymbol{S}_d,\ \boldsymbol{S}_v,\ \boldsymbol{S}_a$	Measurement selection matrices
$\boldsymbol{S}_p$	Force application matrix
$\boldsymbol{x}, \boldsymbol{x}^a$	State vector and augmented state vector
$\boldsymbol{y}$	Observation vector
$\boldsymbol{p}$	Force vector
$\boldsymbol{u}$	Degrees of freedom vector
$\boldsymbol{w},\ \boldsymbol{v},\ \boldsymbol{\eta},\ \boldsymbol{\zeta}$	Noise vectors
$\boldsymbol{Q},\ \boldsymbol{R},\ \boldsymbol{S},\ \boldsymbol{Q}_a$	Noise covariance matrices
$\boldsymbol{e}^{\boldsymbol{p}}$	Prior (prediction) estimate error
$\boldsymbol{e}^{\boldsymbol{f}}$	Posterior (filter) estimate error
$\boldsymbol{P}_{k\|k-1}$	Prior estimate error covariance matrix
$\boldsymbol{P}_{k\|k}$	Posterior estimate error covariance matrix
$\boldsymbol{L}$	Kalman gain
$\boldsymbol{I}$	Identity matrix
Δt	Finite time increment
f_i	Natural frequency no. i
f_s	Sampling frequency

n_{DOF}	No. of degrees of freedom
n_s	No. of states
n_p	No. of forces
n_d	No. of observations
λ	Transmission zero

Notations

$z,\ Z$	Scalar
$\boldsymbol{z}$	Vector
$\boldsymbol{Z}$	Matrix
Z_{ij}	Element in row i and column j of matrix $\boldsymbol{Z}$
$\mathcal{N}(\mu, \Sigma)$	Normal distribution with mean μ and (co)variance Σ
$E[X]$	Expectancy of X
$Cov[X]$	Covariance of X
$\sigma_X,\ \sigma(X)$	Standard deviation of X
$S_\sigma(X)$	Unbiased sample standard deviation of X
$\mathrm{tr}(\boldsymbol{X})$	Trace of matrix $\boldsymbol{X}$
$\det(\boldsymbol{X})$	Determinant of matrix $\boldsymbol{X}$
$\dot{s}$	Time derivative of s
s_k	Variable s evaluated at time $t_k = k\Delta t$
$\hat{s}$	Estimate of s
$\hat{s}_{k\|k-1}$	Prior (prediction) estimate of s
$\hat{s}_{k\|k}$	Posterior (filter) estimate of s
$\equiv$	Equal by definition

List of Figures

List of Tables

Chapter 1

Introduction

1.1 Motivation for research

Identification of loads is an area of interest within the field of structural dynamics. Structural design and related codes, dynamic analysis, risk and reliability assessment all rely upon knowledge and characterization of external loads. Loads from wind, ice, waves, earthquake, impact forces and vehicle/bridge interaction are cases receiving attention in the academic scene. The past fifty years have seen increasing research and advancement in techniques. Measuring loads directly is often not feasible due to structure size, large force magnitudes and practical instrumentation difficulties in general [1, 2], whereas measuring structural response is far more convenient. This opens up for the problem of identifying loads using measured response, which comprise the core matter in this dissertation. This thesis is written in collaboration with international research center SAMCoT (Sustainable Arctic Marine and Coastal Technology). Ice mechanics comprise an entire field of civil engineering, dealing with ice-structure interaction. Offshore structures located in Arctic zones face challenges being exposed to sea ice in motion. With Arctic exploration and development advancing, especially in the interest of the hydrocarbon resource industry, there is a desire to study and understand the behavior of structures subjected to ice actions. This calls for identification of ice loads, playing an important role in the ice-structure analysis. Observational studies have been performed worldwide on Arctic structures, but many related issues are not fully understood and remain uninvestigated.

1.2 Scope of thesis and approach to study

In the next chapter we aim to derive and present a comprehensive theoretical basis for the methods to be applied later. We also seek to review how the general theory adapts to structural dynamics, currently not extensively explored. This will be followed by numerical and experimental studies of force identification. The methods will be studied meticulously to gauge and refine their performance. The combined theoretical and experimental findings should make important contributions to the current understanding. The ultimate goal is to perform simulations of ice force estimation on the Hanko channel marker, located in the Gulf of Bothnia. Despite the existence of interdiscipline schemes coupling ice material models and structural dynamics, detailed considerations of ice behavior are disregarded. Research on ice material mechanics is left for others, rather focusing on the structural aspect. For this reason most of the theory and methods will generally apply to any force identification, regardless of its nature. The author hopes the methods can be further developed and new results unfolded. If techniques prove applicable, they could be employed on a diverse range of dynamic cases. Methods are naturally of greater value if applicable to a broader field of utility.

This thesis will cover theory from the field of optimal control and state-space models, which may be unfamiliar to structural engineers. This field has existed about 50 years and during this time been developed to be suitable for a variety of applications, in the later years also structural dynamics. The state-space formulation has advantages making it especially suitable for integrating classical linear dynamics with stochastic features. The methods to be presented are mostly based on the work of others, although some new ideas will be explored upon. The bulk part of the methods can be straight forward implemented, but detailed usage and fine tuning requires a comprehensive understanding of the underlying theory. This especially applies to their statistical foundation. Even though much of this part is not directly discussed in analysis, a deep comprehension will nevertheless provide a more solid platform for decision-making, improving algorithms and assessment of results. Much the work effort lies in reviewing the fundamental basis. Since most civil engineers, including the author, do not have an inherent background in sta-

tistical approaches to engineering, stochastic processes and state-space problems, these subjects will be elaborated upon thoroughly in the theory. The reader is assumed to already be familiar with conventional mechanics and structural dynamics. Less explanatory emphasis is given on these topics even though their importance remains vital.

Chapter 2

Theory

2.1 The inverse problem and identification techniques

The idea of force identification is using structural response combined with a system model to find loads. This is known as an inverse problem, in contrast to the classic design case of finding response from a given load, called a forward problem. Inverse problems receive much interest in general engineering and have been studied thoroughly, as analogous problems appear in other fields, e.g. heat conduction and signal processing. The inversion requires a mathematical relation connecting the measured quantities and the unknown variables, often via differential equations. Another kind of inverse problem, namely system identification from known response and force will not be covered here. In addition to the response, the system model and boundary conditions will throughout this thesis generally be treated as known.

Principles of classic force identification are briefly mentioned here. Methods can usually be divided into time domain methods and frequency domain methods. Formulations in the time domain are usually done by equilibrium equations on and relies on time sampled observations [3]. Deconvolution of an impulse response integral can be employed to solve for a force history. Conventional deconvolution is severely prone to computational erroneousness [4], thus requiring improved methods to give satisfactory results. A frequency domain solution is classically obtained by a Fourier transformation. This assembles a frequency response function (FRF) matrix, relating system response to input load fre-

quencies. The output, namely structural response, is given together with its frequency spectrum. From this, one can apply the inverse FRF matrix to find the corresponding force spectrum. An inverse Fourier transform then produces the force history. Unfortunately, the FRF matrix inversion is generally ill-conditioned, especially close to resonant frequencies [5]. In fact, the inverse problem itself is in practice often ill-posed, and ordinary numerical methods fail to treat the problem sufficiently. A variety of measures for stability improvement have been developed, but these fall outside the scope of this thesis.

In classical mechanics theory, which can be regarded as deterministic, one has absolute belief in measurements and the system description. That is, their values are believed to be unconditionally true. Stochastic methods rather employes a statistical description of the system, in practice opening for the possibility of imperfections and considering their influence on the solution. As a consequence, variables are not necessarily of absolute value, but instead defined by some statistical properties. The concept of noise can then be introduced and handled adequately. Later, this concept will be integrated by coupling classical dynamics with statistics arriving at a so-called stochastic-deterministic description of a problem.

2.2 State-space models

2.2.1 Introduction

State-space techniques are a branch of optimal control, a field of engineering analyzing dynamic systems with inputs and outputs. First developed in the 1960s, state-space techniques have since successfully been adapted to numerous applications, among others classical mechanics, electromechanics, cybernetics, biology, fluid mechanics and economics. The state-space representation operates by taking in and interpreting system inputs, then manipulating the system by imposing upon it a desired behavior through a control phase, ultimately leading to system outputs. In the field of structural dynamics, system outputs often include displacements, rotations, strains or stresses and their time derivatives, while inputs are forces or moments. The control phase algorithm is comprised of or derived

from a set of differential equations or relations describing system dynamics. Examples of this include force equilibrium or Euler-Lagrange equations. Although methods for dealing with non-linearity exist, the content of this thesis is limited to linear systems.

The majority of notations and conventions of the entire state-space formulation to be presented are adopted and patterned after Lourens [6].

2.2.2 Classical state-space formulation

The set of equilibrium equations in a linear dynamic system with n_{DOF} degrees of freedom (DOFs) is commonly formulated as:

$$\boldsymbol{M}\ddot{\boldsymbol{u}}(t) + \boldsymbol{C}\dot{\boldsymbol{u}}(t) + \boldsymbol{K}\boldsymbol{u}(t) = \boldsymbol{f}(t) = \boldsymbol{S_p}\boldsymbol{p}(t) \tag{2.2.1}$$

The n_{DOF}-dimensional vector $\boldsymbol{u}$ contains the DOFs, generally displacements or rotations. $\boldsymbol{M}$, $\boldsymbol{C}$ and $\boldsymbol{K}$ represents the mass, damping and stiffness matrices. The external force $\boldsymbol{f}$ is factorized into $\boldsymbol{S_p}$ and $\boldsymbol{p}$. $\boldsymbol{S_p}$ is a time-independent force application matrix assigning the force histories contained in $\boldsymbol{p}$ to the designated DOFs. This is of convenience allowing $\boldsymbol{p}$ later to be identified having less elements than $\boldsymbol{f}$. The number of unknown forces is taken as n_p.

The *state* vector $\boldsymbol{x}(t)$ defined in Eq. (2.2.2) can be regarded as information on the system behavior at an instant. Its dimension n_s is $2 \times n_{DOF}$. The relations in Eq. (2.2.3) can be derived from Eq. (2.2.1) together with the redundant equation $\boldsymbol{M}\dot{\boldsymbol{u}} - \boldsymbol{M}\dot{\boldsymbol{u}} = \boldsymbol{0}$. The symmetric matrices $\boldsymbol{P}$ and $\boldsymbol{Q}$ in Eq. (2.2.4) contains system properties only.

$$\boldsymbol{x}(t) = \begin{pmatrix} \boldsymbol{u}(t) \\ \dot{\boldsymbol{u}}(t) \end{pmatrix} \tag{2.2.2}$$

$$\boldsymbol{P}\dot{\boldsymbol{x}}(t) + \boldsymbol{Q}\boldsymbol{x}(t) = \begin{pmatrix} \boldsymbol{S}_p \\ \boldsymbol{0} \end{pmatrix} \boldsymbol{p}(t) \tag{2.2.3}$$

$$\boldsymbol{P} = \begin{bmatrix} \boldsymbol{C} & \boldsymbol{M} \\ \boldsymbol{M} & \boldsymbol{0} \end{bmatrix} \quad , \quad \boldsymbol{Q} = \begin{bmatrix} \boldsymbol{K} & \boldsymbol{0} \\ \boldsymbol{0} & -\boldsymbol{M} \end{bmatrix} \tag{2.2.4}$$

Solving for $\dot{\boldsymbol{x}}(t)$, the state equation on continuous form Eq. (2.2.5) is obtained. $\boldsymbol{A}_c$ and $\boldsymbol{B}_c$ in Eq. (2.2.6) follow from blockwise matrix inversion. Upon inspection one now sees the original system Eq. (2.2.1) of n_{DOF} second order ordinary differential equations (ODEs) is transferred into a system of $2 \times n_{DOF}$ coupled first order ODEs [7].

$$\dot{\boldsymbol{x}}(t) = \boldsymbol{A_c}\boldsymbol{x}(t) + \boldsymbol{B_c}\boldsymbol{p}(t) \tag{2.2.5}$$

$$\boldsymbol{A}_c = \begin{bmatrix} \boldsymbol{0} & \boldsymbol{I} \\ -\boldsymbol{M^{-1}K} & -\boldsymbol{M^{-1}C} \end{bmatrix} \quad , \quad \boldsymbol{B}_c = \begin{bmatrix} \boldsymbol{0} \\ -\boldsymbol{M^{-1}S}_p \end{bmatrix} \tag{2.2.6}$$

Accelerations, velocities and displacements are assumed to be measured at discrete locations and collected in the vector $\boldsymbol{y}(t)$, linked to original DOFs through selection matrices $\boldsymbol{S}_a, \boldsymbol{S}_v$ and $\boldsymbol{S}_d$ as stated in Eq. (2.2.7). Options of including strain gauge (SG) measurements through finite element (FE) strain-displacement formulations are feasible if strain is linear in displacements, supported by both Euler-Bernoulli and Timoshenko beam theory. Measurements are also referred to as *observations*. The number of system observations (and the dimension of $\boldsymbol{y}$) is n_d.

$$\boldsymbol{y}(t) = \boldsymbol{S}_a\ddot{\boldsymbol{u}}(t) + \boldsymbol{S}_v\dot{\boldsymbol{u}}(t) + \boldsymbol{S}_d\boldsymbol{u}(t) \tag{2.2.7}$$

Rewriting Eq. (2.2.1) and (2.2.7), the observation equation on continuous form Eq. (2.2.8), along with (2.2.9) are obtained. The equation pair Eq. (2.2.5) and (2.2.8) together constitute the continuous state-space representation of a linear system. The block diagram in Fig. 2.1 shows a graphic interpretation of the time-continuous progression. Intelligibly, the state-space formulation merely provides the state variables as function of time (output) for a given initial state and force history (input). The calculated state variables can then serve as an initial state at an advanced point in time, repeating the process.

$$\boldsymbol{y}(t) = \boldsymbol{G}_c\boldsymbol{x}(t) + \boldsymbol{J}_c\boldsymbol{p}(t) \tag{2.2.8}$$

$$\boldsymbol{G}_c = \begin{bmatrix} \boldsymbol{S}_d - \boldsymbol{S}_a\boldsymbol{M}^{-1}\boldsymbol{K} & \boldsymbol{S}_v - \boldsymbol{S}_a\boldsymbol{M}^{-1}\boldsymbol{C} \end{bmatrix} \quad , \quad \boldsymbol{J}_c = \boldsymbol{S}_a\boldsymbol{M}^{-1}\boldsymbol{S}_p \tag{2.2.9}$$

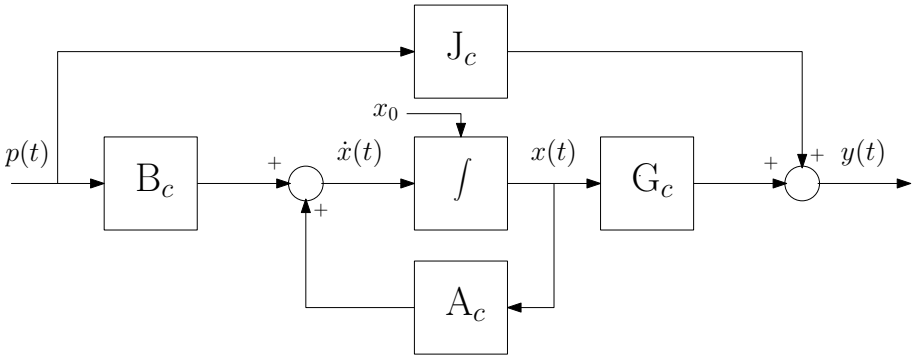

Figure 2.1: Block diagram of continuous state-equation process. Created from Williams II and Lawrence [7].

Numerically, a discrete formulation is advantageous, since measurements in practice must be sampled at distinct points in time. Dividing the time domain into finite time increments Δt, the state response at time $t_k = k\Delta t$ can be recursively calculated from a known force history and specified initial conditions. The subscript notation $r_k = r(t_k)$ for time-varying discrete variables are hereafter used. In existing literature Eq. (2.2.5) is often solved arriving at the state response expressed in Eq. (2.2.10), or an equivalent form. This discretization assumes zero-order hold on $\boldsymbol{p}$ (i.e. forces is kept constant throughout each time step). This can unfortunately prove inaccurate if the sampling frequency is low compared to the force rate, e.g. in the case of an impact load. As measure of improvement, we put forward a solution based on a first order hold on $\boldsymbol{p}$, whose complete derivation is done in Appendix A. The solution in Eq. (2.2.11) effectively adds a correction term proportional to the average force rate.

$$\boldsymbol{x}_{k+1} = \boldsymbol{A}\boldsymbol{x}_k + \boldsymbol{B}\boldsymbol{p}_k \tag{2.2.10}$$

$$\boldsymbol{x}_{k+1} = \boldsymbol{A}\boldsymbol{x}_k + \boldsymbol{B}\boldsymbol{p}_k + \boldsymbol{F}\frac{(\boldsymbol{p}_{k+1} - \boldsymbol{p}_k)}{\Delta t} \tag{2.2.11}$$

$$\boldsymbol{A} = e^{\boldsymbol{A}_c\Delta t} \quad , \quad \boldsymbol{B} = (\boldsymbol{A} - \boldsymbol{I})\boldsymbol{A}_c^{-1}\boldsymbol{B}_c \quad , \quad \boldsymbol{F} = \boldsymbol{A}_c^{-1}(\boldsymbol{B} - \boldsymbol{B}_c\Delta t) \tag{2.2.12}$$

$$\boldsymbol{y}_k = \boldsymbol{G}\boldsymbol{x}_k + \boldsymbol{J}\boldsymbol{p}_k \quad , \quad \boldsymbol{G} = \boldsymbol{G}_c \quad , \quad \boldsymbol{J} = \boldsymbol{J}_c \tag{2.2.13}$$

Computational load is virtually unaffected since the matrix $\boldsymbol{F}$ need only be calculated initially. The notation $e^{\boldsymbol{Z}}$ is the matrix exponential $\sum_{k=0}^{\infty} \frac{\boldsymbol{Z}^k}{k!}$, converging unconditionally. Using the matrix exponential for solving is preferable over other methods such as central differences or Newmark schemes, as it proves to give better accuracy and stability [6]. The discrete observation history in Eq. (2.2.13) attains a form congruent to the continuous case.

2.2.3 Stochastic-deterministic considerations

In a fully deterministic system, the output can be calculated exactly (up to numeric precision) given an initial state. In reality this approach fails as systems cannot be considered fully deterministic. All factors influencing the system cannot be identified, thus rendering the system description erroneous. The ability to handle noise is also of great importance, as all type of measurements will be contaminated with noise or have uncertainties. This advocates the introduction of a *stochastic-deterministic model*.

A legitimate presumption is noise not showing any predictable dynamic pattern, as this would indicate linear dynamic relations ignored in the system description [8]. Noise is therefore taken be white, i.e. its frequency spectrum is completely flat. To satisfy unpredictability, noise is assumed to arise from a stochastic process. The most common noise characterization is zero mean Gaussian (normal) distributed, also called Gaussian white noise. Mathematically, a discrete white noise vector $\boldsymbol{\epsilon}$ can be expressed as [9]:

$$\boldsymbol{E}[\boldsymbol{\epsilon}_k] = \boldsymbol{0}$$

$$\boldsymbol{E}[\boldsymbol{\epsilon}_k \boldsymbol{\epsilon}_l^T] = \begin{cases} \boldsymbol{0} & k \neq l \\ \boldsymbol{\Sigma} & k = l \end{cases}$$

This translates as zero mean and zero autocovariance, except for the case of zero time-shift. Furthermore, $\boldsymbol{\Sigma}$ is often adopted as diagonal only [10, 11], implying no correlation between the individual elements of $\boldsymbol{\epsilon}_k$ within time k.

The stochastic-deterministic state-space system Eq. (2.2.14) and (2.2.15) are identical to the classical discretization Eq. (2.2.11) and (2.2.13), except for added noise. The model noise $\boldsymbol{w}_k$ added to the state accounts for the fact that the system description is imperfect. Similarly, $\boldsymbol{v}_k$ is the observation noise, attributed to inaccuracies in measurements. These noise processes are white and accordingly have the properties stated above. Their vector covariances are defined as $\boldsymbol{E}[\boldsymbol{w}_k\boldsymbol{w}_k^T] = \boldsymbol{Q}$ and $\boldsymbol{E}[\boldsymbol{v}_k\boldsymbol{v}_k^T] = \boldsymbol{R}$.

$$\boldsymbol{x}_{k+1} = \boldsymbol{A}\boldsymbol{x}_k + \boldsymbol{B}\boldsymbol{p}_k + \boldsymbol{F}\frac{(\boldsymbol{p}_{k+1} - \boldsymbol{p}_k)}{\Delta t} + \boldsymbol{w}_k \tag{2.2.14}$$

$$\boldsymbol{y}_k = \boldsymbol{G}\boldsymbol{x}_k + \boldsymbol{J}\boldsymbol{p}_k + \boldsymbol{v}_k \tag{2.2.15}$$

2.2.4 Augmented state-space formulation

Up till now, the input forces has been treated as well-known. Since the aim is to identify forces, the augmented state-space model is introduced, as presented by Lourens [6]. The classic state and the force together constitute the *augmented state* vector $\boldsymbol{x}^a$ as expressed in Eq. (2.2.16). The change in force over one time step is assumed to be a realization of the white noise process $\boldsymbol{\eta}_k$, with vector covariance $\boldsymbol{E}[\boldsymbol{\eta}_k\boldsymbol{\eta}_k^T] = \boldsymbol{S}$. Otherwise known as a Gaussian random walk, the precept in Eq. (2.2.17) allows for an easy probabilistic characterization, but has shortcomings. The force is not random in a purely statistical sense, but rather a realization of underlying processes with a distinct pattern governed by laws of psychics [4].

$$\boldsymbol{x}_k^a = \begin{bmatrix} \boldsymbol{x}_k \\ \boldsymbol{p}_k \end{bmatrix} \tag{2.2.16}$$

$$\boldsymbol{p}_{k+1} = \boldsymbol{p}_k + \boldsymbol{\eta}_k \tag{2.2.17}$$

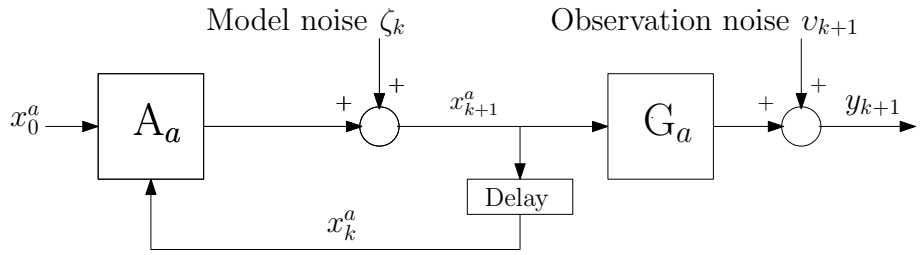

Figure 2.2: Block diagram of time-discrete stochastic augmented state system.

The transformation from the classic to the augmented model unveils the new time discrete stochastic relations Eq. (2.2.18) and (2.2.19), also schematized in Fig. 2.2.

$$\boldsymbol{x}_{k+1}^a = \boldsymbol{A}_a \boldsymbol{x}_k^a + \boldsymbol{\zeta}_k \quad , \quad \boldsymbol{A}_a = \begin{bmatrix} \boldsymbol{A} & \boldsymbol{B} \\ \boldsymbol{0} & \boldsymbol{I} \end{bmatrix} \quad , \quad \boldsymbol{\zeta}_k = \begin{bmatrix} \boldsymbol{w}_k + \frac{\boldsymbol{F}}{\Delta t}\boldsymbol{\eta}_k \\ \boldsymbol{\eta}_k \end{bmatrix} \tag{2.2.18}$$

$$\boldsymbol{y}_k = \boldsymbol{G}_a \boldsymbol{x}_k^a + \boldsymbol{v}_k \quad , \quad \boldsymbol{G}_a = \begin{bmatrix} \boldsymbol{G} & \boldsymbol{J} \end{bmatrix} \tag{2.2.19}$$

The covariance properties of the augmented state noise $\boldsymbol{\zeta}_k$ is collected in the matrix $\boldsymbol{Q}_a$:

$$\begin{aligned} &\boldsymbol{Q}_a = \boldsymbol{E}[\boldsymbol{\zeta}_k \boldsymbol{\zeta}_k^T] = \\ &\boldsymbol{E}\begin{bmatrix} \frac{\boldsymbol{F}}{\Delta t}\boldsymbol{\eta}_k + \boldsymbol{w}_k \\ \boldsymbol{\eta}_k \end{bmatrix} \begin{bmatrix} (\frac{\boldsymbol{F}}{\Delta t}\boldsymbol{\eta}_k)^T + \boldsymbol{w}_k^T & \boldsymbol{\eta}_k^T \end{bmatrix} = \begin{bmatrix} \boldsymbol{Q} + \frac{\boldsymbol{F}}{\Delta t}\boldsymbol{S}\frac{\boldsymbol{F}^T}{\Delta t} & \frac{\boldsymbol{F}}{\Delta t}\boldsymbol{S} \\ \boldsymbol{S}\frac{\boldsymbol{F}^T}{\Delta t} & \boldsymbol{S} \end{bmatrix} \end{aligned} \tag{2.2.20}$$

Even though $\boldsymbol{\eta}_k$ and $\boldsymbol{w}_k$ are assumed uncorrelated, the first order hold on $\boldsymbol{p}$ results in the augmented state noise linked to both the model noise and the force noise. It should be noted this also implies greater uncertainty in the augmented state than without the $\boldsymbol{F}$-terms. To obtain the zero order hold, $\boldsymbol{F}$ can be set to $\boldsymbol{0}$ and all equations will still apply as they stand. While the presented system descriptions are mathematical correct, they are only accurate up to the trueness of their presumptions. If the system behaves different from the statistical description, satisfactory results may not be obtained. $\boldsymbol{Q}$, $\boldsymbol{R}$ and $\boldsymbol{S}$ can without difficulties be assumed to vary with time, they can e.g. for time t_k be taken as functions of states at t_{k-1}, but this was not pursued here.

2.3 Estimation theory

2.3.1 Prediction, filtering and smoothing

Consider a dynamic system with measurements available. The system exhibits causal behavior, i.e. system outputs at any instant do not depend on subsequent inputs, as true for the state-space model. The states and measurements are noisy containing random contributions assumed to arise from some probability distribution. Henceforth the system is unpredictable, as strictly its behavior can only be described statistically. Stochastic interference renders attempts of exact calculations futile. An understanding of the governing probabilistic processes is therefore important. Based on this knowledge, *estimates* can be calculated. In this context, an estimate is a "best guess", meaning it is the most correct gauged by some set criterion. In practice minimization of a cost or error penalty function, or maximization of an objective function is used.

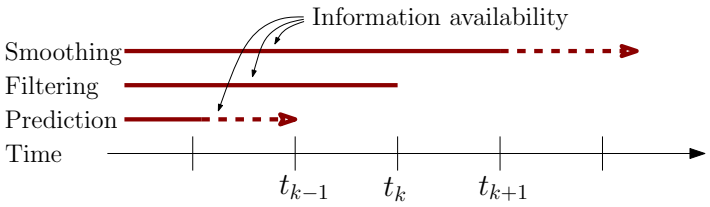

Figure 2.3: Three fundamental estimation concepts.

Prediction, filtering, and smoothing are fundamental concepts in estimation theory, here defined according to Anderson and Moore [12]. A graphical interpretation is showed in Fig. 2.3. Let $s(t)$ be a time-dependent variable estimated from noisy measurements $b(t)$ (s and b not representing the same quantity), assuming a discretized time domain. *Filtering* is the technique of estimating $s(t)$ using information (state and measurements) right up to and including time t. Along the same line, a *prediction* is a forecast estimate, where $s(t)$ is estimated using only information up to time $t - \theta$ $(\theta > 0)$. Prediction has the obvious major advantage of peeking into the future, but comes at the cost of less accuracy, especially dealing with high noise. Analogously, weather forecasts can in effect predict a few days ahead, but predictions months into the future will be too inaccurate for most practical purposes. *Smoothing* is the distinct opposite of prediction. In a smoothing problem, $s(t)$ is estimated using information up to time $t + \tau$ $(\tau > 0)$. In other words,

real time system monitoring is not possible, hindered by a time delay τ. More accuracy is however expected with availability of additional measurements. Considering noise, the extra information provided (i.e after t) is not redundant even if the system is causal. While smoothing can be a powerful tool, its applications is not further addressed here.

2.3.2 Prior and posterior estimate

The state-space model together with the Kalman filter (presented below) provides estimates. An estimate of a variable s is denoted by $\hat{s}$. s can represent physical quantities such as displacements and forces or abstract quantities such as standard deviation or mean. In estimation, s is taken to be a random variable even though it represents a quantity classically considered absolute. Estimates of random variables will depend on observations sampled in time. The *prior* (latin: *a priori*) estimate predicts state values at time step k given observations up to the previous step $k-1$. The *posterior* (latin: *a posteriori*) estimate is a refinement or updated value of the prior estimate, using observations extending up to the current step k. The subscript notation $\hat{s}_{k|k-1}$ and $\hat{s}_{k|k}$ denotes the prior and posterior estimate of s at step k, respectively. Conforming with the preceding section, the prior and posterior estimates are one-step prediction and filter estimates, respectively. Indices can be shifted linearly without loss of generality. While other conventions exist in literature, the use of the aforementioned notation will be kept consistent hereafter.

2.4 The Kalman filter

2.4.1 Derivation of the filter equations

The Kalman filter was developed in early 1960s by primarily Rudolf E. Kálmán [13]. To initiate the derivation, assume the linear relation:

$$\hat{\boldsymbol{x}}^a_{k|k} = \hat{\boldsymbol{x}}^a_{k|k-1} + \boldsymbol{L}_k(\boldsymbol{y}_k - \hat{\boldsymbol{y}}_k) \quad , \quad \hat{\boldsymbol{y}}_k = \boldsymbol{G}_a \hat{\boldsymbol{x}}^a_{k|k-1}$$

The interpretation is coherent: the posterior estimate equals the prior estimate plus an

added correction term. This correction includes a weighing matrix $\boldsymbol{L}_k$ and the innovation $(\boldsymbol{y}_k - \hat{\boldsymbol{y}}_k)$. The innovation tells how much the real observation $\boldsymbol{y}_k$ differs from our predicted observation $\hat{\boldsymbol{y}}_k$. $\hat{\boldsymbol{y}}_k$ is an unbiased estimate taken from Eq. (2.2.19), remembering the zero mean noise assumption. The weighing matrix is a measure of how much we trust our observations. An optimal weighing is derived later this section.

We aim for an unbiased estimate of $\boldsymbol{x}_k^a$, i.e. $\boldsymbol{E}[\boldsymbol{x}_k^a - \hat{\boldsymbol{x}}_{k|k}^a] = \boldsymbol{0}$. Gauging the error of the posterior estimate, conveniently denoted $\boldsymbol{e^f}_k$, it is simply:

$$\begin{aligned}
\boldsymbol{e^f}_k &= \boldsymbol{x}_k^a - \hat{\boldsymbol{x}}_{k|k}^a \\
&= \boldsymbol{x}_k^a - [\hat{\boldsymbol{x}}_{k|k-1}^a + \boldsymbol{L}_k(\boldsymbol{y}_k - \boldsymbol{G}_a\hat{\boldsymbol{x}}_{k|k-1}^a)] \qquad \text{(using defn. of posterior estimate)} \\
&= \boldsymbol{x}_k^a - [\hat{\boldsymbol{x}}_{k|k-1}^a + \boldsymbol{L}_k(\boldsymbol{G}_a\boldsymbol{x}_k^a + \boldsymbol{\upsilon}_k - \boldsymbol{G}_a\hat{\boldsymbol{x}}_{k|k-1}^a)] \qquad \text{(using defn. of measurement)} \\
&= (\boldsymbol{I} - \boldsymbol{L}_k\boldsymbol{G}_a)(\boldsymbol{x}_k^a - \hat{\boldsymbol{x}}_{k|k-1}^a) - \boldsymbol{L}_k\boldsymbol{\upsilon}_k
\end{aligned}$$

The error covariance matrix defined as $\boldsymbol{P}_{k|l} = \boldsymbol{E}[(\boldsymbol{x}_k^a - \hat{\boldsymbol{x}}_{k|l}^a)(\boldsymbol{x}_k^a - \hat{\boldsymbol{x}}_{k|l}^a)^T]$ contains the covariance of estimate errors, where the estimates $\hat{\boldsymbol{x}}_{k|l}$ at time step k are found using observations up to time l. Along the covenance stated in the Section 2.3.2, $\boldsymbol{P}_{k|k-1}$ and $\boldsymbol{P}_{k|k}$ must equal the covariance of prior and posterior estimate errors, respectively. $\boldsymbol{P}_{k|k}$ can be expressed by $\boldsymbol{P}_{k|k-1}$ via recursive manipulation:

$$\begin{aligned}
\boldsymbol{P}_{k|k} &= Cov[\boldsymbol{x}_k^a - \hat{\boldsymbol{x}}_{k|k}^a] \\
&= Cov[(\boldsymbol{I} - \boldsymbol{L}_k\boldsymbol{G}_a)(\boldsymbol{x}_k^a - \hat{\boldsymbol{x}}_{k|k-1}^a) - \boldsymbol{L}_k\boldsymbol{\upsilon}_k] \\
&= (\boldsymbol{I} - \boldsymbol{L}_k\boldsymbol{G}_a)\, Cov[\boldsymbol{x}_k^a - \hat{\boldsymbol{x}}_{k|k-1}^a](\boldsymbol{I} - \boldsymbol{L}_k\boldsymbol{G}_a)^T + \boldsymbol{L}_k Cov[\boldsymbol{\upsilon}_k]\boldsymbol{L}_k^T \\
&= (\boldsymbol{I} - \boldsymbol{L}_k\boldsymbol{G}_a)\, \boldsymbol{P}_{k|k-1}(\boldsymbol{I} - \boldsymbol{L}_k\boldsymbol{G}_a)^T + \boldsymbol{L}_k\boldsymbol{R}\boldsymbol{L}_k^T \\
&= \boldsymbol{P}_{k|k-1} - \boldsymbol{L}_k\boldsymbol{G}_a\boldsymbol{P}_{k|k-1} - \boldsymbol{P}_{k|k-1}\boldsymbol{G}_a^T\boldsymbol{L}_k^T + \boldsymbol{L}_k\boldsymbol{G}_a\boldsymbol{P}_{k|k-1}\boldsymbol{G}_a^T\boldsymbol{L}_k^T + \boldsymbol{L}_k\boldsymbol{R}\boldsymbol{L}_k^T
\end{aligned}$$

The error of the prior estimate is denoted $\boldsymbol{e^p}_k$. Repeating the procedure above (and here

evaluated at time $k+1$) it can be written as:

$$\begin{aligned}
\boldsymbol{e^p}_{k+1} &= \boldsymbol{x}^a_{k+1} - \hat{\boldsymbol{x}}^a_{k+1|k} \\
&= \boldsymbol{A}_a \boldsymbol{x}^a_k + \boldsymbol{\zeta}_k - \boldsymbol{A}_a \hat{\boldsymbol{x}}^a_{k|k} \qquad \text{(using the defn. of exact state and prior estimate)} \\
&= \boldsymbol{A}_a (\boldsymbol{x}^a_k - \hat{\boldsymbol{x}}^a_{k|k}) + \boldsymbol{\zeta}_k
\end{aligned}$$

And its error covariance is accordingly:

$$\begin{aligned}
\boldsymbol{P}_{k+1|k} &= Cov[\boldsymbol{x}^a_{k+1} - \hat{\boldsymbol{x}}^a_{k+1|k}] \\
&= Cov[\boldsymbol{A}_a (\boldsymbol{x}^a_k - \hat{\boldsymbol{x}}^a_{k|k}) + \boldsymbol{\zeta}_k] \\
&= \boldsymbol{A}_a Cov[\boldsymbol{x}^a_k - \hat{\boldsymbol{x}}^a_{k|k}] \boldsymbol{A}^T_a + Cov[\boldsymbol{\zeta}_k] \\
&= \boldsymbol{A}_a \boldsymbol{P}_{k|k} \boldsymbol{A}^T_a + \boldsymbol{Q}_a
\end{aligned}$$

In finding an optimal $\boldsymbol{L}_k$, one must define a norm for gauging the quality of an estimate. The Kalman filter aims to find a minimum mean square error (MSE) of the posterior estimate, equivalent to minimizing the diagonal sum of $\boldsymbol{E}[(\boldsymbol{x}^a_k - \hat{\boldsymbol{x}}^a_{k|k})(\boldsymbol{x}^a_k - \hat{\boldsymbol{x}}^a_{k|k})^T] = \boldsymbol{E}[\boldsymbol{e^f}_k \boldsymbol{e^f}^T_k]$ or min $\text{tr}(\boldsymbol{P}_{k|k})$. This is also referred to as a least squares (LS) solution or minimum-variance unbiased (MVU) estimator. By searching for a minimal point for $\boldsymbol{L}_k$, hereby called the *Kalman gain*, is found:

$$\frac{\partial \text{tr}(\boldsymbol{P}_{k|k})}{\partial \boldsymbol{L}_k} = -2(\boldsymbol{G}_a \boldsymbol{P}_{k|k-1})^T + 2\boldsymbol{L}_k \boldsymbol{R} + 2\boldsymbol{L}_k \boldsymbol{G}_a \boldsymbol{P}_{k|k-1} \boldsymbol{G}^T_a = 0$$

$$\boldsymbol{L}_k = \boldsymbol{P}_{k|k-1} \boldsymbol{G}^T_a [\boldsymbol{G}_a \boldsymbol{P}_{k|k-1} \boldsymbol{G}^T_a + \boldsymbol{R}]^{-1}$$

Substituting $\boldsymbol{L}_k$ back into $\boldsymbol{P}_{k|k}$, a simplification is obtained:

$$\boldsymbol{P}_{k|k} = \boldsymbol{P}_{k|k-1} - \boldsymbol{L}_k \boldsymbol{G}_a \boldsymbol{P}_{k|k-1}$$

To find a prior estimate, we resort to Eq. (2.2.18), erasing the noise term of zero expectancy:

$$\hat{\boldsymbol{x}}^a_{k+1|k} = \boldsymbol{A}_a \hat{\boldsymbol{x}}^a_{k|k}$$

This completes the derivation and the equations forming the entire Kalman filter algorithm are assembled below.

$$\boldsymbol{L}_k = \boldsymbol{P}_{k|k-1}\boldsymbol{G}_a^T[\boldsymbol{G}_a\boldsymbol{P}_{k|k-1}\boldsymbol{G}_a^T + \boldsymbol{R}]^{-1} \tag{2.4.1a}$$

$$\hat{\boldsymbol{x}}_{k|k}^a = \hat{\boldsymbol{x}}_{k|k-1}^a + \boldsymbol{L}_k(\boldsymbol{y}_k - \boldsymbol{G}_a\hat{\boldsymbol{x}}_{k|k-1}^a) \tag{2.4.1b}$$

$$\boldsymbol{P}_{k|k} = \boldsymbol{P}_{k|k-1} - \boldsymbol{L}_k\boldsymbol{G}_a\boldsymbol{P}_{k|k-1} \tag{2.4.1c}$$

$$\hat{\boldsymbol{x}}_{k+1|k}^a = \boldsymbol{A}_a\hat{\boldsymbol{x}}_{k|k}^a \tag{2.4.2a}$$

$$\boldsymbol{P}_{k+1|k} = \boldsymbol{A}_a\boldsymbol{P}_{k|k}\boldsymbol{A}_a^T + \boldsymbol{Q}_a \tag{2.4.2b}$$

The equations are separated into two sets: *measurement update* Eq. (2.4.1) and *time update* Eq. (2.4.2). With this, the predictor-update process of estimation should be more apparent, and is visualized in the diagram in Fig. 2.4. The prior estimate is calculated first, in effect propagating system dynamics one step ahead in time. Further measurements is then applied in the update, optimizing the solution yielding the posterior estimate. The posterior estimate is optimally unique in minimizing the MSE [12]. Uniqueness of the solution is a general condition for well-posedness of inverse problems [14]. For reasons of summing non-coinciding units (e.g. m, m/s and N), the MSE of the augmented state must be considered dimensionless. Different formulations can be found in literature and indexes may be shifted. The Kalman filter usually presented in a non-augmented form employing a Kalman gain denoted $\boldsymbol{K}_k$ with the linear connection $\boldsymbol{K}_k = \boldsymbol{A}_a\boldsymbol{L}_k$. The approach presented here is fully equal by means of optimization.

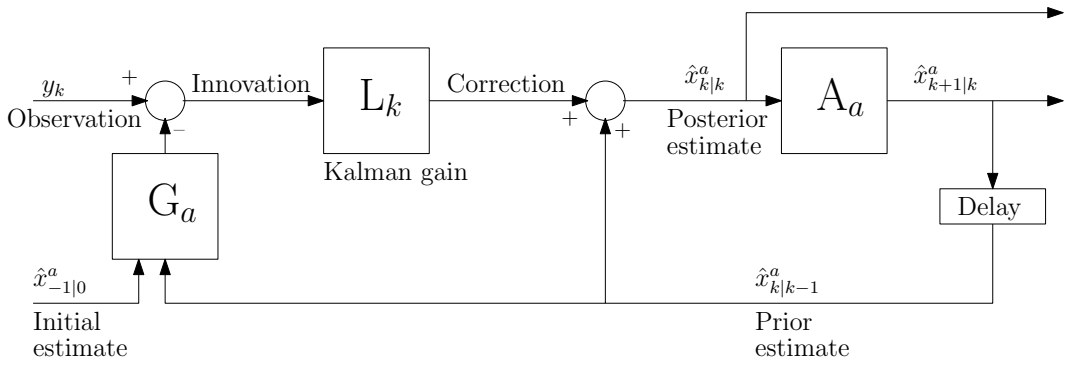

Figure 2.4: Block diagram of Kalman filter implementation. Calculation of $\boldsymbol{L}_k$ is done externally.

2.4.2 Filter considerations

An advantage of the Kalman filter is its explicit formulation and the algorithm having a constant number of computations in each step, avoiding the need for iterations to find an optimal estimate. The recursive form is also beneficial, not directly using all available data, allowing for easier implementation and faster calculation.

Regarding initial values, it is evident $\boldsymbol{P}_{0|-1}$ and $\hat{\boldsymbol{x}}^a_{0|-1}$ must be supplied to initiate the algorithm. Chan et al. [15] suggested letting $\boldsymbol{P}_{0|-1}$ be of high magnitude, diagonally $\sim 10^{10}$, effectively treating errors in the first steps as large and imposing the filter to ignore the first estimates. With an increasing number of observations, the initial estimate becomes less important. Running short time series, the estimation is more sensitive to failure in supplying a correct initial estimate. As the number of steps approaches infinity, the results become independent of the initial estimate, provided that $\boldsymbol{P}_{0|-1}$ is positive definite [8] (sufficiently satisfied by a diagonal matrix).

One notable case is that of high observation noise: In the limit $\boldsymbol{R} \to \infty$ the Kalman gain $\boldsymbol{L}_k \to \boldsymbol{0}$, so the measurement update has zero influence. The opposite is also true. If $\boldsymbol{v}_k = \boldsymbol{0}$ or $\boldsymbol{R} = \boldsymbol{0}$ the the observations is trusted more. Working with a set of observations, one must therefore try to make an educated guess about noise magnitude. Calibration and characterization (white or colored) of noise can be done by sampling during constant inputs [10]. A simple verification of the Kalman filter performance can be done by looking at the innovation $\boldsymbol{y}_k - \boldsymbol{G}_a \hat{\boldsymbol{x}}^a_{k|k-1}$ [16]. This should be a white process because failure to predict measurements exactly stems from white noise itself. If this fails to be true, there are indications of design errors. Looking for peaks in a spectral density chart can reveal interference at certain frequencies not covered in the white noise description.

Another point worth noting is $\hat{\boldsymbol{x}}^a_{k|k}$ depends on $\boldsymbol{y}_k$, but $\boldsymbol{P}_{k|k}$ does not, meaning the error covariance can be calculated before the filter for estimates is run (referred to as an offline calculation) [12]. The role of the error covariance can be further investigated. The filter can reach a steady state, where the covariances $\boldsymbol{P}_{k|k}$ and $\boldsymbol{P}_{k|k-1}$ does not change for each

iteration. The same is therefore true for the Kalman gain by its definition in Eq. (2.4.1a). It might be convenient finding the steady state matrices prior to analysis, providing the filter with the steady state matrix initially for optimal performance. With the assumption $\boldsymbol{P}_{k|k} = \boldsymbol{P}_{k|k-1} \equiv \boldsymbol{P}_\infty$ and by using Eq. (2.4.2b), one arrives the so-called discrete Lyapunov equation [16]:

$$\boldsymbol{A}_a \boldsymbol{P}_\infty \boldsymbol{A}_a^T - \boldsymbol{P}_\infty + \boldsymbol{Q}_a = 0$$

The associated solution $\boldsymbol{P}_\infty = \sum_{m=0}^{\infty} (\boldsymbol{A}_a)^m \, \boldsymbol{Q}_a \, (\boldsymbol{A}_a^T)^m$ is only valid if $\boldsymbol{A}_a$ is stable. This requires $\boldsymbol{A}_a$ having eigenvalues strictly inside the unit circle [8], which is violated by the fact that $\boldsymbol{A}_a$ always has n_p eigenvalues equal to 1, associated with the unknown forces [6]. While this is not generally the case for the non-augmented $\boldsymbol{A}$, the augmented system must be considered unstable. A weaker assumption is $\boldsymbol{P}_{k|k} \neq \boldsymbol{P}_{k|k-1}$, but both still asymptotically reaching their respective steady state values. From this the so-called discrete algebraic Riccati equation (DARE) is derived (see Appendix B):

$$\boldsymbol{Q}_a - \boldsymbol{P}_{k|k-1} + \boldsymbol{A}_a \boldsymbol{P}_{k|k-1} \boldsymbol{A}_a^T - \boldsymbol{A}_a \boldsymbol{P}_{k|k-1} \boldsymbol{G}_a^T (\boldsymbol{G}_a \boldsymbol{P}_{k|k-1} \boldsymbol{G}_a^T + \boldsymbol{R})^{-1} \boldsymbol{G}_a \boldsymbol{P}_{k|k-1} \boldsymbol{A}_a^T = 0$$

which can be solved for $\boldsymbol{P}_{k|k-1}$, followed by $\boldsymbol{P}_{k|k}$ from Eq. (2.4.1c). In Appendix B we show that the existence of an asymptotically steady solution, and hereby a bound on the expected error, requires the following three criteria to be satisfied:

1. $\text{rank} \begin{bmatrix} \boldsymbol{A} - \lambda \boldsymbol{I} \\ \boldsymbol{G} \end{bmatrix} = n_s$, where λ is an eigenvalue of $\boldsymbol{A}$ and $|\lambda| \geq 1$.
2. The system $(\boldsymbol{A}, \boldsymbol{B}, \boldsymbol{G}, \boldsymbol{J})$ must have no transmission zero equal to 1.
3. $n_d \geq n_p$

We also argue that the first criteria always will be fulfilled in a structural dynamic system. Not only for performance optimization, covariance matrices also reveals the expected errors, which prior to filtering can indicate whether or not satisfactory accuracy is obtained.

In solving in a linear system $\boldsymbol{Z}\boldsymbol{x} = \boldsymbol{b}$, $\boldsymbol{Z}^{-1}$ need not be calculated explicitly. Solving numerically for $\boldsymbol{x}$ will generally give better numerical stability [10]. This principle is

done is all MATLAB implementations by the syntax $x = Z \setminus b$. The performance of an implemented Kalman filter can still suffer for a number of reasons. Program round-off errors, large matrix dimensions, high condition numbers and numerical inversion problems are some well-known issues [10]. The latter is especially true if one has little confidence in the initial error estimation, so $\boldsymbol{P}_{0|-1} \gg \boldsymbol{R}$, leading to zero Kalman gain if precision is poor. Loss of symmetry in covariance matrices is a sign of numerical instability. To induce stability, methods of matrix decomposition or factorization is often introduced. These issues and related remedies are however not specifically addressed any further, other than keeping in mind possible effects.

2.4.3 Probabilistic origins and relation to Bayesian statistics

A justification for choosing the Kalman filter optimization as minimum MSE is the connection to maximum likelihood estimation (MLE). Suppose data is sampled from a joint probability density function (PDF) p_θ, a function of the system parameter set θ. MLE then resolves a suitable set θ such that the likelihood of the observed realizations is maximized. In other words, a model is formed on basis of agreeing with sample data. Provided that the uncertainties (noise) is Gaussian, the MSE approach gives the same result as a MLE approach [17]. In the current setting, the parameter set defining the joint PDF are properties of the state variables and the sample data is observations.

The Kalman filter is also related to Bayesian statistics, a field of mathematics dealing with conditional probabilities. Suppose x and y are random variables, dependent on each other. With information on y available, the PDF of x is modified. For scalars, with f being a joint PDF, this is often written:

$$f_{X|Y}(x|y) = \frac{f_{X,Y}(x,y)}{\int_S f_{X,Y}(x,y)\,dx} = \frac{f_{X,Y}(x,y)}{f_Y(y)} \qquad (x \,\epsilon\, S \quad , \quad f_Y(y) \neq 0)$$

The PDFs of x before and after this information is provided is called the prior and posterior PDF. In the Kalman filter, the measurement update is conditioned on the information from the current timestep. Since $\hat{\boldsymbol{x}}^a_{k|k}$ is linear in the Gaussian variable $\boldsymbol{y}_k$, $\hat{\boldsymbol{x}}^a_{k|k}$ will itself be Gaussian [12, 16]. $\hat{\boldsymbol{x}}^a_{k|k}$ is in reality a conditional mean estimate (i.e. first

non-central moment of the posterior PDF), statistical optimal in estimating the state by minimizing the MSE. For scalars, this yields:

$$\hat{x} = E[X|Y = y] = \int_S x \, f_{X|Y}(x|y) \, dx = \int_S x \, \frac{f_{X,Y}(x, y)}{f_Y(y)} \, dx$$

This way of constructing a posterior PDF in light of new information is also called recursive Bayesian estimation. It can be shown the conditional mean minimizes the expected Bayes risk, where the expected error penalty relies on the error squared [16, 18]. Since estimates are generated from PDFs, one could construct confidence intervals rather than a single estimate value, also expressing the estimate uncertainty. The posterior and prior estimate are both unbiased conditional mean estimates. It can be shown that the best linear estimator, in terms of minimizing the expected squared error, is always unbiased [10]. In a linear problem with Gaussian variables, a probabilistic approach with recursive Bayesian estimation therefore becomes equivalent to the Kalman filter. Bayesian estimation can also be formulated on a general case with arbitrary distributions, whose result is more complicated and computational heavy. The most relevant PDFs are summed up below [18], where $\boldsymbol{y}_{a:b}$ means the observation sequence $\{\boldsymbol{y}_a \cdots \boldsymbol{y}_b\}$.

$$\begin{aligned}
p(\boldsymbol{x}_k^a|\boldsymbol{x}_{k-1}^a) &= \mathcal{N}(\boldsymbol{A}_a\boldsymbol{x}_{k-1}^a, \boldsymbol{Q}_a) \\
p(\boldsymbol{y}_k|\boldsymbol{x}_k^a) &= \mathcal{N}(\boldsymbol{G}_a\boldsymbol{x}_k^a, \boldsymbol{R}) \\
p(\boldsymbol{x}_k^a|\boldsymbol{y}_{1:k-1}) &= \mathcal{N}(\hat{\boldsymbol{x}}_{k|k-1}^a, \boldsymbol{P}_{k|k-1}) \\
p(\boldsymbol{x}_k^a|\boldsymbol{y}_{1:k}) &= \mathcal{N}(\hat{\boldsymbol{x}}_{k|k}^a, \boldsymbol{P}_{k|k})
\end{aligned}$$

To visualize statistics of the filter process, a scalar example is presented. We try to estimate a quantity x, initially equal to 10 and changed each step with a noise contribution $\sim \mathcal{N}(0, Q)$, where $Q = 5 \times 10^{-3}$. This example is overly simple and cannot directly be related to force identification applications, but demonstrates some statistical features of the Kalman filter. (Note: here, in the absence of an input, the augmented form is not really necessary). Also, this gives a helpful graphical illustration of PDFs, which is less viable for systems with more variables. Direct unbiased observations of x are provided, called y. These are contaminated with white noise, $y \sim \mathcal{N}(x, 1.5)$, so $R = 1.5$. To give

an useful interpretation, let x be a 1D position changed by some random factor and y noisy coordinate readings. Initial estimates are set to $x_{0|-1} = 6$ and $P_{0|-1} = 1$. The filter process over 50 samples is visualized in Fig. 2.5 and 2.6. The filter estimate starts too low due to the biased initial estimate, then approaching the true value. The uncertainty ($P_{k|k}$) decreases by more samples, converging towards $\frac{Q}{2}(\sqrt{1 + \frac{4R}{Q}} - 1) = 0.0841$.

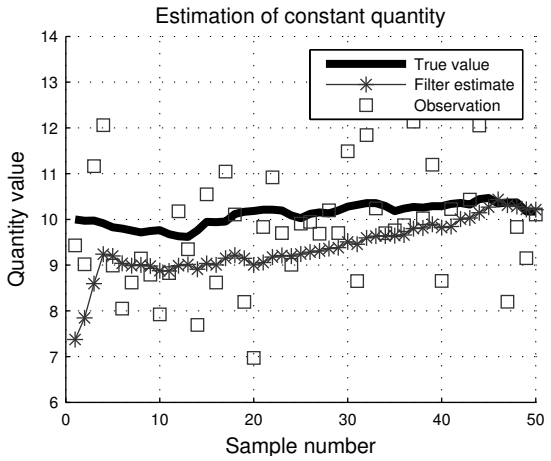

Figure 2.5: Estimation process of x.

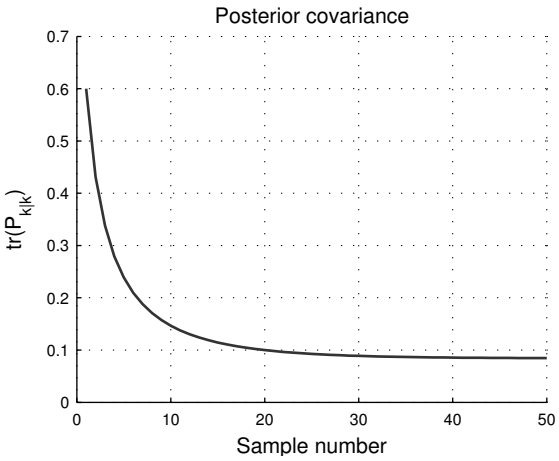

Figure 2.6: Posterior estimate error covariance.

Of particular interest is the PDFs shown in Fig. 2.7. Note the change in uncertainty (bell curve height) over both step update and over multiple steps. The posterior PDF is more always more narrow than the prior PDF, meaning the uncertainty in our estimate is reduced with receiving a measurement. This does not however guarantee the posterior estimate always *is* more correct than the prior, we only *expect* it to be more correct by means of minimum MSE. Looking at step $k = 10$, we arrive at such a situation, with the posterior estimate moving further away from the true value. This is caused by the quite low observation $y_{10} = 7.923$, fooling the estimate update by high (negative) noise. The statistical description of the system must naturally be as accurate as possible. Providing false information can damage the filter performance, as confidence in the estimates is based on the system behaving in accordance with its statistical description provided by the analyst. This is particularly important for noise covariance matrices. Notably, the solution is generally less sensitive to changes in $\boldsymbol{Q}$ and $\boldsymbol{R}$ than compared to $\boldsymbol{S}$ [6]. For practical purposes, several parallel observations in desired. Statistically, multiple observations having particular high noise at the same time is less likely than just one

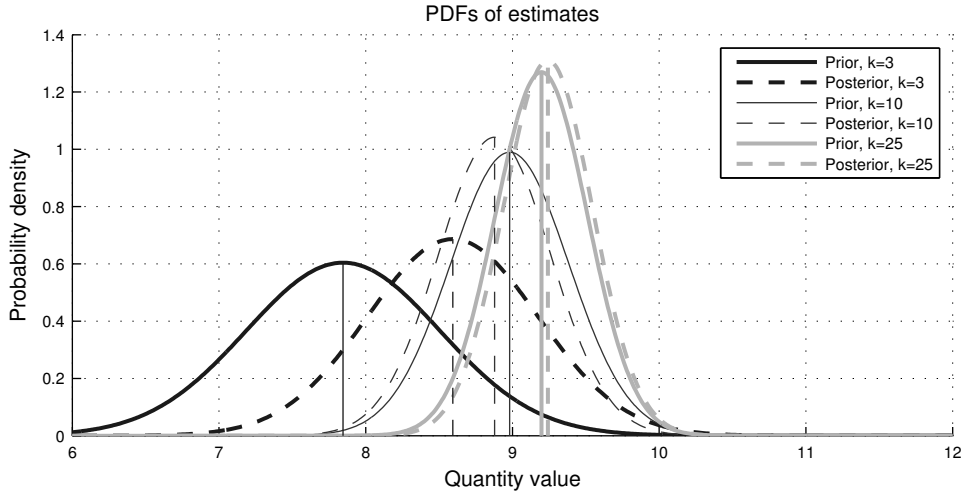

Figure 2.7: PDFs provided by the Kalman filter at three different steps. The (conditional mean) estimates are the values associated with the vertical lines.

observation encountering the same noise. Multiple measurements should therefore give better results.

2.5 Requirements for sufficient identification

2.5.1 Observability

Observability is a relevant concept in states-space problems. It concerns whether one are able to reconstruct the states uniquely from an observation sequence. This is influenced by the number and type of observations and their location in the system. A general requirement for observability in the non-augmented state-space problem can be formulated as [6]:

$$\text{rank} \begin{bmatrix} \boldsymbol{G} \\ \boldsymbol{GA} \\ \vdots \\ \boldsymbol{GA}^{n_s-1} \end{bmatrix} = n_s$$

where it is recalled $n_s = 2 \times n_{dof}$ is the dimension of the (non-augmented) state vector. This is normally not achieved in most structures, as it would require a great number of

sensors carefully distributed. In practice this means all modes cannot be detected. In the particular case of force identification, the remaining states (i.e. displacements and velocities) are of less interest. If the number of forces (n_p) do not exceed the number of modes excited, and at least n_p modes are distinguishable from the acceleration measurements, a relaxed observability criteria is fulfilled [19]. The number of accelerometers must also be equal or greater than n_p. These results stems from the rationale that only modes excited by the force are of importance in identification.

$\boldsymbol{J}$ also plays an active role, as the magnitude of its elements directly signify how much the unknown forces influences the observations through Eq. (2.2.13) [6]. Accelerometers collocated with the forces will generally give the best results. Furthermore, they should not be placed at zero-points of a mode. $\boldsymbol{J}$ is contained in $\boldsymbol{G}_a$, whom the Kalman gain $\boldsymbol{L}_k$ is a multiple function of, heightening the effect of its magnitude. This possibly poses a numerical problem, specially in through the matrix inversion. We look at an identification case of a single force in located in DOF no. p with an arbitrary number of accelerometers j, placed in DOFs no. $a_1 \dots a_j$. Repeating Eq. (2.2.9), $\boldsymbol{J}$ written out reads:

$$\begin{aligned}\boldsymbol{J} = \boldsymbol{S}_a \boldsymbol{M}^{-1} \boldsymbol{S}_p &= \begin{bmatrix} 0 \cdots 1_{1,a_1} \cdots 0 \\ \vdots \\ 0 \cdots 1_{j,a_j} \cdots 0 \end{bmatrix} \begin{bmatrix} M^{-1}_{1,1} & M^{-1}_{1,2} & \cdots & M^{-1}_{1,n_{DOF}} \\ M^{-1}_{2,1} & M^{-1}_{2,2} & \cdots & M^{-1}_{2,n_{DOF}} \\ \vdots & \vdots & \ddots & \vdots \\ M^{-1}_{n_{DOF},1} & M^{-1}_{n_{DOF},2} & \cdots & M^{-1}_{n_{DOF},n_{DOF}} \end{bmatrix} \begin{bmatrix} 0 \\ \vdots \\ 1_{p,1} \\ \vdots \\ 0 \end{bmatrix} \\ &= \begin{bmatrix} 0 \cdots 1_{1,a_1} \cdots 0 \\ \vdots \\ 0 \cdots 1_{j,a_j} \cdots 0 \end{bmatrix} \begin{bmatrix} M^{-1}_{1,p} \\ \vdots \\ M^{-1}_{n_{DOF},p} \end{bmatrix} = \begin{bmatrix} M^{-1}_{a_1,p} \\ \vdots \\ M^{-1}_{a_j,p} \end{bmatrix} = \begin{bmatrix} M^{-1}_{p,a_1} \cdots M^{-1}_{p,a_j} \end{bmatrix}^T \end{aligned}$$

For a simply supported beam with one force fixed midspan and one accelerometer, the scalar value of $J = M^{-1}_{a,p}$ is shown in Fig. 2.8. This confirms the proximity of the accelerometer is important. Since $M^{-1}_{a,p} = M^{-1}_{p,a}$, the accelerometer and force nodes can be swapped yielding the same numerical result. Moreover, a finer mesh will seemingly increase influence with collocated sensors, but deteriorates rapidly with increased gap.

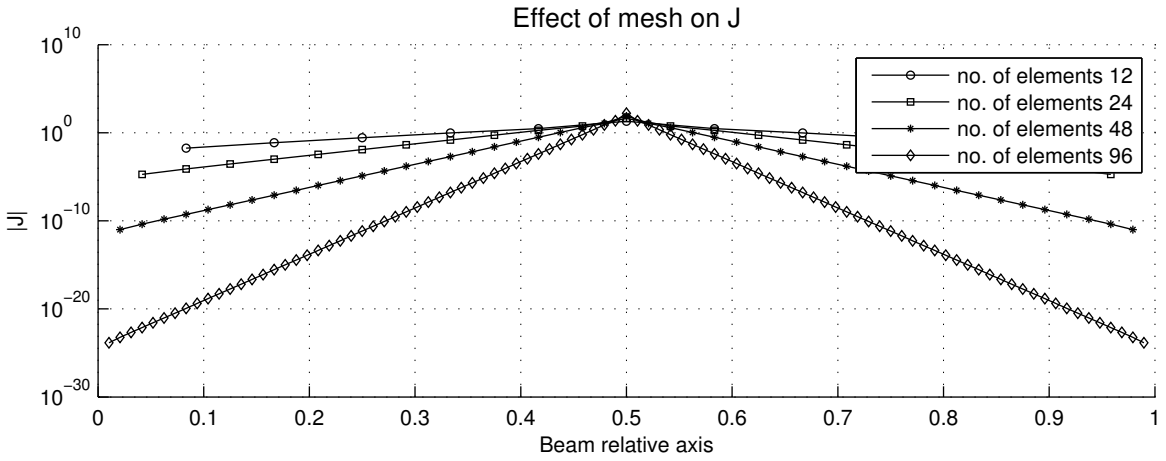

Figure 2.8: J on a simple supported beam with respect to varying accelerometer placement, with a single unknown force fixed midspan. The beam is for simplicity constructed by 2D 4 DOF Euler-Bernoulli elements. End nodes are omitted.

From the linearity in the logarithmic plot, the decrease in J is close to exponential. A finer mesh will however allow for an increase in possible sensor and force locations, and likely give a better model representation. There exists a possibility that a biased mesh, i.e. refined near sensors or force locations, generally will give better results without having to refine the whole model, thus not substantially increasing computational load. Development of such an optimal mesh distribution is uncharted area.

2.5.2 Stability

The system must have sufficient *stability* for the system inversion to be unique. The stability depends on the so-called transmission zeros λ_j [6], satisfying:

$$\begin{bmatrix} \boldsymbol{A} - \lambda_j \boldsymbol{I} & \boldsymbol{B} \\ \boldsymbol{G} & \boldsymbol{J} \end{bmatrix} \begin{bmatrix} \boldsymbol{x}_0 \\ \boldsymbol{p}_0 \end{bmatrix} = \begin{bmatrix} \boldsymbol{0} \\ \boldsymbol{0} \end{bmatrix}$$

To demonstrate why this is destructive, note that:

$$\boldsymbol{A}\boldsymbol{x}_0 + \boldsymbol{B}\boldsymbol{p}_0 \equiv \boldsymbol{x}_1 = \boldsymbol{x}_0 \lambda_j$$

Here, Eq. (2.2.10) and not (2.2.11) have been used since $\boldsymbol{p}_{k+1} - \boldsymbol{p}_k$ is treated as noise term in system inversion. Assuming a force on the form $\boldsymbol{p}_k = \boldsymbol{p}_0 \lambda_j^k$ $(k \geq 0)$, the further

response reads:

$$\begin{aligned}\boldsymbol{x}_2 &= \boldsymbol{A}\boldsymbol{x}_1 + \boldsymbol{B}\boldsymbol{p}_1 \\ &= \boldsymbol{A}\boldsymbol{x}_0\lambda_j + \boldsymbol{B}\boldsymbol{p}_0\lambda_j \\ &= \boldsymbol{x}_0\lambda_j^2 \\ &\vdots \\ \boldsymbol{x}_k &= \boldsymbol{x}_0\lambda_j^k\end{aligned}$$

and for observations (Eq. (2.2.13)):

$$\begin{aligned}\boldsymbol{y}_k &= \boldsymbol{G}\boldsymbol{x}_k + \boldsymbol{J}\boldsymbol{p}_k \\ &= \boldsymbol{G}\boldsymbol{x}_0\lambda_j^k + \boldsymbol{J}\boldsymbol{p}_0\lambda_j^k \\ &= (\boldsymbol{G}\boldsymbol{x}_0 + \boldsymbol{J}\boldsymbol{p}_0)\lambda_j^k \\ &= \boldsymbol{0}\end{aligned}$$

This can be interpreted as zero observations despite nonzero force and response. This clearly poses a problem since this force can be included to any event without influencing the observational data. Since the presence of such a force cannot be told, uniqueness in inversion (system reconstructability) is not achieved. If $|\lambda_j| > 1$, the response will grow unbounded rendering the system unstable. If $|\lambda_j| < 1$, the force and response will converge towards zero and asymptotic convergence is obtainable. The system is marginally stable in the case of $|\lambda_j| = 1$, notably occurring if only collocated acceleration data is present, disenabling identification of static components [19]. By including displacement or strain measurements the 0 Hz component is restored. Discretization, type and location of measurements will affect the transmission zeros. Instability is in addition displayed by increasing $\mathrm{tr}(\boldsymbol{P}_{k|k})$ [6], accounting for expected errors.

2.6 Current methods and existing research

Numerous offshore light houses and channel markers in the Gulf of Bothnia have been studied since 1973 to identify ice loads [20]. Methods of analysis mentioned by Bjerkås [20] include monitoring of structural response and hindcast calculations. Hindcast calculations involve evaluation of load actions based on structural deterioration or damage assessment

(e.g. permanent deformations, friction slip or fractures), consequently yielding a max load and not a time history. This method is therefore of less interest here. Response measurements is more in line with the methods used in this thesis.

Lourens [6] developed the augmented Kalman filter used throughout this thesis. A numerical simulation of a multiple input multiple output (MIMO) cantilever was presented. Two simultaneous forces were identified using 10 accelerometers sampling at 10 kHz. Both estimation of forces and displacement response were found to be good. With including strain measurements the results improved, attributed mainly to the removal of low-frequency (i.e. quasi-static) drift. Experimental validation was performed on a simply spring-supported beam. The identification was done by a joint input-state estimator, developed by Gillijns [21]. This can briefly be described as an algorithm structured as the Kalman filter, but with no assumptions on force characteristics needed. This opposes the force as a Gaussian random walk introduced in Eq. (2.2.17). $\boldsymbol{R}$ and $\boldsymbol{Q}$ were constructed from percentages peak values in observation data and states, respectively. Purely deterministic methods were found to perform inferiorly in comparison with stochastic-deterministic, as expected. Subject to sine loads of multiple frequencies, the augmented Kalman filter performed similarly to joint input-state estimator, compared by error root mean square (RMS).

Ma et al. [22] presented a stochastic state-space formulation together with a Kalman filter finding displacements and velocities. This was accompanied by a separate LS scheme for estimating time-discrete forces. Sampling at 20 kHz, numerical simulations demonstrated ability to accurate estimate impulse forces in both single degree of freedom (SDOF) and multi degree of freedom (MDOF) systems. The same method was repeated by Ma and Lin [23] on a physical cantilever, treated as a SDOF system. The estimation of periodic and random excitation forces from displacement measurements were accurate at 6666 Hz sampling. Later, Ma et al. [11] expanded on this, looking into MIMO systems. A numerical example on a cantilever were performed, identifying continuous harmonic forces at multiple nodes, triangular and rectangular impulses as well as random forces. In this formulation, forces at all system nodes were identified, including the ones not subject

to external loads. This differs from the augmented Kalman filter, where only forces at certain DOFs are considered, selected through $\boldsymbol{S_p}$, see Eq. (2.2.1). Disregarding this principle could potentially, due to noise, lead to getting nonzero forces in nodes known to be unloaded. Based on the results from the harmonic force, Ma et al. concluded this not to be of concern. Dealing with wind loads varying in time and space across a structure, the formulation might be necessary. $\boldsymbol{R}$ and $\boldsymbol{Q}$ were obtained by numerical calibration. Overall results showed the method to perform satisfactory, be capable of handling noise and provide accurate estimates.

Wind loads have also been researched in a Kalman filter setting. Hwang et al. [24] studies loads in a modal space, with a reduced number of modes. Through numerical demonstrations on both SDOF and MDOF systems, acceleration measurements were found to give more stable load estimation than displacements or velocities. This was attributed to noise amplification for the latter in the frequency range above resonance. The results were little affected by noise levels estimating a random load, but highly sensitive in the case of a harmonic input.

Hollandsworth and Busby [25] experimented with identification of impact forces on a cantilever, using a state-space formulation together with a dynamic programming LS solution. Results showed the best estimation were obtained with the accelerometer close to the location of the unknown force. Refining the FE model from 10 to 20 elements, little difference in results were found.

Other identification methods, both in time and frequency domain, can be found in literature. Many of these are based concepts similar to the ones presented here, including but not limited to state-space formulations, LS schemes, optimality principles and Kalman filter variations. These were however not considered relevant enough or outside the predefined scope, and is not discussed here.

Chapter 3

Analysis and results

3.1 Simulated two DOF mass-spring system

3.1.1 System description

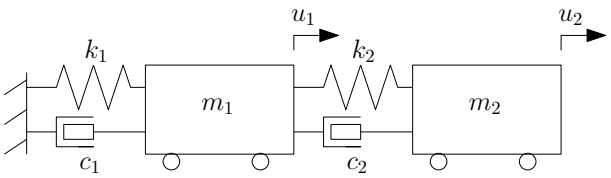

Figure 3.1: Mass-spring system with viscous damping.

A numerical simulation on a two DOF mass-spring system was performed, whose system properties are listed below and sketched in Fig. 3.1. The simulation aimed to to identify forces and reconstruct the states using a state-space model and a MATLAB-implemented Kalman filter, and through this investigate the filtering capabilities.

$$k_1 = 300 \times 10^3 \text{ N/m} \qquad c_1 = 2 \text{ Ns/m} \qquad m_1 = 1.0 \text{ kg}$$
$$k_2 = 400 \times 10^3 \text{ N/m} \qquad c_2 = 1 \text{ Ns/m} \qquad m_2 = 1.5 \text{ kg}$$

The undamped natural frequencies were found to be $f_1 = 48$ Hz and $f_2 = 149$ Hz. A positive triangular load with amplitude 400 N and period $4{\times}10^{-3}$ s was applied in u_2 over the time interval $0 \leq t \leq 10^{-1}$ s. The system was set to rest at initial time. A numerical solution was then found by Eq. (2.2.11) and (2.2.13), here claimed to be "exact" because

of its accuracy, practically not deviating from an analytical solution. Displacements and accelerations were measured in both DOFs sampling at $f_s = 10$ kHz. This renders the observation vector, selection matrices and force application matrix as:

$$\boldsymbol{y} = \begin{bmatrix} u_1 \\ \ddot{u}_1 \\ u_2 \\ \ddot{u}_2 \end{bmatrix} \qquad \boldsymbol{S}_a = \begin{bmatrix} 0 & 0 \\ 1 & 0 \\ 0 & 0 \\ 0 & 1 \end{bmatrix} \qquad \boldsymbol{S}_v = \begin{bmatrix} 0 & 0 \\ 0 & 0 \\ 0 & 0 \\ 0 & 0 \end{bmatrix} \qquad \boldsymbol{S}_d = \begin{bmatrix} 1 & 0 \\ 0 & 0 \\ 0 & 1 \\ 0 & 0 \end{bmatrix} \qquad \boldsymbol{S}_p = \begin{bmatrix} 0 \\ 1 \end{bmatrix}$$

This system has no transmission zeros and fulfills full observability. White noise were added to the observations. The elements (denoted subscript i) of the noise vector $\boldsymbol{\epsilon_k}$ were simulated as expressed in Eq. (3.1.1), an approach used by Lombaert et al. [26]. This construes as a random variable r_k drawn from a standard normal distribution scaled by the factors γ and σ_i (i.e. the standard deviation of the exact measurement time series itself). The latter ensures noise deviation to correspond to the deviation of the measured quantity. Another possible approach is using the RMS instead of the standard deviation [3]. The two essentially become equivalent in the event of zero mean. The non-dimensional factor γ regulates noise magnitude, in this case set to 5% and 10%. For illustrative purposes, an exemplified noise process in u_1 and its frequency spectrum is shown in Fig. 3.2 and 3.3.

$$\epsilon_{i,\,k} = \gamma \sigma_i r_k \quad , \quad \sigma_i = \sigma(y_i) \quad , \quad r_k \sim \mathcal{N}(0,1) \tag{3.1.1}$$

$\hat{\boldsymbol{x}}^a_{0|-1}$ was set to $\mathbf{0}$ and $\boldsymbol{P}_{0|-1}$ to 10^{-8} on diagonal entries, expected to quickly update over the first few steps. Model noise, $\boldsymbol{Q} = \boldsymbol{I} \times 10^{-10}$, was added to the forward solution to resemble a real case. $\boldsymbol{R}$ and $\boldsymbol{S}$ were fixed to $\boldsymbol{I} \times 10^{-10}$ and 1, respectively.

3.1.2 Force estimation

The resulting displacement and force estimation is shown in Fig. 3.4 and 3.6 for the two noise levels. The force estimation can for both cases be considered accurate, which is reasonable in such a simple system with multiple observations. The ratio of two DOFs

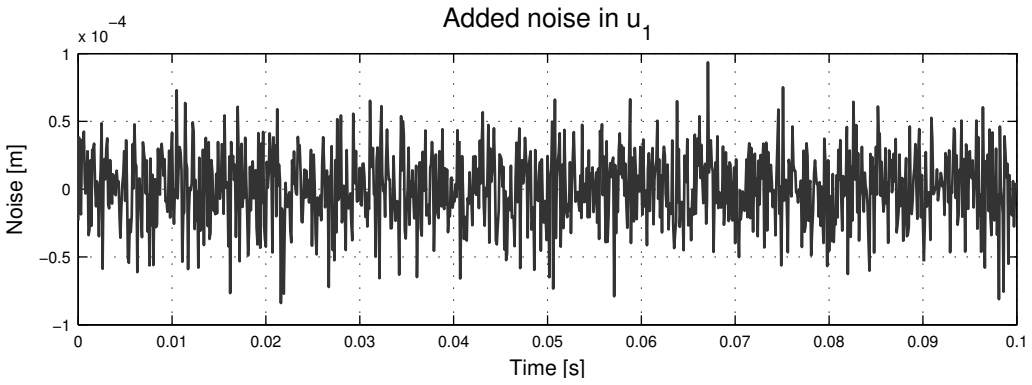

Figure 3.2: White noise process in u_1. Noise level is 5%.

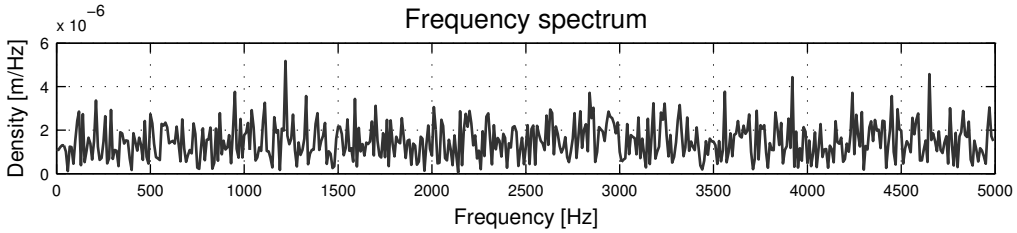

Figure 3.3: Frequency spectrum of white noise. Fluctuations is a result of the noise being a particular (time finite) realization of a random process.

and four observations will obviously not sustain moving to real structures. The influence of noise level can be noticed by the intermediate fluctuations. For both noise levels the differences between prior and posterior state estimates are small, with apparently overlapping curves. Although not shown, velocity estimates were found to be very accurate, more so than displacements.

The scalar measures of error $(\boldsymbol{e^p}_k)^T\boldsymbol{e^p}_k$ and $(\boldsymbol{e^f}_k)^T\boldsymbol{e^f}_k$ (i.e. sum of squared errors (SSE) within one time step) are used in Fig. 3.5 and 3.7 to demonstrate the filter ability to reduce errors in measurement update. At 5% noise, it is easy to see the posterior estimate outperforms the prior. For 10% noise level, the difference is more subtle, but still visible. The SSE is of particular interest, as the algorithm is based on minimizing it in each step. A comparison of SSE vs noise level can be found in Table 3.1, where a 2% noise simulation also have been included. Note that these values stem from *one* noise realization. In order to create an unbiased measure of performance, one would have to repeat simulations along

Monte Carlo principles. At 5% noise in Fig. 3.5, one can notice errors in both estimates drop close to zero even time intervals. This stems from the assumption Eq. (2.2.17) of the force rate as random process with zero mean, when in fact here it is constant (positive or negative). At points where the force rate is changing sign (peak or valley), the prior estimate accidentally becomes very good due to its one time step lag. This must therefore be regarded a coincidence, and will not generally be true for other data. The same effect can be found at higher noise levels.

It should also be remarked the square error is dominated by the force. Errors in velocities and displacements are significantly smaller, further emphasized by squaring. The main measurement update is also done in the force. This can at first sight suggest the filter is biased towards correcting one variable (the force) at the expense of others, as it considers absolute errors and not their relative value. A quick fix would be constructing a diagonal weighing matrix $\boldsymbol{W}$ and modifying the optimality criteria such that $\text{tr}(\boldsymbol{W}\boldsymbol{P}_{k|k})$ is minimized. If this is done, the Kalman gain will remain unchanged by its derivation in Section 2.4.1, thereby giving $\boldsymbol{W}$ zero influence. This implies the expected state errors are minimized individually and not just as a whole, thereby acquitting the filter from being biased towards the force. In addition, displacements are scaled by $\boldsymbol{K}$ in Eq. (2.2.1), which tends to even out error magnitudes in a force equilibrium sense.

Noise level	$\frac{1}{N}\sum_{k=1}^{N}(\boldsymbol{e^p}_k)^T\boldsymbol{e^p}_k$	$\frac{1}{N}\sum_{k=1}^{N}(\boldsymbol{e^f}_k)^T\boldsymbol{e^f}_k$
2%	1211	304
5%	1356	364
10%	1451	505

Table 3.1: Noise levels vs time average SSE.

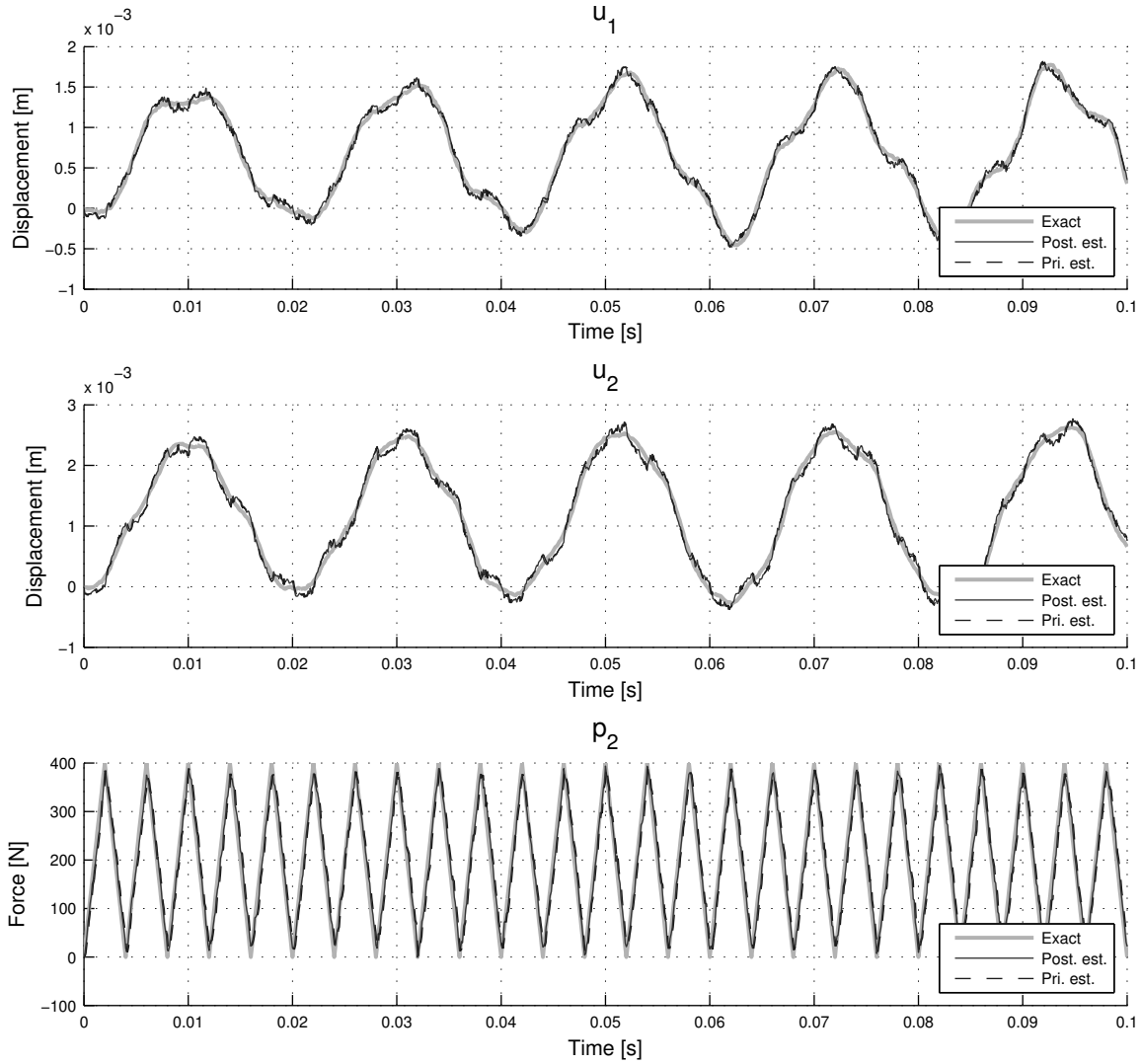

Figure 3.4: State and force estimation at 5% noise.

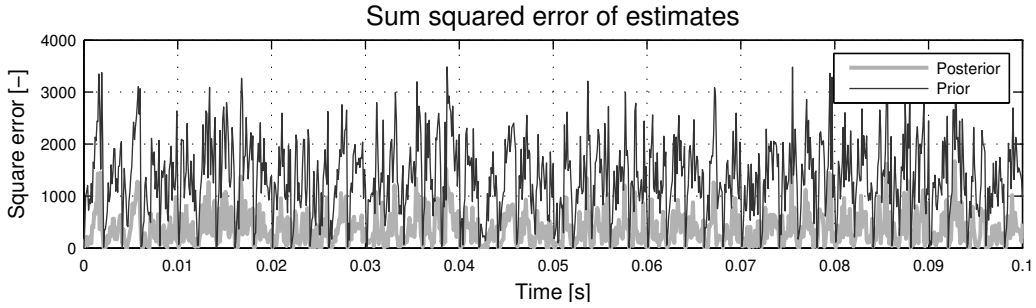

Figure 3.5: Square error of estimates vs time at 5% noise.

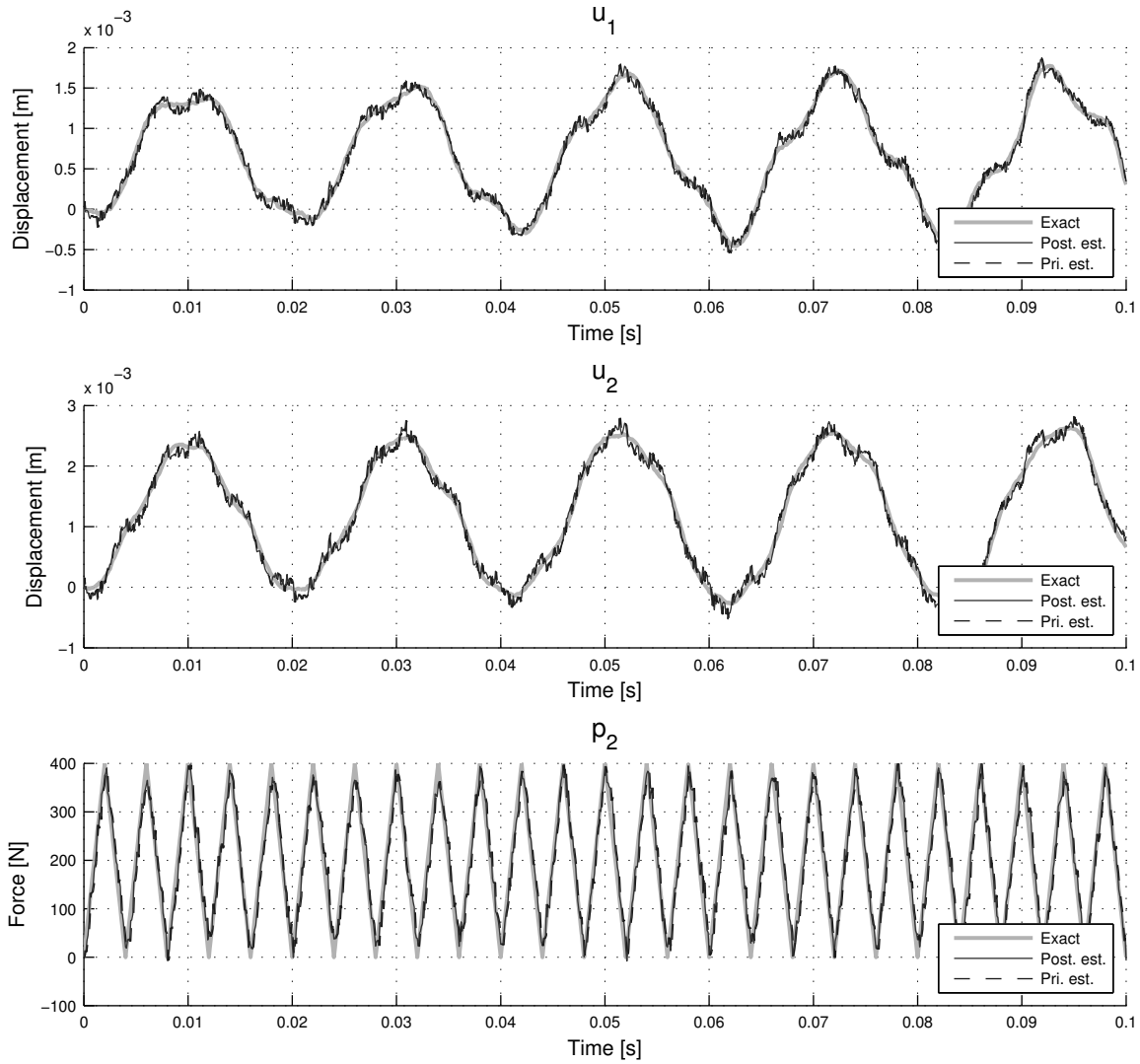

Figure 3.6: State and force estimation at 10% noise.

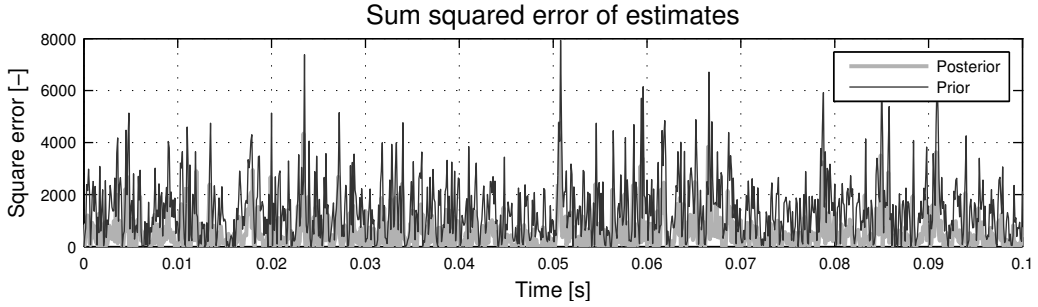

Figure 3.7: Square error of estimates vs time at 10% noise.

The trace of $\boldsymbol{P}_{k|k-1}$ and $\boldsymbol{P}_{k|k}$ in Fig. 3.8 clearly converges after few iterations. Their respective asymptotic values 1.9383 and 2.9384 can be precalculated in accordance with Appendix B. The main difference between the two is associated with $\boldsymbol{S} = 1$. Note that these values are shared by both noise levels, as they do not directly depend on measurements. The measurement updates in u_1 and in the force are graphed in Fig. 3.9. The periodic square wave patterns in velocity and force stems from the periodic force of constant rate. The displacement updates in u_1 differs from this, and its white character can be explained by the domination of white noise added to direct measurements in this variable.

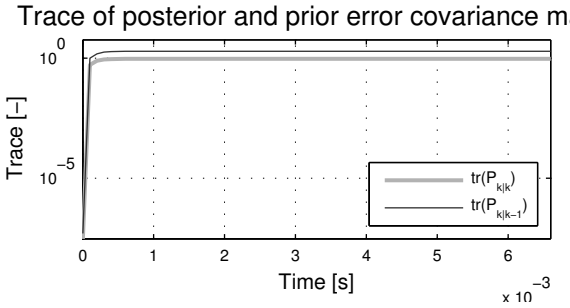

Figure 3.8: Trace evolution, rapidly converging towards steady values.

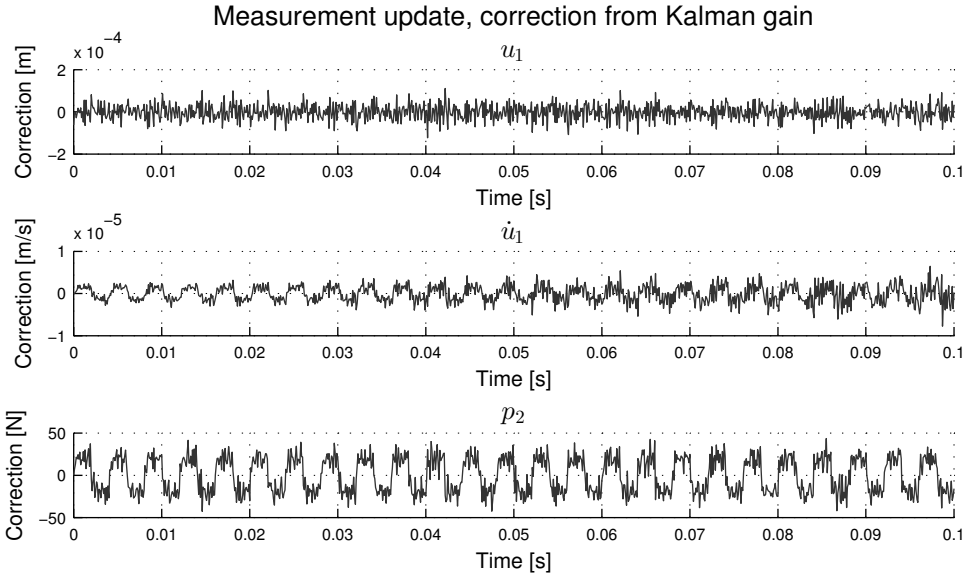

Figure 3.9: Measurement update in Kalman filter for three of the five states at 5% noise.

Additionally, a force random force was identified, with estimates in Fig. 3.10. The force was taken as an actual Gaussian random walk, fulfilling the presumption in Eq. (2.2.17). The force rate variance in generation was 100 N^2 (i.e. $\boldsymbol{S} = 100$), and the observation noise set to 5%.

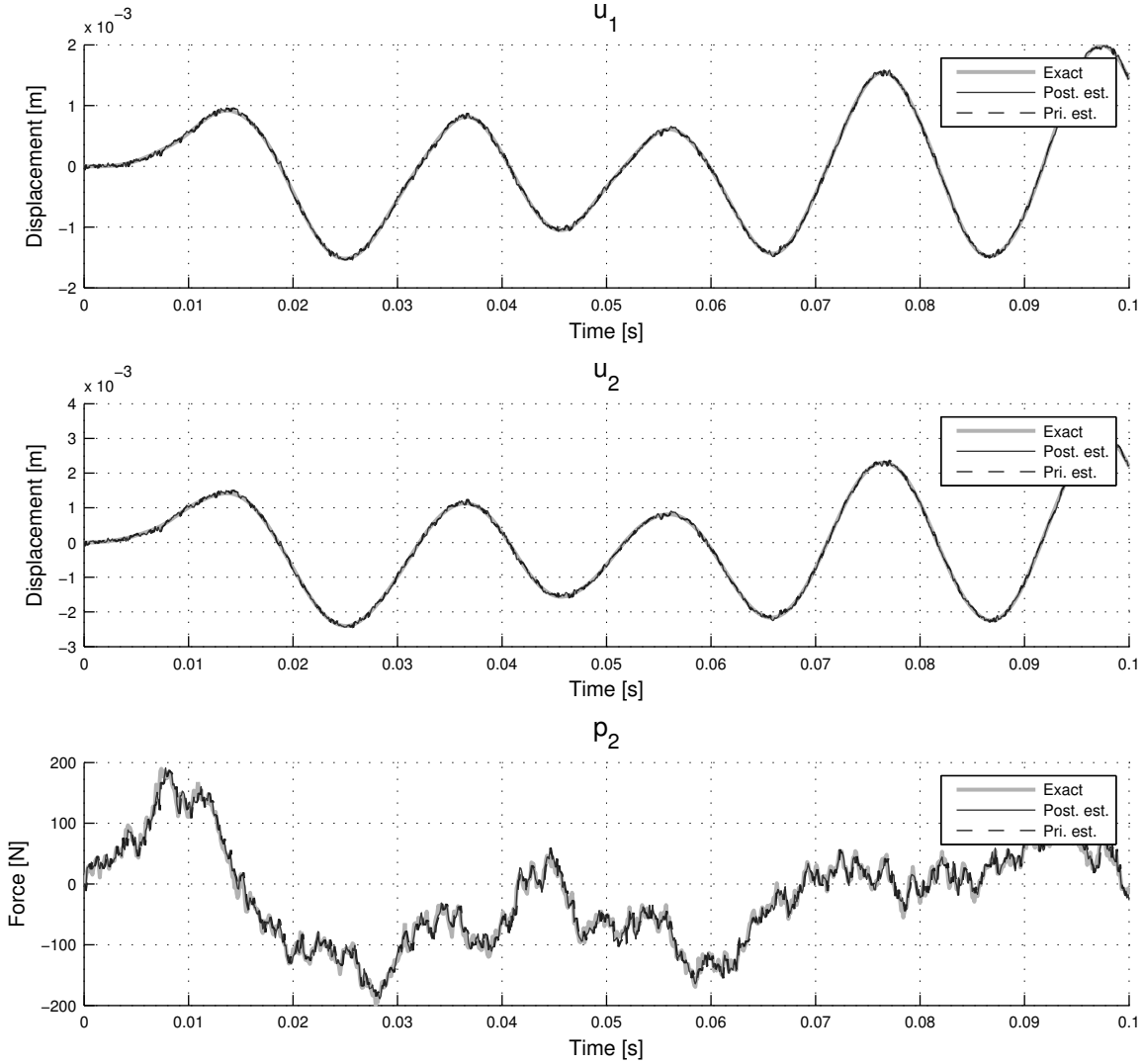

Figure 3.10: State and force estimation of a random force, with 5% noise contamination.

$\boldsymbol{S}$ was still taken as 1 in filtering, meaning the filter was supplied with false information. Refer to Fig. 3.10 for the estimation results. Even when the filter is lied to (here by a factor 100), the force identification is sufficient. Since $\boldsymbol{S}$ is undervalued, abrupt changes in the force (i.e. a Gaussian realization in the tails of the bell curve) is not fully detected,

as a consequence of its statistical unlikeliness in a Bayesian sense. The largest force estimation errors are associated with such high force rates. This agrees with the fact that $\boldsymbol{S}$ can be seen as a form of regularization, controlling the smoothness of the solution [6]. Lourens also explained that given the existence of an optimal $\boldsymbol{S}$-value, the force estimation is relative insensitive to $\boldsymbol{S}$ within an optimal range. For comparison with the triangular force, the force measurement update is graphed in Fig. 3.12, clearly with more white characteristics. The SSE over a short time interval is shown in Fig. 3.11. The effectiveness of the measurement update is clearly visible, especially in reducing large errors in the prior estimate.

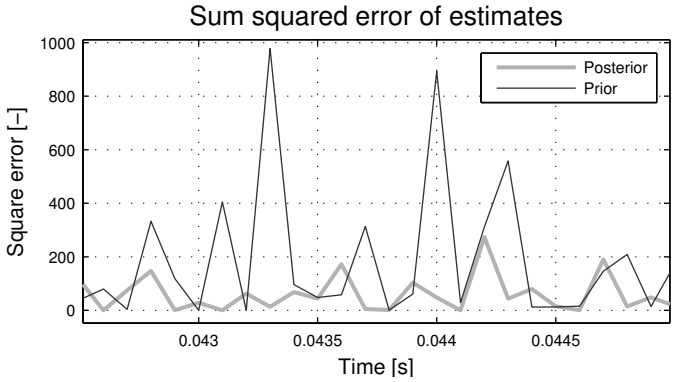

Figure 3.11: Detail of SSE in random force estimation.

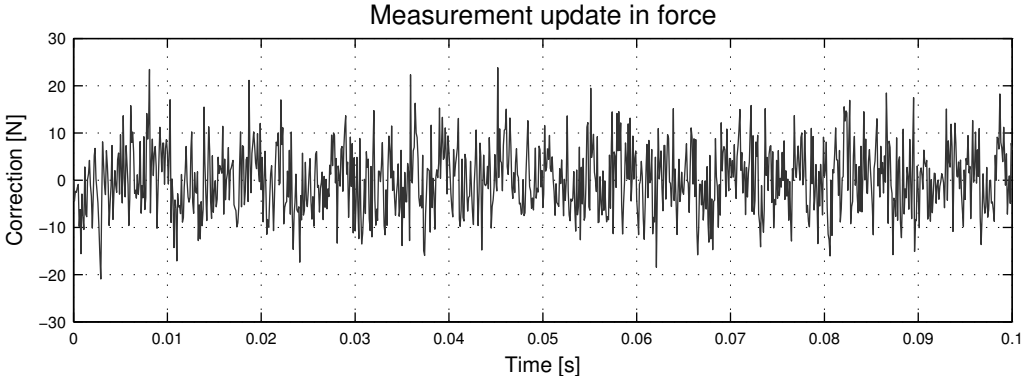

Figure 3.12: Measurement update force correction in the random force case, notably white.

In all, the force identifications on this system can fairly be considered sufficient, as expected. In a larger system, the susceptibility to numerical problems will be higher and

the ratio $\frac{n_d}{n_{DOF}}$ smaller. Although not apparent from the graphs, the estimated force has a small time lag. In numerical cantilever experiments (mentioned in Section 2.6), similar phenomenon was observed by Ma et al. [11], although forces were found from a separate LS scheme and not by a Kalman filter directly. From cross-correlation between the estimated and exact forces, the time lag was found to be three steps. Time series were therefore shifted manually by Ma et al. before evaluating errors. This principle can be crucial, supported by hypothetical case in Fig. 3.13. As a consequence of time lag, the SSE in estimate 2 is approximately twice than for estimate 1. Contrary one could still argue estimate 1 represents a better identification, as it fits the exact curve quite well if time shifted.

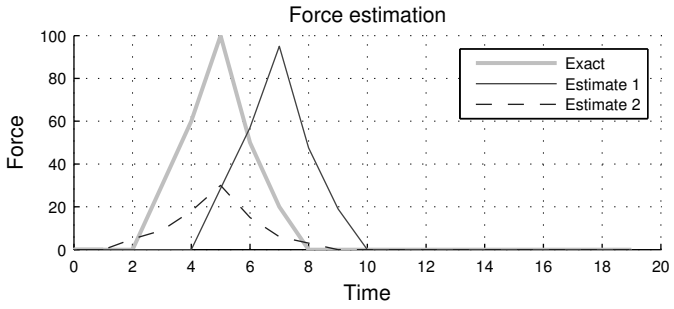

Figure 3.13: Two hypothetical force estimations.

3.2 Impact force on simply supported beam

3.2.1 Setup and model

A simply supported aluminum (alloy 6082 T6) beam (with end overhangs) were set up in the laboratory, with the purpose of identifying a single impact force. This force originated from a hammer with an internal load cell (Brüel & Kjær 8208 Modal sledge hammer, sensitivity 0.225 mV/N). The setup is pictured in Fig. 3.14. Material and mechanical properties are listed in Table 3.2. The H-cross section geometry was measured by a vernier caliper. Any entailing inaccuracies was neglected and left to later calibration and model noise. The beam rested on steel trestles fixed with 70 kg dead weight. F-clamps on the lower flanges were used to pin the beam at supports, taken as zero rotational constrain.

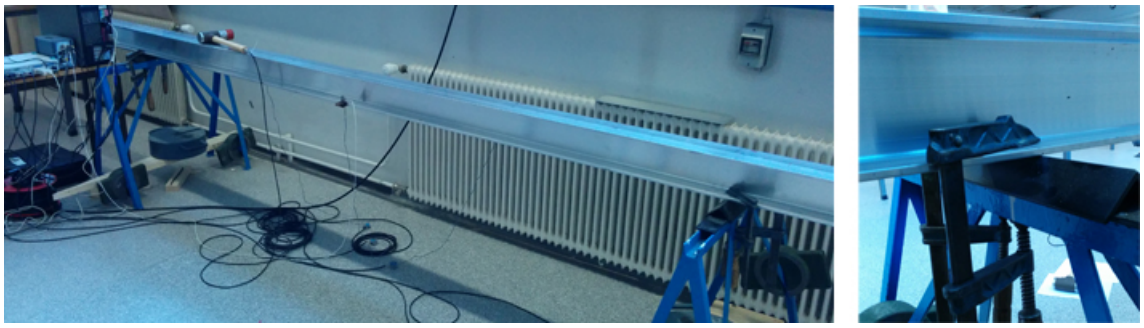

Figure 3.14: Left: beam rigged in laboratory. Right: detail of pinned support.

A_x (Axial area)	1.86×10^3 mm^2	Elastic modulus	69.0 GPa
A_y (Vertical shear area)	4.20×10^2 mm^2	Shear modulus	25.5 GPa
A_z (Lateral shear area)	1.44×10^3 mm^2	Poisson's ratio	0.35
I_{yy} (Weak axis)	1.73×10^6 mm^4	Density	2700 kg/m^3
I_{zz} (Strong axis)	5.16×10^6 mm^4	Distance NA-max y	60 mm
I_t (Torsion)	1.88×10^4 mm^4	Distance NA-max z	60 mm

Table 3.2: Beam properties.

A FE model was created, discretizing the beam evenly in elements of length 125 mm,

whose mesh is visualized in Fig. 3.15. To gain the mass and stiffness matrices, C^1-continuous elements were used. These are based on Timoshenko beam theory with cubic shape functions and accounts for shear flexibility [27]. The reason for generating system matrices manually and not via FE software is due to strain compatibility. Exact shape functions are needed in the strain-displacement relation derivation establishing $\boldsymbol{S_d}$. In FE software, these are often not elucidated, export of matrices is not available or hidden internal nodes are added beyond the user's insight.

Figure 3.15: Mesh of FE model, with node numbering from 1 to 33. Support nodes 5 and 29 marked together with strain observation nodes.

Boundary conditions were enforced by removing the translational DOFs at the supports from the system matrices entirely rather than assigning large stiffness. The latter would raise the condition number of $\boldsymbol{K}$ thereby cause numerical problems. Removing elements obstructed the original uniform DOF numbering, calling for an automatic metadata scheme to keep track of the right DOFs in analysis. Although the system matrices were initially assembled in a 3D formulation, all axial, torsional and weak axis bending DOFs were condensed out to speed up computations, greatly depending on matrix dimensions. Therefore, unless stated otherwise, all modes referred to subsequently are strong axis excitations.

Three strain gauges, whose fixed positions on the lower flange can be seen in Fig. 3.16, together with a movable accelerometer were taken as observations. Both sensor types are pictured in Fig. 3.17. The accelerometer were of type Kistler (8703A50M5, sensitivity 10 $\mathrm{mV/g_n}$, range ± 50 $\mathrm{g_n}$). $\boldsymbol{S_d}$ was constructed as described by Nord et al. [28].

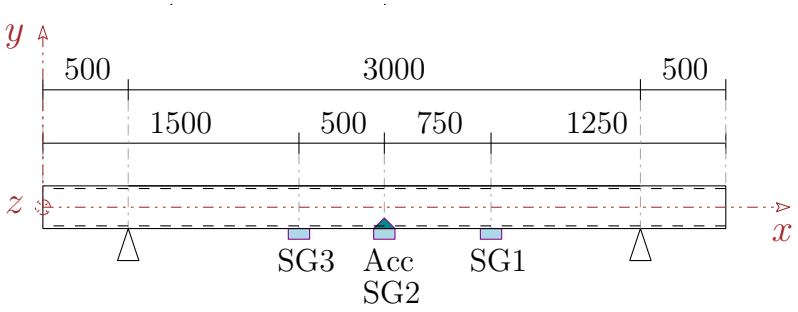

Figure 3.16: Placement of strain gauges. The accelerometer is here placed in the middle. All dimensions in mm.

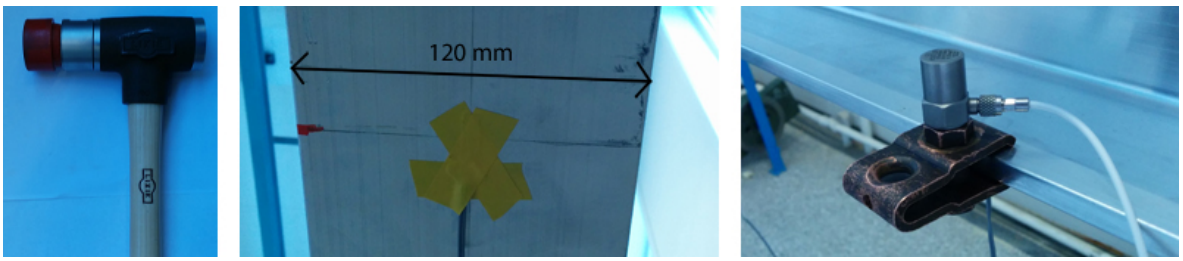

Figure 3.17: Left: Modal hammer. Middle: strain gauge glued to underside of the lower flange and secured with tape. Right: accelerometer clamped to lower flange.

3.2.2 Initial calibration and preparations

Static calibrations of strain gauges were performed by loading the beam midspan with 10, 30, 60 and 68 kg. The strain readings were compared to the theoretical value in the lower flange by Euler-Bernoulli beam theory, whose result is tabulated in Table 3.3. Average values over an extended time were used to eliminate noise contributions, discussed further below. From this it was found the strain gauges gave severely undervalued readings. All strain readings were therefore upscaled by 40% (error ratio mean) in calculations. The source of this defect remains unclear, but it is likely the strain-voltage gauge factor was wrong.

Initially it was evident the strain readings were particularly noisy and it was not clear if identification was practically viable, even with stochastic methods, let alone deterministic methods. To illustrate, sampling at 1200 and 2400 Hz, the strain noise midspan had approximate "amplitude" 2×10^{-6} and 4×10^{-6}. This is equivalent to a 1.5 and 3 kg static

	Ratio theoretical/measured strain		
Load [kg]	SG1	SG2	SG3
10	1.40	1.33	1.29
30	1.38	1.56	1.40
60	1.38	1.46	1.38
68	1.34	1.43	1.36

Table 3.3: Static calibration of strain gauges.

load, respectively, which must be regarded as considerably strong disturbance. The noise was found to increase severely with sampling frequency, such that the real strain values from a 1000 N force at 4800 or 9600 Hz would practically drown and be inseparable from the noise. Sampling was therefore limited to 1200 and 2400 Hz. All measurements were detrended before analysis in the sense of removing the noise mean to eliminate uncontrollable initial offsets. Noise variance sampled at zero load was found to be $\sim 1 \times 10^{-14}$.

To find the noise source, or at least investigate its characteristics, a frequency trans-

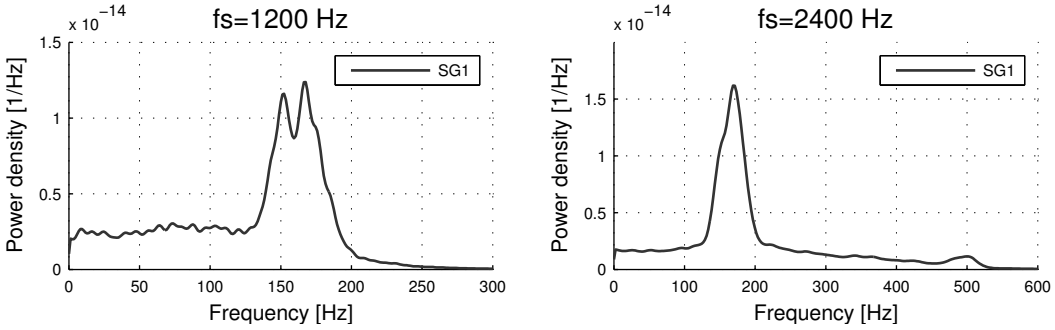

Figure 3.18: Welch power spectrum estimate of noise.

formation were done. A power spectral density chart is seen in Fig. 3.18. The noise is seemingly prominent in the frequency range 130-200 Hz. This could indicate the beam *is* excited when at "rest", thus noise not coming from the measurement equipment itself. To eliminate this possibility, the beam was loaded with 50 kg midspan, lowering the natural frequencies (discussed later this section) f_1 by 59% and f_2 by 23%. With the noise spectrum not changing in this setup, it was concluded the noise did not origin from system

modes. Upon closer inspection it was also discovered the noise in SG1, SG2 and SG3 was all correlated with coefficient $r \approx 0.85$. This strong interdependence suggests electrical wiring configuration is the source. The capability of handling fast sampling dynamics was also likely limited. The acceleration noise was uncorrelated with the others ($r < 0.01$). The strain was also observed to be sensitive to simple mechanic interaction (e.g. walking or door slams) in near proximity, meaning traffic or ventilation could be prominent external disturbances. It is important to remember the test environment here was quite controllable, contrary to a real structure, so one might as well accept such circumstances.

The natural frequencies were found from frequency analysis of free vibrations induced by a load ensured to excite the first three modes. These were compared to the (undamped) eigenfrequencies from the FE model. $\boldsymbol{K}$ were then scaled such that f_1 coincided with its empirical equivalent. This equals scaling the elastic modulus directly. The calibrated frequencies is listed in Table 3.4. Errors in higher modes were not treated further, as system identification was not the main objective per se. Moreover, the first mode is the main contributor during vibrations. This method is feasible and just as simple for real structures, whose susceptibility to model errors is unavoidable.

No.	Measured [Hz]	FE, unscaled $\boldsymbol{K}$ [Hz]	Error [%]	FE, scaled $\boldsymbol{K}$ [Hz]	Error [%]
f_1	42.8	45.1	-5.6	42.8	0.0
f_2	157.8	162.8	3.2	154.5	-2.1
f_3	297.4	292.4	-1.7	277.4	-6.7

Table 3.4: Calibration of natural frequencies.

The scaled stiffness matrix was used throughout analysis. The associated lowermost mode shapes can be seen in Fig. 3.19. Notably, the second mode has zero amplitude midspan, while for the third the same occurs at third points. Sensors placed at zero points of modes will not be able to observe the corresponding mode. All four lowermost modes have at least two sensors at nonzero nodes.

The damping matrix was created from Rayleigh damping (i.e. mass and stiffness propor-

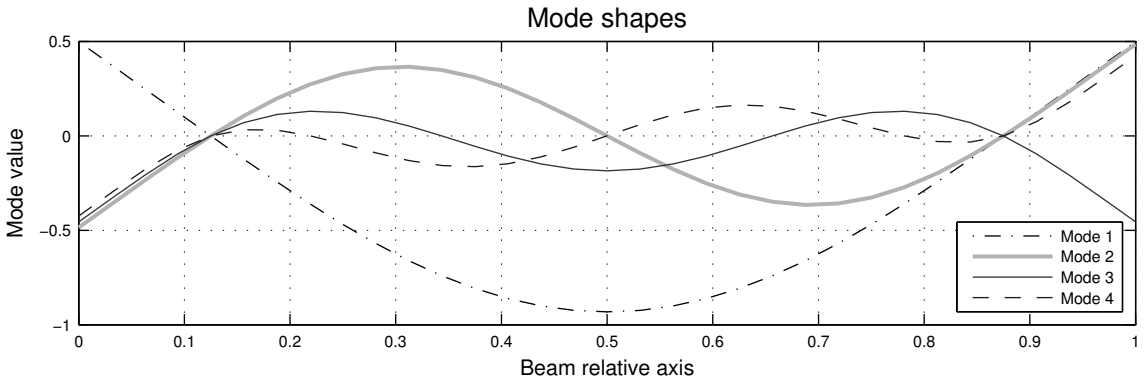

Figure 3.19: First four modes of the beam. Note the alternating symmetry/antisymmtry.

tional damping) [29], fed with the frequencies 42.8 and 154.5 Hz and assumed 1% critical damping.

3.2.3 Conventional force identification

A forward solution was found from the measured hammer forces (using Eq. (2.2.11)), in turn generating measurements (using Eq. (2.2.13)), back-calculating the force with the Kalman filter. 5% noise was added to the generated observations by the method in Section 3.1.1. The assumption of a piecewise linear force (first order hold) can be seen in Fig. 3.20 to have great significance. Over the impact duration, the generated acceleration data has severe errors for the zero order hold case ($\boldsymbol{F} = \mathbf{0}$) because of high force rates. Even though only the real measurements are ultimately used in force identification, comparisons are important to gauge performance. The generated data from on a first order hold decently traces the real measurements throughout the series. Although not shown here, the same phenomenon occurred at 2400 Hz with local relative errors of $\sim 500\%$.

Identifications termed "aXX-pYY-fZZZZ" refer to accelerometer and force located in node XX and YY, respectively, sampled at ZZZZ Hz. First, a series of identifications with varying force location and accelerometer fixed midspan is presented. All available observational data (acceleration and three strains) were included. Identification with reduced amount of sensors is discussed in Section 3.2.5. A numerical measure of error, e.g. SSE, was considered unfeasible here. Numerically comparing different series would require a

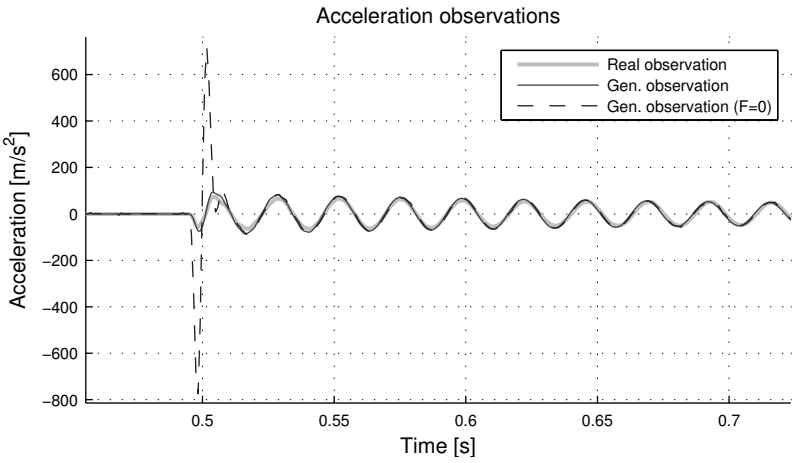

Figure 3.20: Comparison of real and generated measurement data at 1200 Hz sampling. Force and accelerometer collocated midspan (node 17).

standard establishing equal conditions with respect to noise, time series length, as well as the location, duration and magnitude of the hammer impact. Accepting that fully eliminating bias was not practically possible, the quality of the force identification were rather judged by the analyst.

$\hat{\boldsymbol{x}}^a_{0|-1}$ was unbiasedly supplied as $\mathbf{0}$, and $\boldsymbol{P}_{0|-1}$ as $\boldsymbol{I} \times 10^{-10}$. $\boldsymbol{Q}$ was set to $\boldsymbol{I} \times 10^{-14}$, and $\boldsymbol{R}$ to diagonal 10^{-14}, with 0.85×10^{-14} on the strain cross terms to accommodate for the correlated noise. $\boldsymbol{S}$ was calibrated to 10. Impacts were commenced in the middle, collocated with accelerometer, moving towards the end, striking in node 15, 13, 11, 08, and 02, see Fig. 3.21. Nodes opposite remained untouched due to near symmetry.

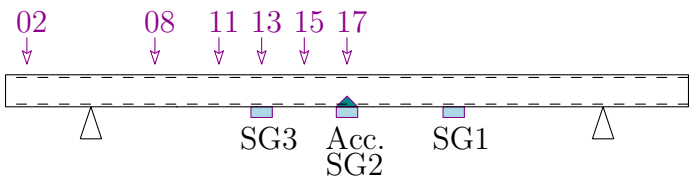

Figure 3.21: Nodes hit with hammer.

The resulting force estimations is shown sequentially in Fig. 3.22 – 3.29 for both 1200 and 2400 Hz. Any difference between the two sampling frequencies are hard to distinguish. The advantages of faster sampling is balanced with increase in noise. The best results are obtained with collocated force and accelerometer. Lack of impact amplitude recognition is

seemingly a larger problem than the opposite (overestimation). While there is generally good agreement between the measured and estimated forces during impact, there are prominent force fluctuations before and after. This can be contributed the particularly noisy strains. Larger fluctuations subsequent to impact is a phenomenon also observed by Lourens [6] among others. Fluctuations are also present in the force estimate from generated observations, but with smaller magnitude, and mostly as a result of the 5% generated noise, which *is* white. The same phenomenon mentioned on the random load in Section 3.1.2 can be observed here, but more clearly: if $\boldsymbol{S}$ is taken too low, the full amplitude of the impact is not recognized. The easiest way of resolving this is by increasing $\boldsymbol{S}$, but comes at the cost of larger fluctuations, since $\boldsymbol{S}$ regulates the expected force rate intensity. Alternatively, one could customize an intelligent time-varying $\boldsymbol{S} = \boldsymbol{S}_k$ for this case. Initially letting $\boldsymbol{S}_k = 1$, followed by an increase when impact is detected (e.g. predicted force $\hat{\boldsymbol{p}}_{k|k-1} > 100$ N), and resetting to 1 in the free vibration phase. This type of approach could certainly reduce errors, but requires information on the force prior to analysis, which may not be obtainable.

In case p17 and p13 the estimates from real observations perform better than estimates from generated observations, seemingly contra intuitive since the latter is just a back-calculation of the force. The incidents can be explained by information supplied to the filter (e.g. noise magnitude and correlation) are mainly calibrated to accommodate for the real observations. Both these cases notably also benefits from collocation. Identification case p02 was expected to be most difficult, with the force located beyond the support. Although this node should have little influence on the accelerometer, it has significant amplitude in the first mode, at least guaranteeing first mode excitations, meaning some acceleration signal will be registered. Strikingly, the force is decently identified, with results similar to case p08 and p11. Referring to Fig. 2.8 and related discussion, it remains unknown how a finer mesh would affect the estimation.

There is seemingly also increasing time lag and reduction in amplitude with moving towards the beam end. The lag is a common feature for identifications with increasing force-sensor distance, and finite elastic wave speed inputs causes a delayed influence on

sensors [6]. The number of lag steps can be assessed as $n_{lag} = \frac{s\, f_s}{v_{al}}$, with s as the force-sensor distance and $v_{al} \approx 3000$ m/s, amounting approximately 1.5 steps for case a17-p02-f2400. This corresponds to 10% of the load duration and is close to the difference between the real and generated estimate in Fig. 3.29. Seeing that the estimation from generated observations, which effectively has infinite wave speed, also suffers from time lag, the problem mainly lies within the filter itself. The reduction in amplitude can also be caused by the proximity to the supports. The supporting steel trestles were observed to vibrate slightly, meaning some energy is dissipated. Real observations was also found smaller than their generated counterparts for case p02, further approving this belief. The problem therefore relates to the model, or arguably the laboratory setup, and not the methods themselves.

The force frequency spectrum is shown for case p17 and p15 in Fig. 3.23 and 3.25, displaying similar characteristics. The estimated force has more spurious noise-like contributions in the low frequency range compared to the measured force. Mismatch in magnitude is largely present for components above 300 Hz, but constitute low values and are beyond the third mode, thus having little impact on the system.

The largest transmission zeros in the six cases presented here were in the order of $\lambda_{max} \sim 10^{-9}-10^{-6}$. Recalling from Section 2.5.2 its influence on stability, convergence in inversion can be considered good and any unstable parts are practically unnoticeable after few steps. Although not explicitly shown here, the same is displayed in $\mathrm{tr}(\boldsymbol{P}_{k|k})$, rapidly converging to its asymptotic value, ranging approximately $25 - 65$. Good stability is also expected with using all available measurements.

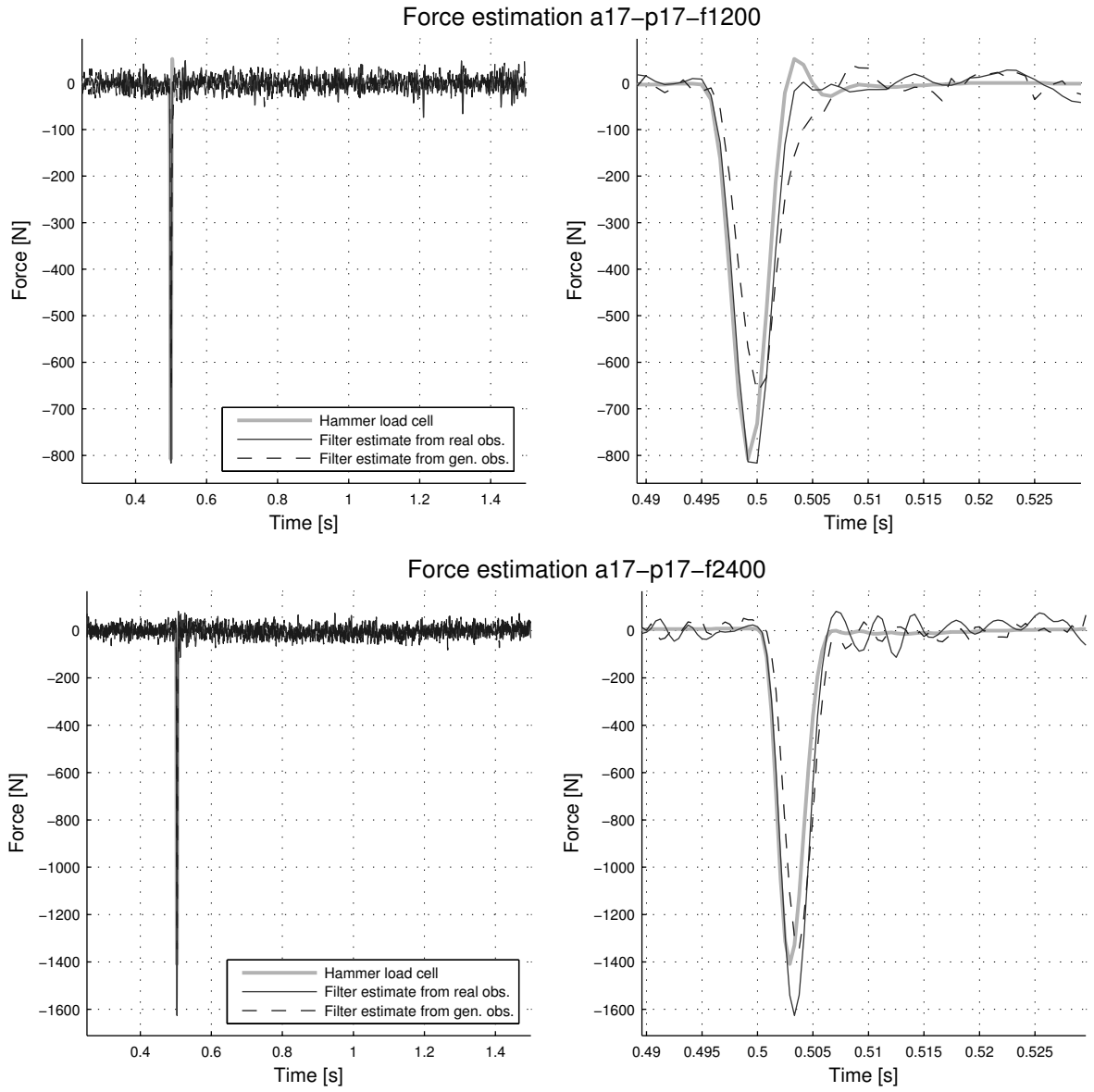

Figure 3.22: Estimation of force in node 17. Collocated with accelerometer and SG2.

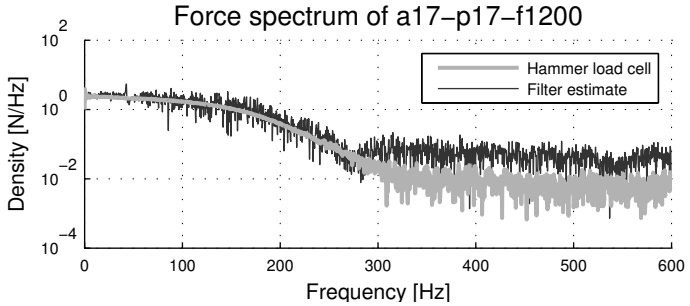

Figure 3.23: Force spectrum comparison at 1200 Hz sampling.

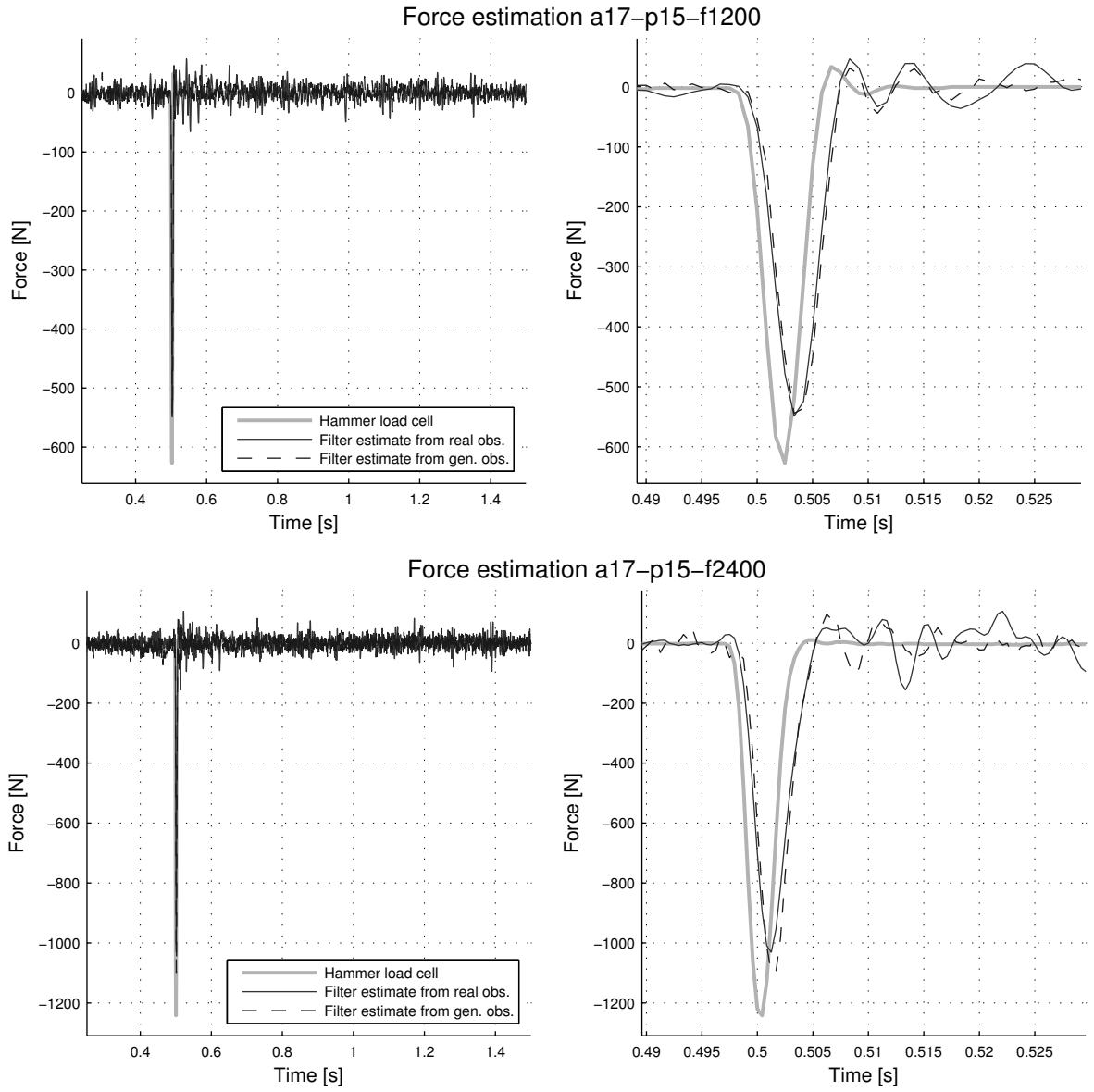

Figure 3.24: Estimation of force in node 15.

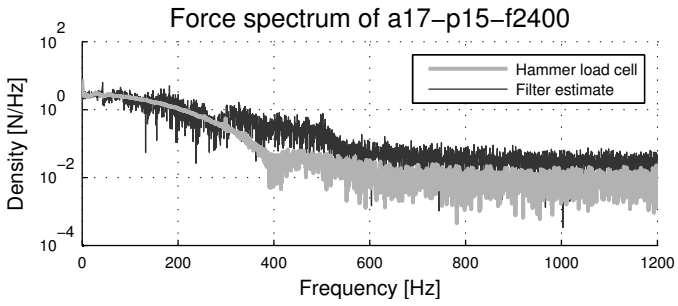

Figure 3.25: Force spectrum comparison at 2400 Hz sampling.

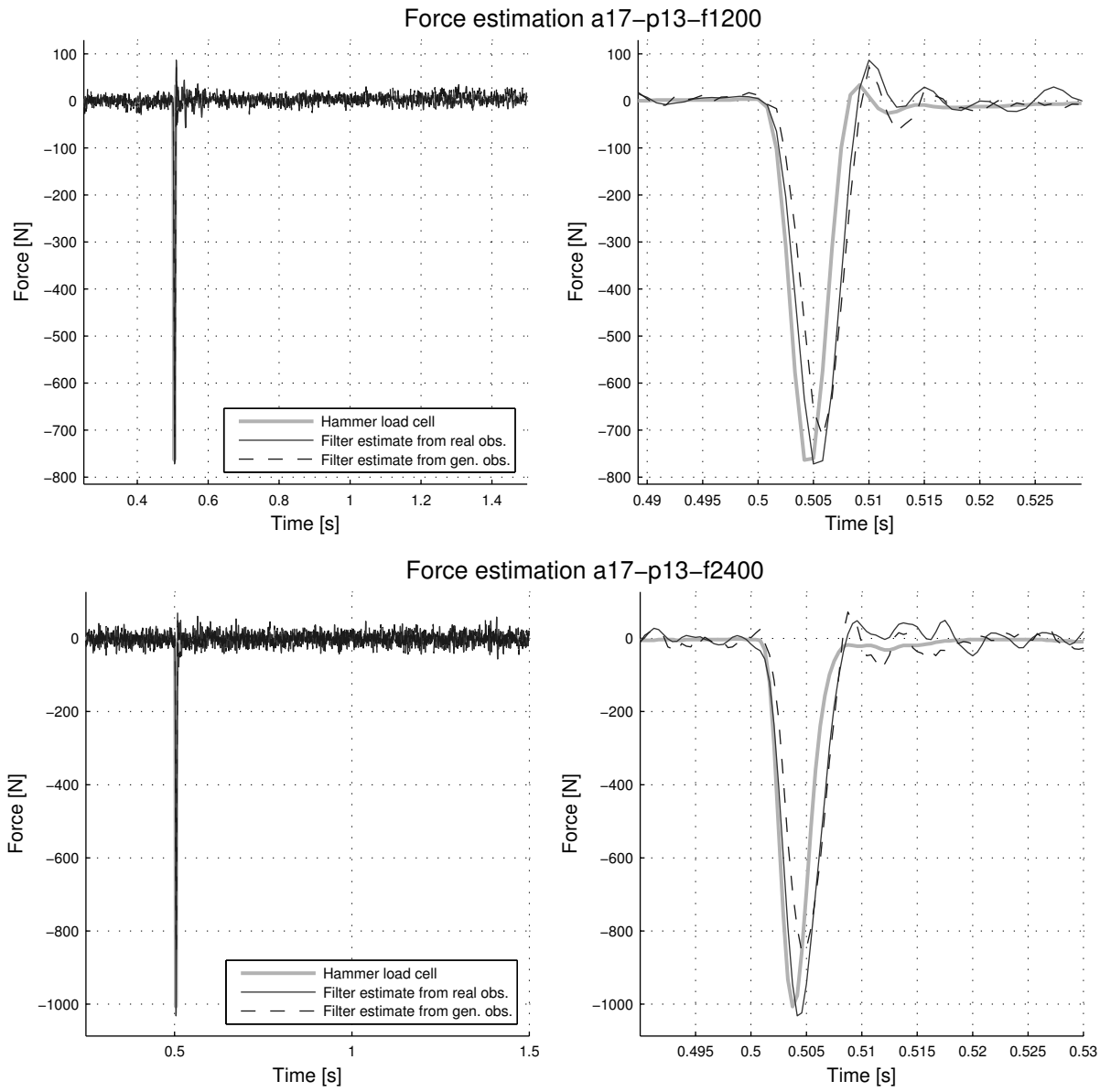

Figure 3.26: Estimation of force in node 13. Collocated with SG3.

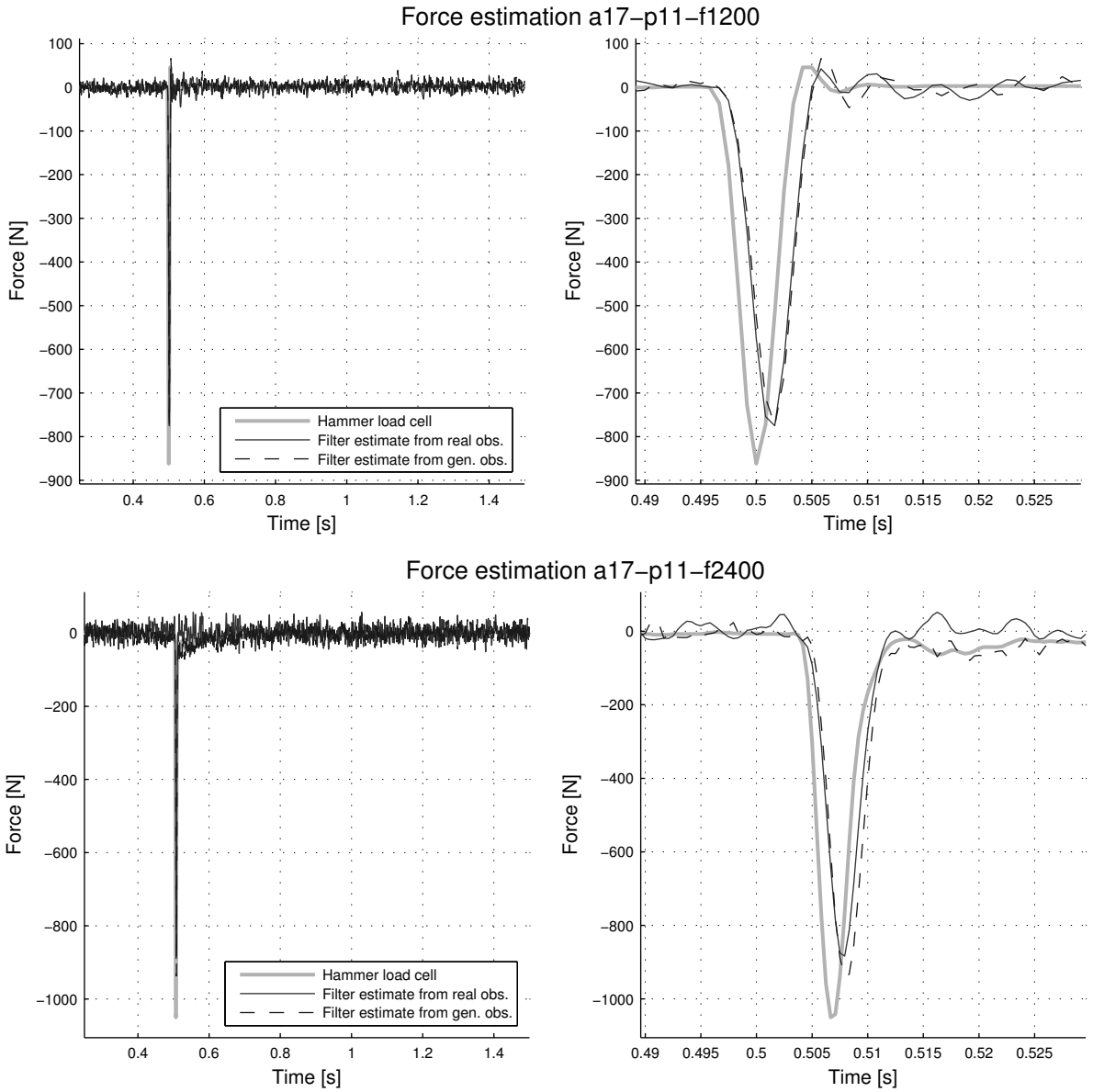

Figure 3.27: Estimation of force in node 11.

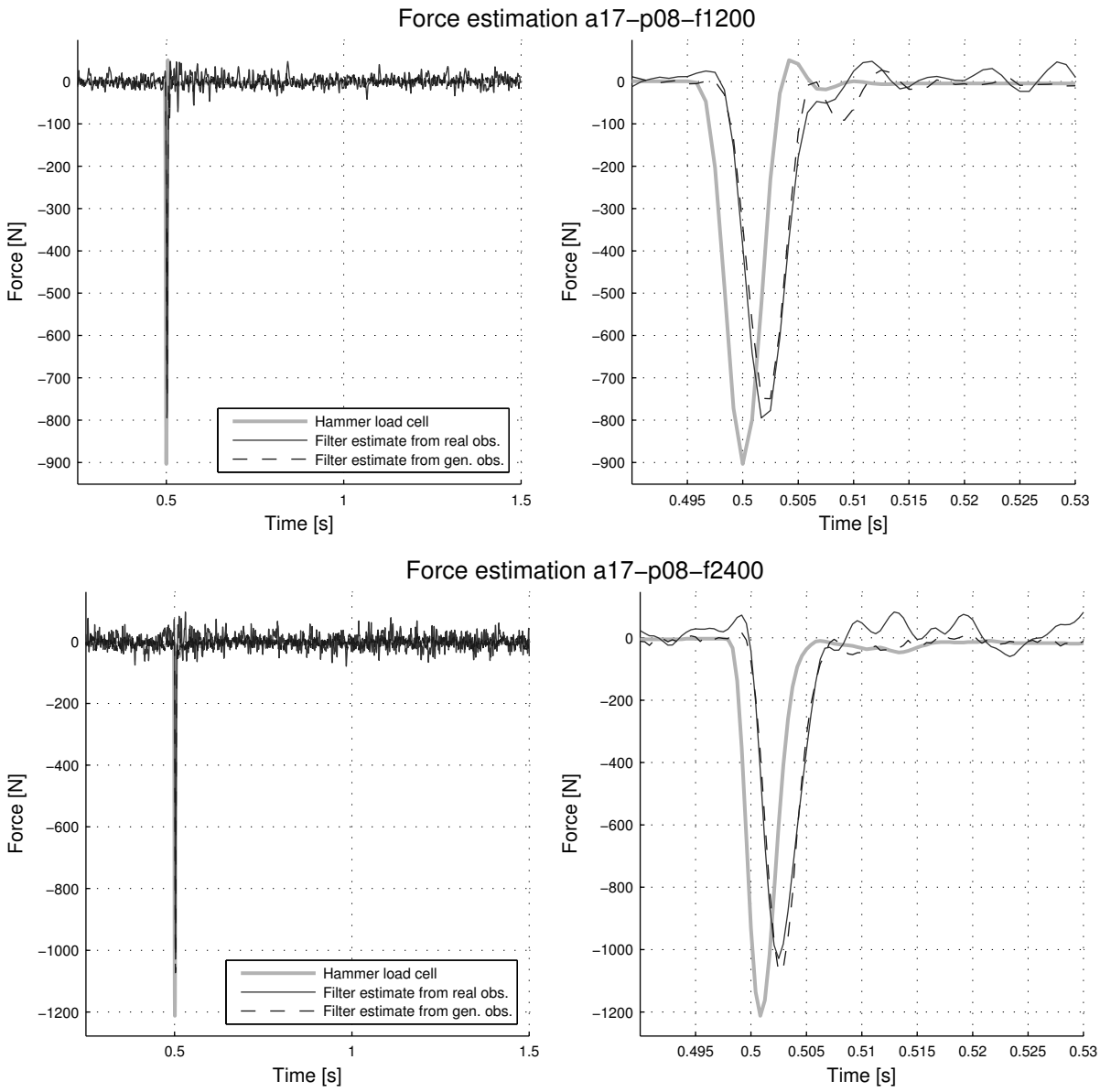

Figure 3.28: Estimation of force in node 08.

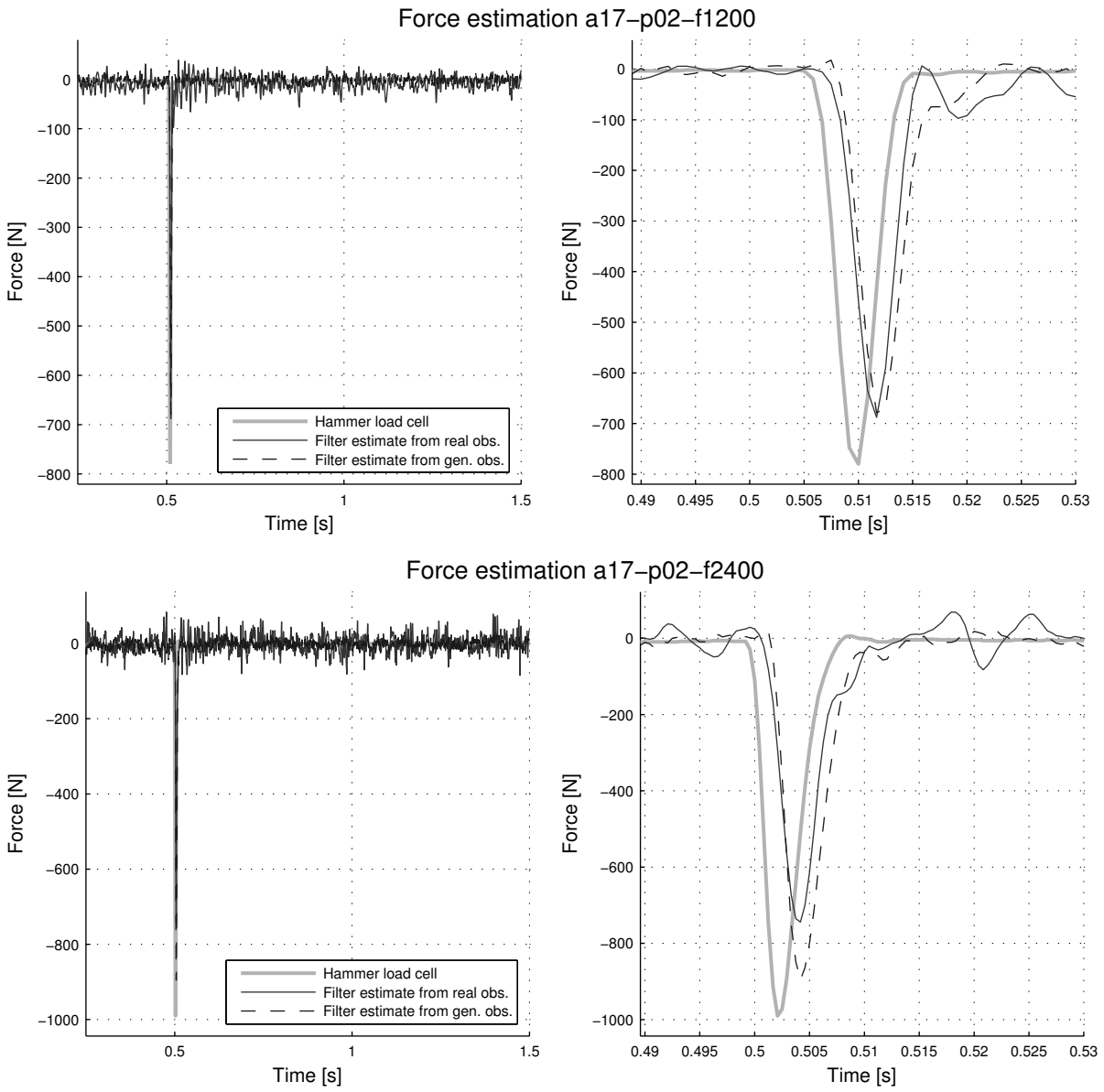

Figure 3.29: Estimation of force in node 02.

The estimation of displacements and velocities are of lesser interest here, but worth mentioned briefly and inspected for their general correspondence with the forward solution. If the impact duration τ is short compared to the first natural period T_1, the total force impulse $\int_0^\tau p(t)\,dt$ will be more important than amplitude or time lag concerning response. The displacement after impact will be in the order of τ^2, but the velocity is one order lower (τ), hence the system response can be treated as free vibrations caused by an initial velocity $\approx \frac{1}{M^*}\int_0^\tau p(t)\,dt$. In the case examined here $\frac{\tau}{T_1} \approx 3-5$, thus not adhering fully to this principle. The displacements for cases a17-p13-f2400 and a17-p02-f2400 is shown in Fig. 3.30 and 3.31, respectively. The estimates quite agree with the forward solution in the former, as expected with accelerometer proximity and collocation with SG3. In the latter, both first and second mode vibrations are recognized, although the second quickly diminishes. Amplitudes does not fully concur, partly attributed to the aforementioned energy dissipation at supports. The advantage of calibrating the model to get f_1 right is apparent, very little phase lag is acquired throughout the history. Velocities are not shown here, but had similar relative accuracy. In all, the state estimation must be considered sufficient.

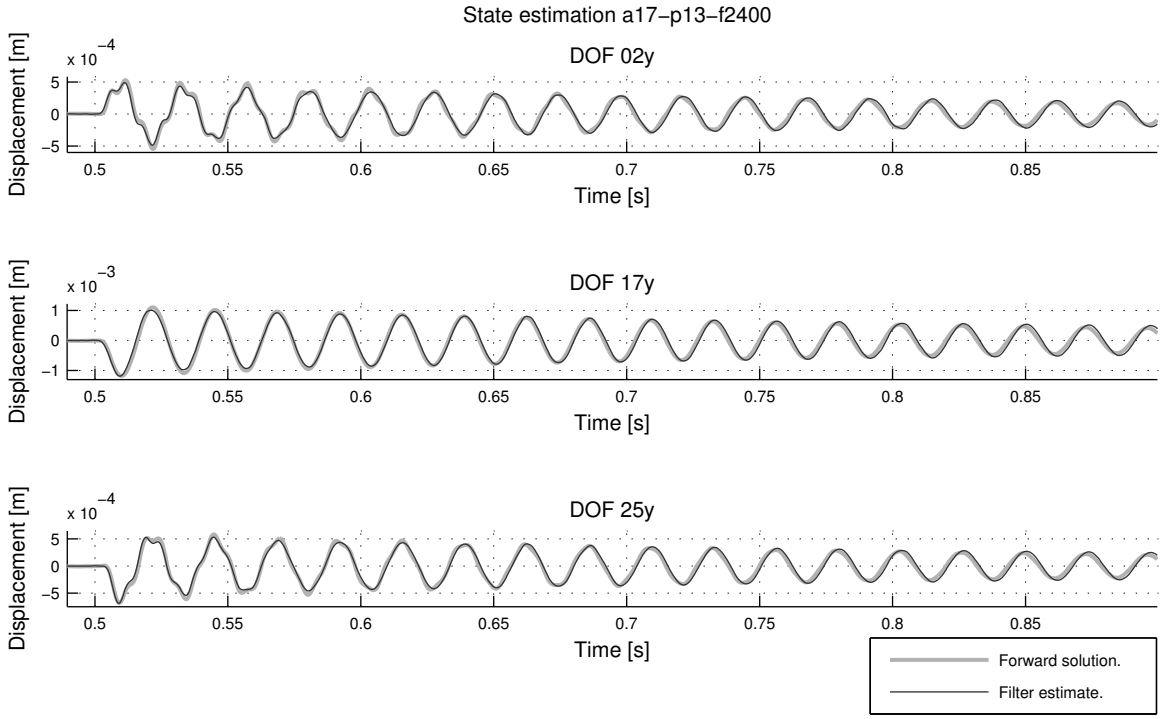

Figure 3.30: State estimation of selected DOFs for case p13. Collocated with SG3.

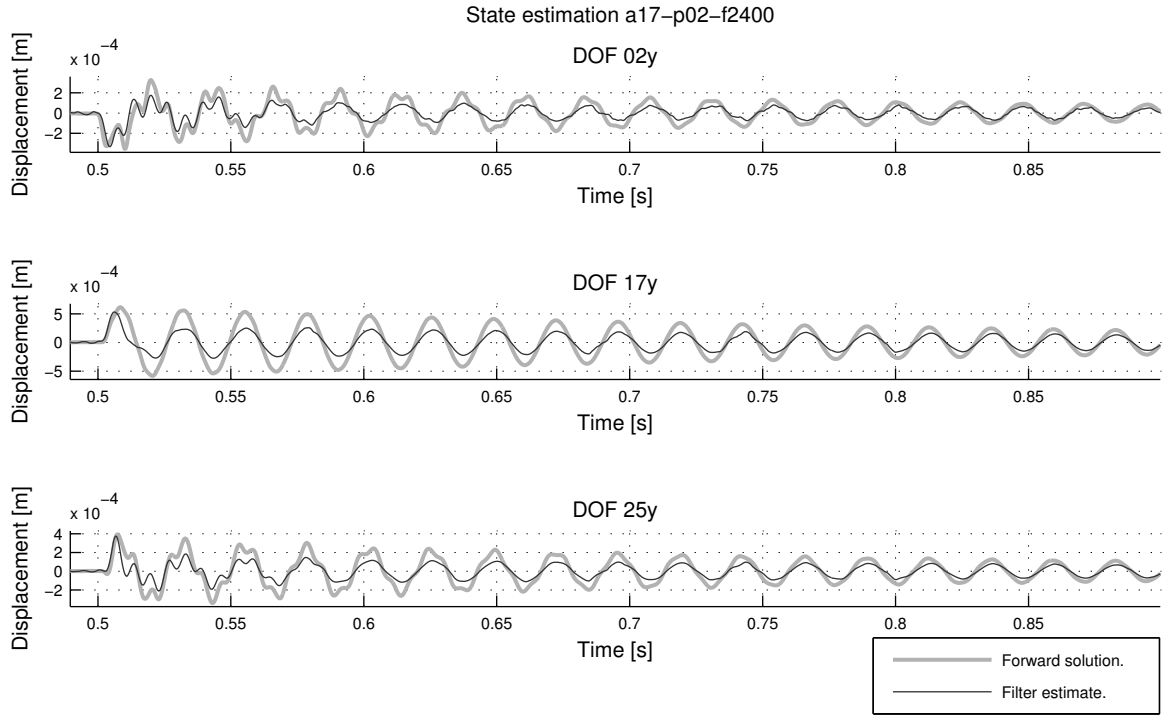

Figure 3.31: State estimation of selected DOFs for case p02.

3.2.4 Parameter study: model uncertainty

Real structures can be difficult to model because of sheer structural complexity. For this reason, a parameter study was performed. The purpose was to investigate the effect of modeling errors on the force identification. By such errors lies the main interest in stiffness and mass deviations. Deviations in system matrices cannot be inflicted as Gaussian variables directly, even if symmetry is maintained, due to high eigen-sensitivity. Naive random contributions causes loss of positive definiteness, and forms negative or imaginary eigenvalues. A as remedy, a Wishart distribution (multivariate Gamma distribution) was used. For the details omitted here, refer to works by Adhikari [30]. The undistorted mass and stiffness matrices are here termed $\boldsymbol{M}_0$ and $\boldsymbol{K}_0$. Their distorted equivalents $\boldsymbol{M}$ and $\boldsymbol{K}$, in this context by definition random variables, are unbiased, i.e. $\boldsymbol{E}(\boldsymbol{M}^{-1}) = \boldsymbol{M}_0^{-1}$ and $\boldsymbol{E}(\boldsymbol{K}^{-1}) = \boldsymbol{K}_0^{-1}$. Furthermore, the DOF-parameter in the Wishart PDF were chosen such

that same is true for the inverse: $\boldsymbol{E}(\boldsymbol{M}^{-1}) = \boldsymbol{M}_0^{-1}$ and $\boldsymbol{E}(\boldsymbol{K}^{-1}) = \boldsymbol{K}_0^{-1}$. Symmetry is also maintained. The level of distortion, measured by the normalized standard deviation (defined by the Frobenius norm) were supplied as:

$$\sigma_M^2 = \frac{\boldsymbol{E}(||\boldsymbol{M} - \boldsymbol{M}_0||_F^2)}{\boldsymbol{E}(||\boldsymbol{M}_0||_F^2)} = 0.1^2 \qquad \sigma_K^2 = \frac{\boldsymbol{E}(||\boldsymbol{K} - \boldsymbol{K}_0||_F^2)}{\boldsymbol{E}(||\boldsymbol{K}_0||_F^2)} = 0.1^2$$

The damping matrix, likely already inaccurate, was regenerated via Rayleigh damping, and not treated further. 10 Wishart realizations were generated and run on case a17-p02-f2400 and a17-p13-f2400, deliberately chosen as non-collocated with accelerometer to challenge the filter. To better illustrate the distortion level, the matrix element ratio sample standard deviations were found to be:

$$S_\sigma\left(\frac{M_{ij}}{M_{0,\,ij}}\right) = 0.0688 \qquad S_\sigma\left(\frac{K_{ij}}{K_{0,\,ij}}\right) = 0.0575 \qquad i,j = 1,2\ldots n_{DOF} \quad (M_{0,\,ij}, K_{0,\,ij} \neq 0)$$

which is a reasonable from a practical perspective. Likewise, deviations from the original (FE-model) natural frequencies $f_{0,\,i}$ were:

$$S_\sigma\left(\frac{f_1}{f_{0,\,1}}\right) = 0.0190 \qquad S_\sigma\left(\frac{f_2}{f_{0,\,2}}\right) = 0.0204 \qquad S_\sigma\left(\frac{f_3}{f_{0,\,3}}\right) = 0.0193$$

Covariance matrices remained as $\boldsymbol{R} = \boldsymbol{I} \times 10^{-14}$ and $\boldsymbol{S} = 10$. To obtain the best results, $\boldsymbol{Q}$ was calibrated to $\boldsymbol{I} \times 10^{-13}$ to accommodate for model errors, one magnitude increase from the preceding section. Compared to the undistorted model, the estimations seen in Fig. 3.32 and 3.33 are able to recognize the impact force quite well. If the objective is purely limited to impact identification, the results are satisfactory. The distorted models have an one step time lag compared to the undistorted and the amplitude is consistent. The largest inconvenience is the ringing subsequent to impact, which must regarded severe and clearly varies with each realization. This can be explained by the model error directly. The system does not vibrate as anticipated by the model since change in mass and stiffness gives deviations in frequency and phase. The algorithm therefore imposes a correction by presuming this is caused by an external force with harmonic characteristics. Since the ringing clearly origins from model errors here, this suggests the

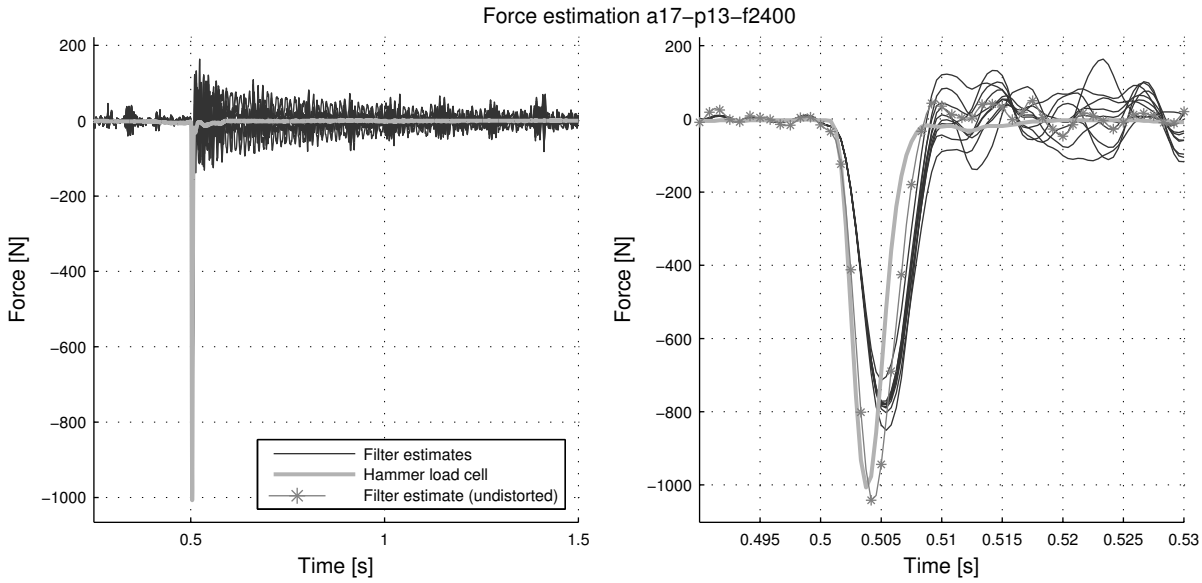

Figure 3.32: Force estimation in node 13 from 10 distorted models, compared with undistorted.

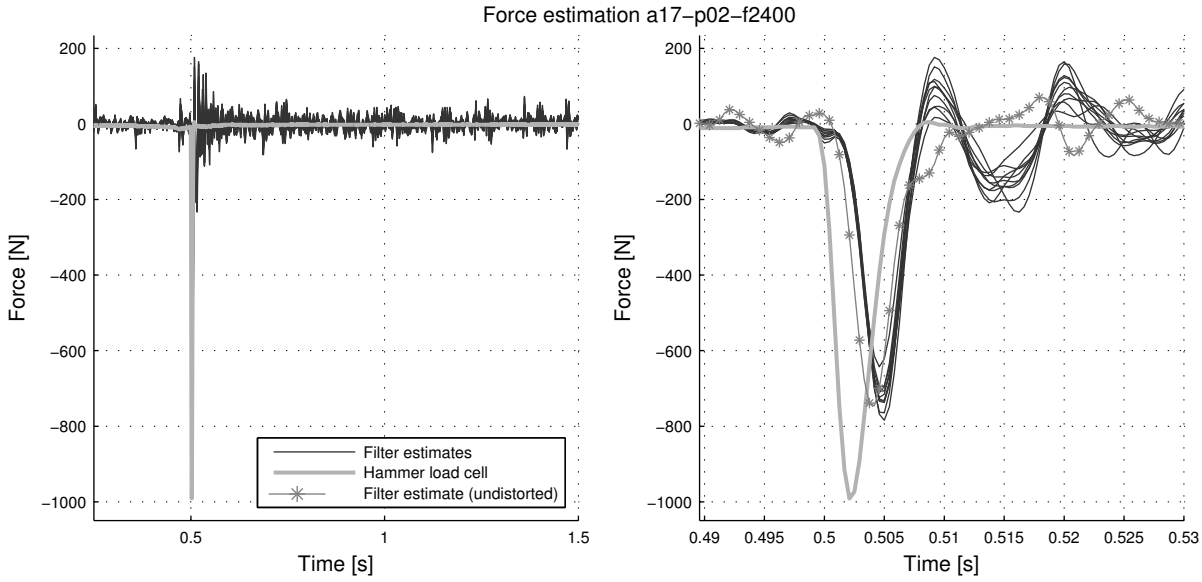

Figure 3.33: Force estimation in node 02 from 10 distorted models, compared with undistorted.

similar phenomenon for the undistorted model (preceding section) occurs for the same reason, albeit on a smaller scale. Taking into account $\boldsymbol{M}_0$ and $\boldsymbol{K}_0$ are not exact per se, referring to Table 3.4, the total model errors are effectively larger than implied just by the distortion itself. The impact force estimations can therefore be considered fairly

robust to model errors.

The displacement estimation does not suffer the same inaccuracies as forces. As pictured in Fig. 3.34, they are virtually unaffected by the inflicted model errors. This can be supported by the fact that displacements are directly linked to measurements, while unknown forces always remain indirectly coupled.

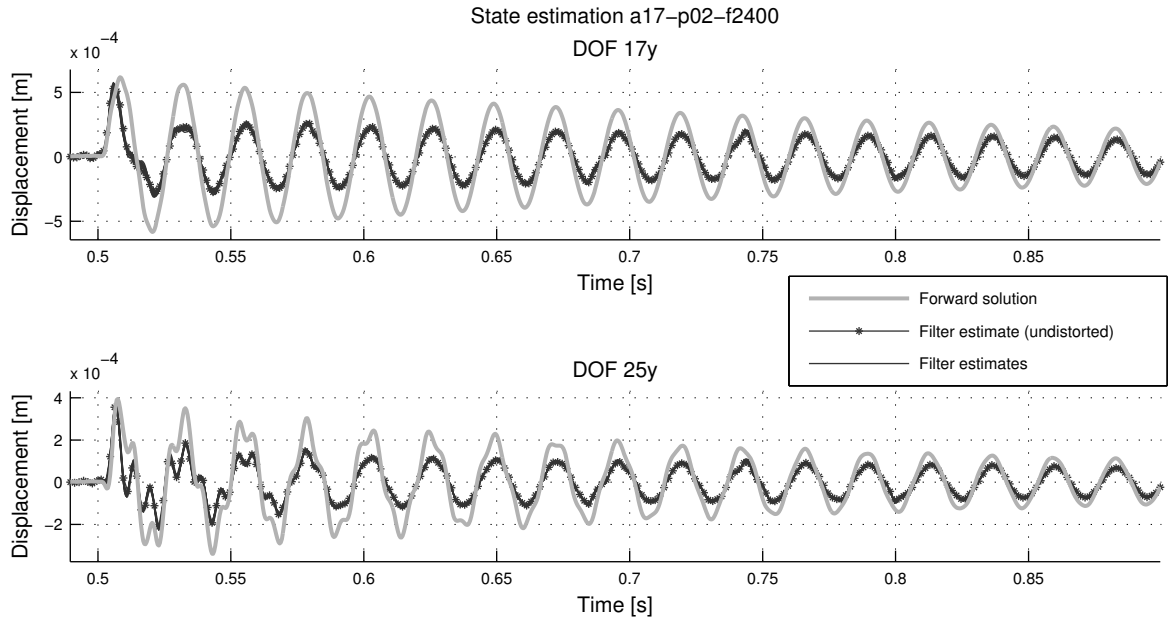

Figure 3.34: State estimation in distorted models, compared with undistorted and forward solution.

3.2.5 Force identification with reduction of observations

For practical reasons, it is often desired to limit the number of sensors on a structure to a necessary minimum. This raises the issue of finding an acceptable compromise between identification performance versus amount of observational data. As discussed in Section 2.5.2, at least one accelerometer is required for marginal stability, and additional displacement data gives asymptotic stability. Identification was performed with the setups shown in Fig. 3.35, i.e. two configurations with limited strain gauges and one with all sensors active. The filter was run with impact force located in the same nodes as

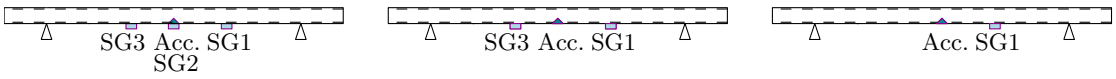

Figure 3.35: Three configurations of active sensors.

Section 3.2.3, see Fig. 3.21, but at 2400 Hz sampling only. The six force estimates is shown alongside in Fig. 3.36 – 3.41. Moderate loss of amplitude is associated with removal of strain gauges, especially collocated ones. More prominent is the force fluctuations, which for all cases increases with when less strain data is present. The force-accelerometer distance also positively correlates to greater fluctuations. An interesting result for five of the six cases is the small difference between three and two strain gauges. The main loss of accuracy comes moving from two to one strain gauges. Another phenomenon worth noting with a single strain gauge is the spurious positive initial amplitude, peaking almost simultaneous with the real impact, but incoherently with wrong sign. This result can also be connected to the large force-sensor distance, with SG1 is located in the opposite beam half, thus causing a sensor delay of a few steps. The force is strongly connected to acceleration and furthermore, as explained in Section 3.2.2, the strain measurements has poor quality. For this reason the acceleration data is the main contributor to a correct identification, thereby giving middling estimates of the impact itself without numerous strain readings. As a closing remark, some of these results must be interpreted with caution because of the strain inaccuracies. Some deceptive results can rise from removing or including flawed data. To validate the findings one must acquire better data, or alternatively generate data through a simulation.

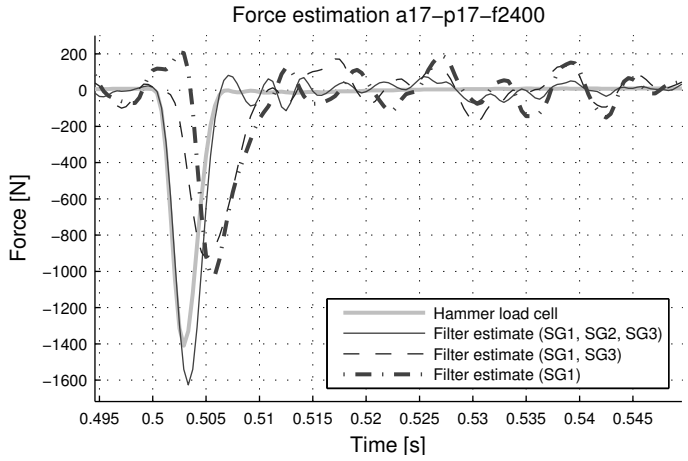

Figure 3.36: Force estimation in node 17. Collocated with accelerometer and SG2.

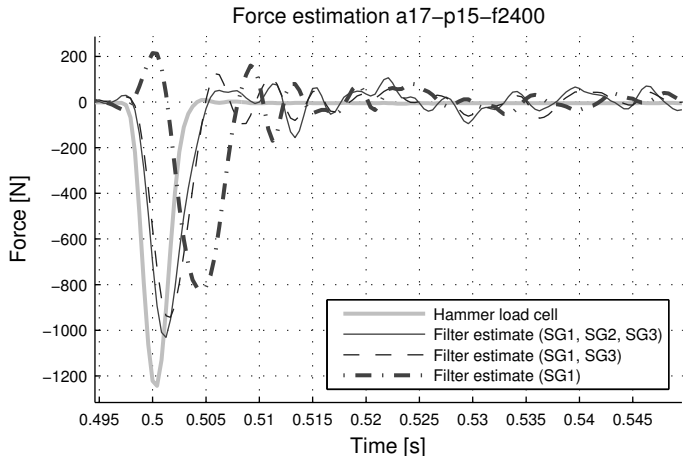

Figure 3.37: Force estimation in node 15.

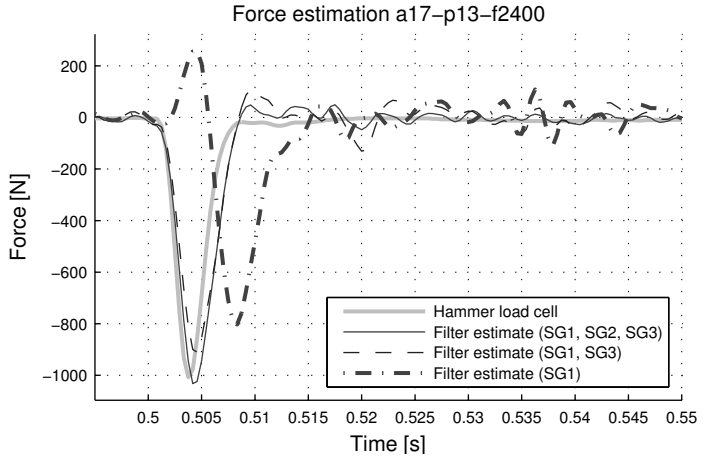

Figure 3.38: Force estimation in node 13. Collocated with SG3.

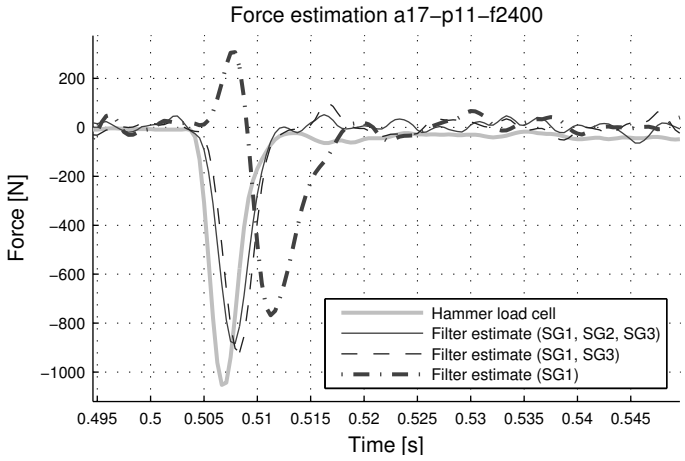

Figure 3.39: Force estimation in node 11.

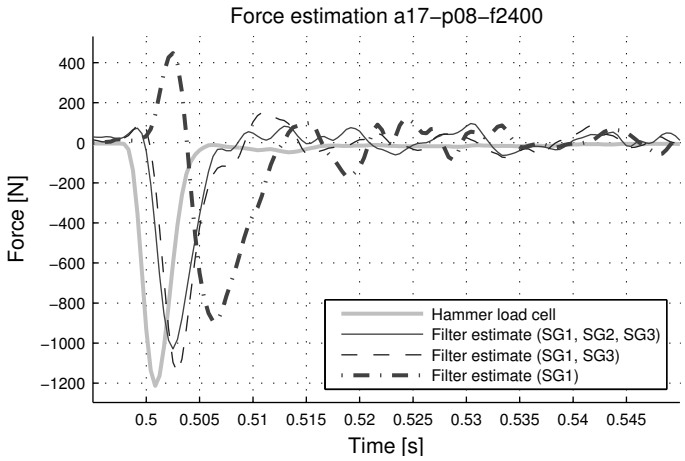

Figure 3.40: Force estimation in node 08.

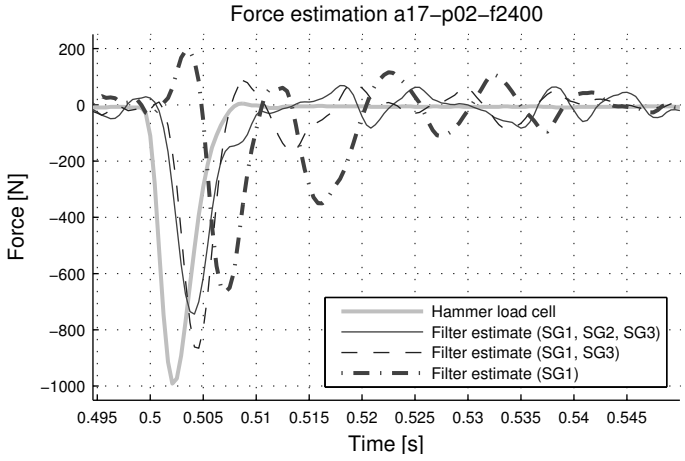

Figure 3.41: Force estimation in node 02.

3.3 Case study: simulation of Hanko channel marker

3.3.1 Model and description

The Hanko channel marker is located in the Gulf of Bothnia in shallow water (depth approximate 14 m) and is fixed to the seabed. The marker is subjected to ice actions in the winter season. A 3D visualization is shown in Fig. 3.42. The lowermost part is concrete, while the conical and supersurface tube is steel with decreasing thickness towards the top. An idealized 1200 kg mass is seated in the uppermost 2.7 m. A FE model was created by C^1-continuous beam elements. The structure was meshed into 58 elements ranging $0.3 - 0.5$ m and limited to 2D due to axisymmetry.

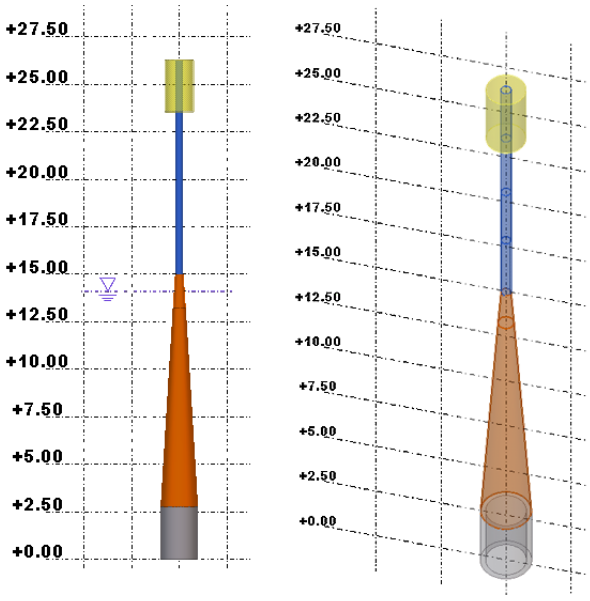

Figure 3.42: Side view and isometric transparent view of Hanko rendering. Vertical scale in meter, with origin at seabed and ice level at +14.50 m.

Boundary conditions were enforced as zero rotation and translation at seabed level. Rayleigh damping was used to generate the damping matrix. Any fluid interaction (e.g. aeroelasticity or inertia) was not included. The model mode shapes are shown in Fig. 3.43, and the corresponding natural frequencies listed in Table 3.5. f_1 matches a value attained in earlier studies [31], while the rest are slightly higher than anticipated. For ice load identification, there is a desire to determine whether an instrumentation configuration will be sufficient for analysis. The planned sensor locations are shown in

Fig. 3.44. The point in question is specifically if the tiltmeter will contribute sufficiently. The corresponding value of J (accelerometer influence) is shown in Fig. 3.45 with the ice force assumed to work in a single node. Maximum is reached with collocation at ice level, but this position is infeasible for practical reasons. The influence shows the same pattern of exponential decay as observed in Section 2.5.1.

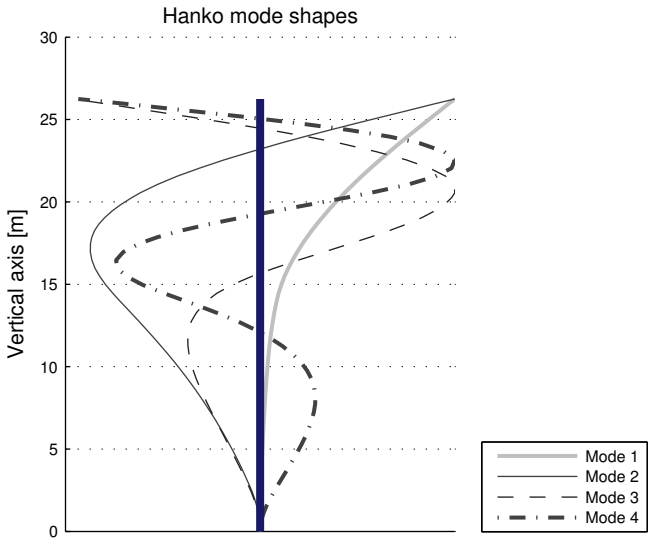

Figure 3.43: Mode shapes of FE model.

No.	FE model [Hz]
f_1	4.3
f_2	14.1
f_3	30.9
f_4	62.5

Table 3.5: Natural frequencies of FE model.

3.3.2 Force identification and response

Ice load calculation in accordance with ISO19906 [32] is done in Appendix C. The design load is a sawtooth wave with period corresponding to the first natural frequency. With no real data available, all measurements were generated from a forward solution and polluted with 5% noise. Sampling were done at 4000 Hz. The filter was supplied with unbiased initial state estimates and the asymptotic $\boldsymbol{P}_{k|k}$ (see Appendix B) in calculations to eliminate the stabilization phase of $\sim 10^2 - 10^3$ steps. Even though identification with accelerometers only is stable in the sense that all transmission zeros are $\ll 1$, a satisfactory convergence in the error (i.e. $\mathrm{tr}(\boldsymbol{P}_{k|k})$) is not attained. A tiltmeter is therefore necessary, and particularly for detection of static components. $\boldsymbol{R}$ was fixed with diagonal elements 1 for acceleration and 10^{-8} for tilt. Model noise from the distribution $\mathcal{N}(0, 10^{-14})$ was added to the forward solution, so $\boldsymbol{Q} = \boldsymbol{I} \times 10^{-14}$. Comparing the two identifications

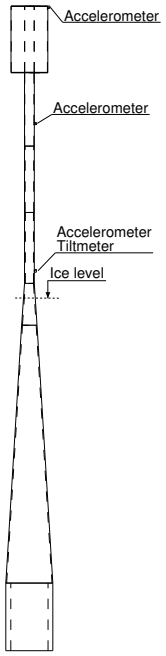

Figure 3.44: Planned location of sensors.

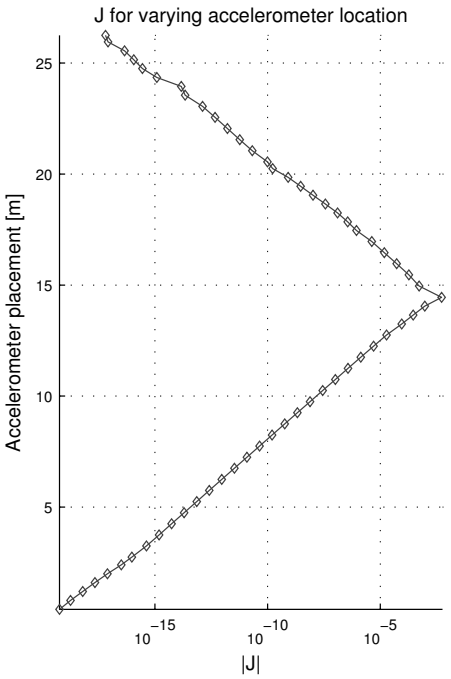

Figure 3.45: Accelerometer force influence.

with force rate levels $\boldsymbol{S} = 10^6$ and $\boldsymbol{S} = 10^8$ in Fig. 3.46 and 3.47, typical features of force regularization is displayed. In the former, the lag is very persistent and the force minimum is shifted almost half a period. The sawtooth load rate is very high ($\sim$ 1300 kN/s), and the filter struggles to keep up with abrupt changes. An increase in $\boldsymbol{S}$ to 10^8 improves this, e.g. the vertical descent in Fig. 3.47 is almost traced. As seen before, this results in a consistent increase of intermediate fluctuations since the solution is less smoothed. Ultimately, estimates do not judge the force character, but only considers statistical likeliness of data. Repeatable patterns of errors also occur, which can originate from the structural response itself, being first mode dominant. From the frequency content in Fig. 3.48, the filter estimate (for $\boldsymbol{S} = 10^8$) agrees fairly with the exact force at frequencies up to the third mode, mismatch is happens mostly above 40 Hz. This could be due to the limited number of accelerometers, mostly recognizing the 3 lowermost modes. Some challenges also arises from the fact that discontinuities in a theoretical sawtooth wave are traced by high frequency components in a Fourier series sense. The system was also observed to be highly sensitive to the level of model noise. With a decrease in model

noise the estimated force almost traced the exact solution.

The state response at ice level and top is shown in Fig. 3.49, with the accompanying spectrum in Fig. 3.50. The response at top is characterized by first and second mode excitations, while the response at ice level is more directly influenced by the force itself, and therefore has a wider force content. Larger errors in response are also found in nodes close to ice level since the effect of the force is not easy to predict. These errors displays as larger deviations in the spectrum. The movement at the top is less dominated by the force and more by time propagation of dynamics, which is easier predicted. This touches the core of the main drawback with the current force identification formulation: $\hat{\boldsymbol{p}}_{k|k-1}$ must always be taken as $\hat{\boldsymbol{p}}_{k-1|k-1}$ because no knowledge on the force propagation is provided in the formulation (i.e. $E[\boldsymbol{\eta}_k] = \mathbf{0}$). Any estimated change in the force giving $\hat{\boldsymbol{p}}_{k|k}$ therefore always relies only on measurement update. The predicted measurements ($\boldsymbol{G}_a \hat{\boldsymbol{x}}^a_{k|k-1}$) used in the measurement update step is generated under the assumption that the force remains unchanged. The erroneousness is transferred further, thereby looping the problem.

For a simple validation of the case and model, the structural velocity is inspected. The velocity amplitude at ice level can be taken as 0.4 m/s (see DOF 32y in Fig. 3.49), corresponding to an ice sheet velocity of approximately 0.3 m/s (see Appendix C). This agrees well with previous observations at the channel marker and other locations along Finnish coast [31]. The results strongly suggest identification with the presented sensor configuration is viable. The tiltmeter contributes sufficiently for a satisfactory identification to be obtainable. Since the identification is sensitive to model noise, a FE model must be designed and calibrated with attention to details. The fact that model noise is more troublesome to quantify than sensor noise does not lessen this problem. Non-structural mass must be included. Half the structure is also located subsurface, and fluid interference is not covered by the model. Fortunately the lower part is stiffer and, as displayed in the mode shapes, has smaller response.

An animation of the estimated structure response can be found as a digital attachment.

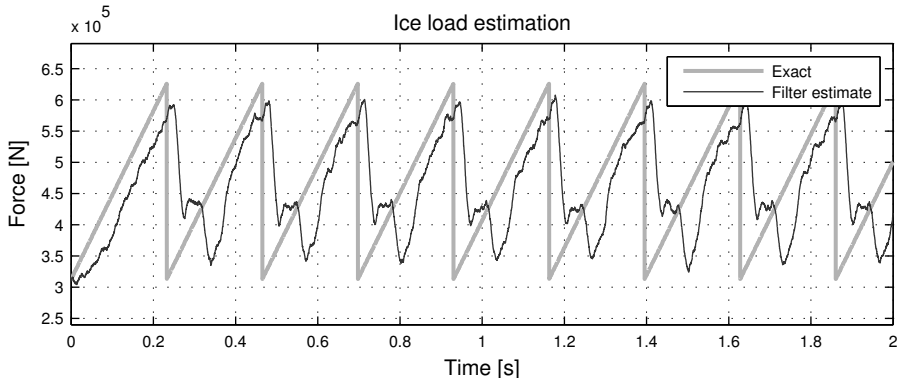

Figure 3.46: Ice force identification with $\boldsymbol{S} = 10^6$.

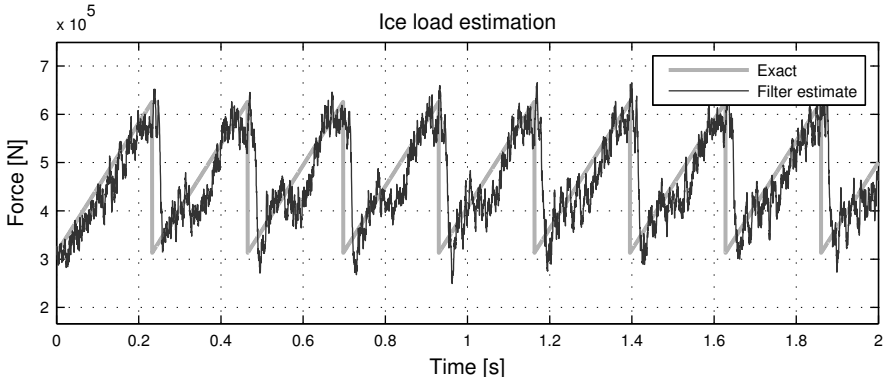

Figure 3.47: Ice force identification with $\boldsymbol{S} = 10^8$.

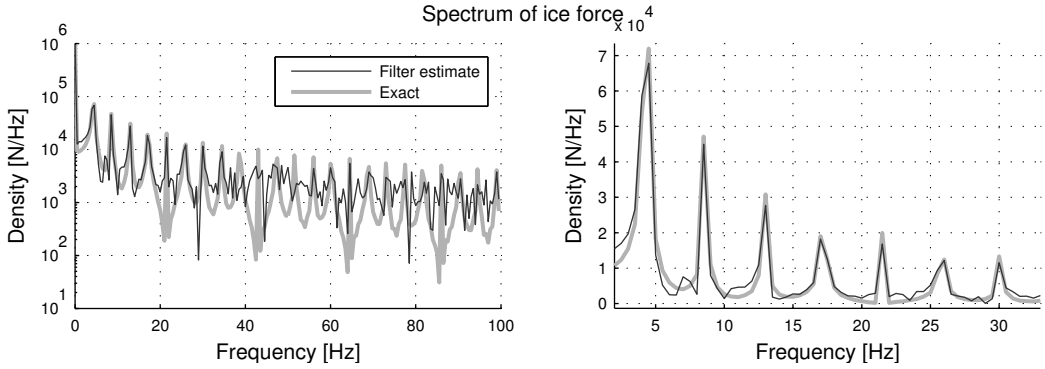

Figure 3.48: Spectrum of force filter estimate vs exact force ($\boldsymbol{S} = 10^8$). Non-logarithmic detail of low range frequencies right.

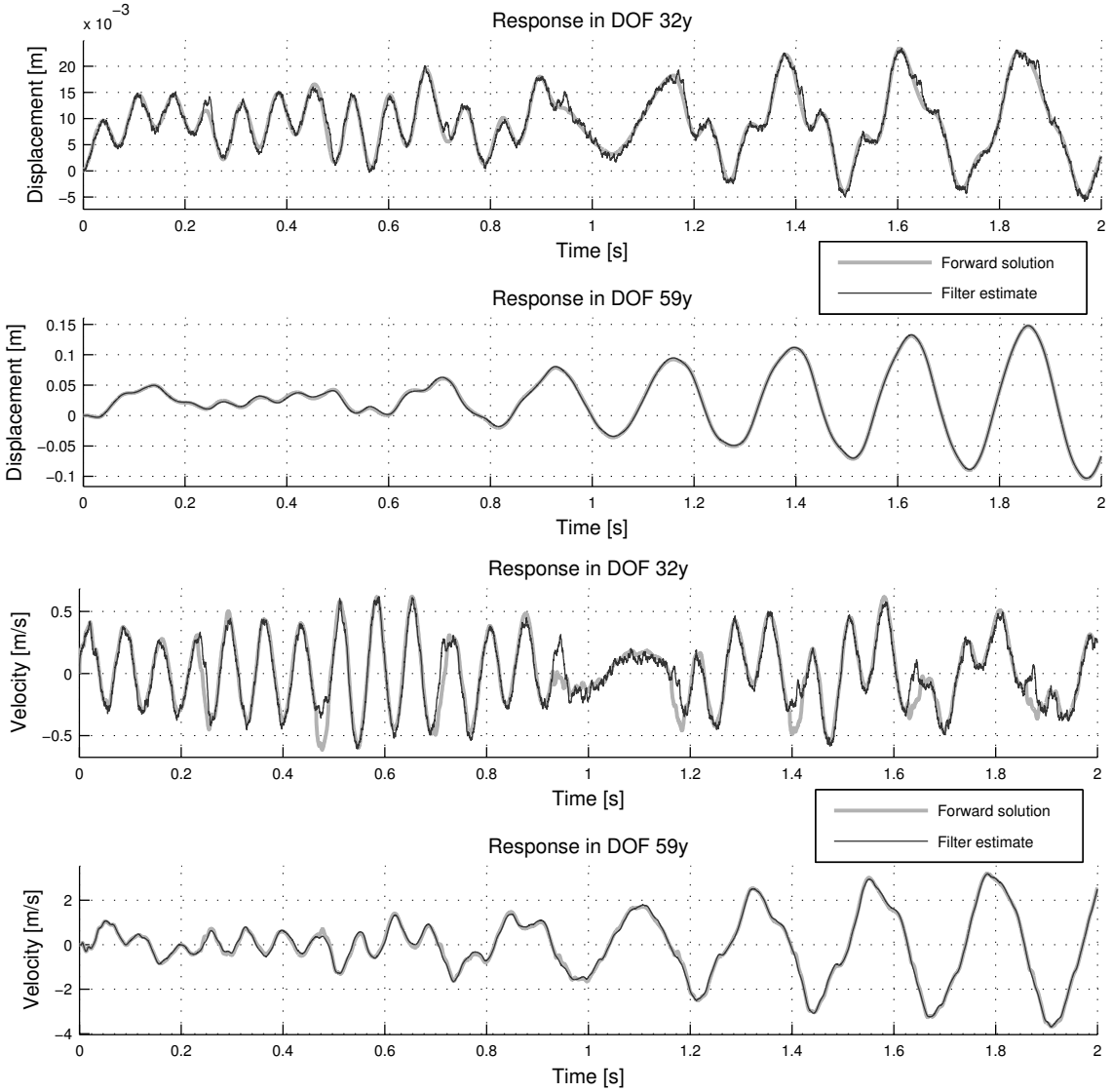

Figure 3.49: State estimation ($\boldsymbol{S} = 10^8$) at ice level (DOF 32y) and structure top (DOF 59y).

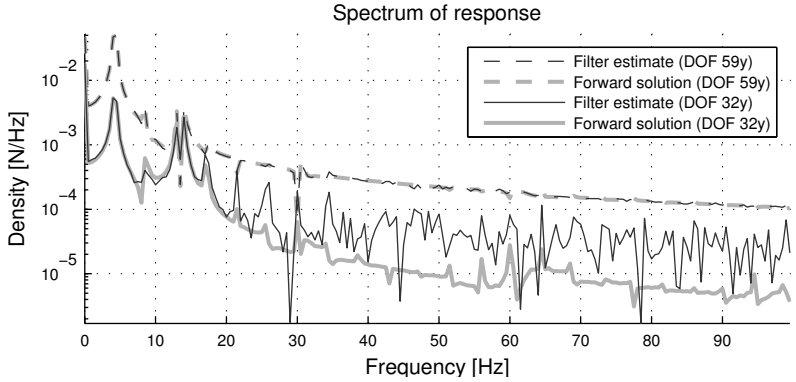

Figure 3.50: Spectrum of displacements at ice level (DOF 32y) and structure top (DOF 59y).

Chapter 4

Conclusion

4.1 Main results and research findings

This thesis on structural dynamics set out to identify loads from structural response. The main goal was to apply and validate the presented methods by numerical and laboratory experiments, and perform simulations of state and force estimation on the Hanko channel marker. The state-space representation of a linear structural dynamic system, modified to an augmented form, has been derived. Classical dynamics have been combined with stochastic considerations (noise), such that a Kalman filter can provide MVU estimates of displacements, velocities and forces. A new discrete solution to the state-space problem was presented, giving better accuracy in cases of high load rates. Requirements for system stability and observability as well as steady convergence have been elaborated upon. Moreover, force-accelerometer influence relations have been studied, in which maximum influence was found with sensor-force collocation, decreasing exponentially in non-collocation.

Laboratory tests on a simply supported beam were done with acceleration and strain measurements. Single impact forces were successfully identified and in agreement with forces measured by a load cell. The main weakness in the tests was high level correlated non-white noise in strains, from which the results suffered considerably. Tests with collocated force and accelerometer gave in general better identifications than non-collocated, confirming the theory and results obtained in prior studies. The same trend was observed

with strain gauges, where close proximity to the force improved results slightly. Furthermore, the influence of model errors was studied. The assignment found introduction of random errors in mass and stiffness to decrease the impact identification moderately, besides create spurious force fluctuations. Estimation of displacements and velocities was more robust and virtually unaffected by a faulty model. Lastly, identification was attempted with only two or one strain gauges in addition to the accelerometer. Although these configurations had stable system reconstructability, the results were severely affected. The main outcome on force identification were loss of impact amplitude, increased time lag and spurious fluctuations. This was particularly the case with one strain gauge only. The role of the high strain noise in these cases remains unclear.

Numerical simulations on the Hanko channel marker, instrumented with three accelerometers and a tiltmeter, has demonstrated the feasibility of ice force identification. Moderate errors were found in identification of a sawtooth wave load. The estimated response agreed well with a forward solution. Simulations were performed on a 2D model, but the problem formulation suggests a 3D model will yield results of similar character. The analysis results emphasized the necessity of an accurate FE model to absolutely limit model errors in order to obtain identifications with satisfactory precision.

The applied methods perform in general satisfactory if used with care, yet some drawbacks have been noted. It is now possible to state the force identification consistently suffers from the lack of sufficient prediction. This originates from the precept of the force as a Gaussian random walk with zero mean. Specification of a cumbersome force rate parameter $\boldsymbol{S}$ is required, controlling the force smoothness. This consequently indirectly imposes a behavior which can be undesired or does not fit the true nature of the force. Any assumptions on the force are problematic to justify since the force is, by problem definition, unknown. This is the most severe shortcoming of the method, and a complete reformulation on this point would certainly improve results.

4.2 Remarks and recommendations for future research

In the experimental tests on the simply supported beam the time domain was roughly separated into a short force application phase (with little response) and a free vibrations phase (with zero force). Since the filter estimates jointly response and load, it would be interesting to see an experiment with long duration force identification, where the both force and response are nonzero for prolonged periods. This requires load cells with ability of registering non-instantaneous loads, alternatively utilizing e.g. a rotational device whose inertia force can be calculated.

Controllable laboratory tests are in general helpful to validate ideas before being applied to real structures. The laboratory research in this assignment did not include systems of intricate nature. A further step could be modification by introducing a geometric stiffness, analogous to cable-stayed bridges. If a geometric stiffness matrix is included in the model, would this suffice? Future work also needs to assess the effect of FE meshing on the estimation results and the force-accelerometer influence.

It should also be mentioned the joint input-state estimator referred to in Section 2.6 estimates the force purely from measurements, thereby possibly avoiding the problematic force assumptions stumbled upon here. A final remark concerns ideas emerged during studies of the algorithm, and especially remedies for the weak point of force prediction. As an expansion on the first order hold solution of the state-space equation, one could rewrite Eq. (2.2.14) and (2.2.15) to:

$$\begin{bmatrix} \boldsymbol{x}_{k+1} \\ \boldsymbol{y}_k \end{bmatrix} = \begin{bmatrix} \boldsymbol{A} & \widetilde{\boldsymbol{B}} \\ \boldsymbol{G} & \widetilde{\boldsymbol{J}} \end{bmatrix} \begin{bmatrix} \boldsymbol{x}_k \\ \widetilde{\boldsymbol{p}}_k \end{bmatrix} + \begin{bmatrix} \boldsymbol{w}_k \\ \boldsymbol{v}_k \end{bmatrix}$$

where

$$\widetilde{\boldsymbol{p}}_k = \begin{bmatrix} \boldsymbol{p}_k \\ \boldsymbol{p}_{k+1} \end{bmatrix} \qquad \widetilde{\boldsymbol{B}} = \begin{bmatrix} \boldsymbol{B} - \boldsymbol{F}/\Delta t & \boldsymbol{F}/\Delta t \end{bmatrix} \qquad \widetilde{\boldsymbol{J}} = \begin{bmatrix} \boldsymbol{J} & \boldsymbol{0} \end{bmatrix}$$

such that

$$\widetilde{\boldsymbol{x}}^a_{k+1} = \begin{bmatrix} \boldsymbol{x}_{k+1} \\ \widetilde{\boldsymbol{p}}_{k+1} \end{bmatrix} = \widetilde{\boldsymbol{A}}_a \widetilde{\boldsymbol{x}}^a_k + \begin{bmatrix} \boldsymbol{w}_k \\ \boldsymbol{\Psi}_k \end{bmatrix} \qquad \boldsymbol{y}_k = \widetilde{\boldsymbol{G}}_a \widetilde{\boldsymbol{x}}^a_k + \boldsymbol{v}_k$$

where

$$\widetilde{\boldsymbol{A}}_a = \begin{bmatrix} \boldsymbol{A} & \widetilde{\boldsymbol{B}} \\ \boldsymbol{0} & \boldsymbol{I} \end{bmatrix} \qquad \widetilde{\boldsymbol{G}}_a = \begin{bmatrix} \boldsymbol{G} & \widetilde{\boldsymbol{J}} \end{bmatrix} \qquad \widetilde{\boldsymbol{p}}_{k+1} = \widetilde{\boldsymbol{p}}_k + \boldsymbol{\Psi}_k$$

in other words a Kalman filter doubly augmented with force components. Supplying all necessary matrices, could one perform an identification on the new augmented state vector $\widetilde{\boldsymbol{x}}^a_k$? Notably, this also involves an one step prediction of the force, giving two estimates for a single time step. How would the prediction and filter estimate differ? One can recognize the generality of the stability criteria in Section 2.5.2 still holds, but with $\boldsymbol{B}$ and $\boldsymbol{J}$ modified to $\widetilde{\boldsymbol{B}}$ and $\widetilde{\boldsymbol{J}}$. Can this type of formulation change the transmission zero stability criteria? As a remark, this was tested at the beam in Section 3.2 with accelerometer data only, interestingly adjusting the largest transmission zero from $1 - 10^3$ to $10^{-7} - 10^{-6}$. Does this imply the system is unstable transformed into a stable one, or does one meet other hinders later? Sadly, $\boldsymbol{A}$ and $\boldsymbol{G}$ remain unchanged, thereby not affecting observability. Furthermore, the new force vector has dimension $2 \times n_p$, requiring a double amount of sensors. Time limitations left this further investigated.

Bibliography

[1] S. L. Han and T. Kinoshita. Investigation of a stochastic inverse method to estimate an external force: Applications to a wave-structure interaction. *Mathematical Problems in Engineering*, 2012, 2012.

[2] S. Granger and L. Perotin. An inverse method for the identification of a distributed random excitation acting on a vibrating structure part 1: theory. *Mechanical Systems and Signal Processing*, 13(1):53–65, 1999.

[3] H. Imai, C. Yun, O. Maruyama, and M. Shinozuka. Fundamentals of system identification in structural dynamics. *Probabilistic Engineering Mechanics*, 4(4):162–173, 1989.

[4] C. Johnson. Identification of unknown, time-varying forces/moments in dynamics and vibration problems using a new approach to deconvolution. *Shock and Vibration*, 5(3):181–197, 1998.

[5] Y. Liu and W. S. Shepard Jr. Dynamic force identification based on enhanced least squares and total least-squares schemes in the frequency domain. *Journal of sound and vibration*, 282(1):37–60, 2005.

[6] E.-M. Lourens. *Force identification in structural dynamics*. PhD thesis, Katholieke Universiteit Leuven - Faculty of Engineering, Leuven (Belgium), 2012.

[7] R. L. Williams II and D. A. Lawrence. *Linear state-space control systems*. John Wiley and Sons, New Jersey, USA, 1st edition, 2007.

[8] C. Heij, A. Ran, and F. van Schagen. *Introduction to mathematical systems theory:*

linear systems, identification and control. Birkhäuser, Basel, Switzerland, 1st edition, 2007.

[9] W. S. Levine. *Control System Advanced Methods*. CRC Press, Maryland, USA, 2nd edition, 2010.

[10] M. S. Grewal and A. P. Andrews. *Kalman filtering: theory and practice using MATLAB*. John Wiley and Sons, New Jersey, USA, 3rd edition, 2008.

[11] C. K. Ma, J. M. Chang, and D. C. Lin. Input forces estimation of beam structures by an inverse method. *Journal of sound and vibration*, 259(2):387–407, 2003.

[12] B. D. O. Anderson and J. B. Moore. *Optimal filtering*. Prentice-Hall, New Jersey, USA, 1979.

[13] R. E. Kalman. A new approach to linear filtering and prediction problems. *Journal of basic Engineering*, 82(1):35–45, 1960.

[14] F. D. M. Neto and A. J. da Silva Neto. *An Introduction to Inverse Problems with Applications*. Springer, 2013.

[15] Y. Chan, A. G. Hu, and J. Plant. A Kalman filter based tracking scheme with input estimation. *Aerospace and Electronic Systems, IEEE Transactions on*, AES-15(2): 237–244, 1979.

[16] F. L. Lewis, L. Xie, and D. Popa. *Optimal and robust estimation: with an introduction to stochastic control theory*. Taylor & Francis Group, Florida, USA, 2nd edition, 2007.

[17] A. Charnes, E. L. Frome, and P.-L. Yu. On the equivalence of generalized least-squares approaches to the evaluation of measurement comparisons. *Journal of the American Statistical Association*, 71(353):169–171, 1976.

[18] S. Säarkkä. *Bayesian Filtering and Smoothing*, volume 3. Cambridge University Press, 2013.

[19] K. Maes, E.-M. Lourens, G. De Roeck, and G. Lombaert. General conditions for instantaneous system inversion in structural dynamics. In *Proceedings of the 5th International Conference on Structural Engineering, Mechanics and Computation, SEMC 2013*, pages 43–48, 2013.

[20] M. Bjerkås. *Ice actions on offshore structures - with applications of continuous wavelet transforms on ice load signals*. PhD thesis, Norwegian University of Science and Technology, 2006.

[21] S. Gillijns. *Kalman Filtering Techniques for System Inversion and Data Assimilation*. PhD thesis, Katholieke Universiteit Leuven - Faculty of Engineering Technology, Leuven (Belgium), 2007.

[22] C.-K. Ma, P.-C. Tuan, D.-C. Lin, and C.-S. Liu. A study of an inverse method for the estimation of impulsive loads. *International Journal of Systems Science*, 29(6): 663–672, 1998.

[23] C.-K. Ma and D.-C. Lin. Input forces estimation of a cantilever beam. *Inverse Problems in Engineering*, 8(6):511–528, 2000.

[24] J. Hwang, A. Kareem, and W. Kim. Estimation of modal loads using structural response. *Journal of Sound and Vibration*, 326(3):522–539, 2009.

[25] P. Hollandsworth and H. Busby. Impact force identification using the general inverse technique. *International Journal of Impact Engineering*, 8(4):315–322, 1989.

[26] G. Lombaert, K. Maes, and E.-M. Lourens. CISM advanced course: Identification methods for structural health monitoring and residual lifecycle assessment: Vibration-based force and state estimation for structures. Lecture presentation, 6. June 2013. Udine, Italy.

[27] K. Bell. *An engineering approach to finite element analysis of linear structural mechanics problems*. Akademika Publ., Trondheim, 1st edition, 2013.

[28] T. Nord, E.-M. Lourens, O. Øiseth, and A. Metrikine. Model-based force identification in experimental ice-structure interaction by means of Kalman filtering. In *EURODYN, Porto, Portugal*, 2014 (to be published).

[29] A. K. Chopra. *Dynamics of Structures: Theory and Applications to Earthquake Engineering*. Civil Engineering and Engineering Mechanics Series. Prentice Hall/Pearson Education, 3rd edition, 2011.

[30] S. Adhikari. Response variability of linear stochastic systems: A general solution using random matrix theory. In *49th AIAA/ASME/ASCE/AHS/ASC Structures, Structural Dynamics, and Materials Conference*, 2008.

[31] M. Määttänen. Ice velocity limit to frequency lock-in vibrations. In *19th IAHR International Symposium on Ice*, volume 2, pages 1265–1276, 2008.

[32] ISO. *ISO/FDIS 19906:2010, Petroleum and natural gas industries - Arctic offshore structures*, 2010.

Appendices

Appendix A

State-space ODE solution assuming input first order hold

The load $\boldsymbol{p}$ is assumed to vary linearly in the time interval $t_k < \tau < t_{k+1}$. Interval length is fixed to $t_{k+1} - t_k = \Delta t$. Some notations are adopted from Lourens[1]. Useful properties:

$$e^{\boldsymbol{Z}t} \equiv \sum_{k=0}^{\infty} \frac{(\boldsymbol{Z}t)^k}{k!} \tag{A.0.1}$$

$$e^{\pm\boldsymbol{Z}t}\boldsymbol{Z} = \left[\sum_{k=0}^{\infty} \frac{(\pm\boldsymbol{Z}t)^k}{k!}\right]\boldsymbol{Z} = \sum_{k=0}^{\infty} \frac{(\pm 1)^k(\boldsymbol{Z})^{k+1}t^k}{k!} = \boldsymbol{Z}\left[\sum_{k=0}^{\infty} \frac{(\pm\boldsymbol{Z}t)^k}{k!}\right] = \boldsymbol{Z}e^{\pm\boldsymbol{Z}t} \tag{A.0.2}$$

$$\begin{aligned} \boldsymbol{Z}^{-1}e^{\pm\boldsymbol{Z}t}\boldsymbol{Z} &= \boldsymbol{Z}^{-1}\boldsymbol{Z}e^{\pm\boldsymbol{Z}t} = e^{\pm\boldsymbol{Z}t} \\ \boldsymbol{Z}^{-1}e^{\pm\boldsymbol{Z}t} &= e^{\pm\boldsymbol{Z}t}\boldsymbol{Z}^{-1} \end{aligned} \tag{A.0.3}$$

$$\frac{d(e^{\boldsymbol{Z}t})}{dt} = \boldsymbol{Z}e^{\boldsymbol{Z}t} \tag{A.0.4}$$

$$\int e^{\boldsymbol{Z}t}dt = \boldsymbol{Z}^{-1}e^{\boldsymbol{Z}t} + \boldsymbol{C}_0 \tag{A.0.5}$$

[1] E.-M. Lourens. *Force identification in structural dynamics.* PhD thesis, Katholieke Universiteit Leuven - Faculty of Engineering, Leuven (Belgium), 2012.

State-space equation on continuous form and solution by integrating factor:

$$
\begin{aligned}
\dot{\boldsymbol{x}} - \boldsymbol{A}_c\boldsymbol{x} &= \boldsymbol{B}_c\boldsymbol{p} \\
e^{-\boldsymbol{A}_c t}[\dot{\boldsymbol{x}} - \boldsymbol{A}_c\boldsymbol{x}] &= e^{-\boldsymbol{A}_c t}\boldsymbol{B}_c\boldsymbol{p} \\
\frac{d(e^{-\boldsymbol{A}_c t}\boldsymbol{x})}{dt} &= e^{-\boldsymbol{A}_c t}\boldsymbol{B}_c\boldsymbol{p} \\
\int_{(\boldsymbol{x}_k,t_k)}^{(\boldsymbol{x}_{k+1},t_{k+1})} d(e^{-\boldsymbol{A}_c t}\boldsymbol{x}) &= \int_{t_k}^{t_{k+1}} e^{-\boldsymbol{A}_c\tau}\boldsymbol{B}_c\boldsymbol{p} \quad d\tau \\
&= \int_{t_k}^{t_{k+1}} e^{-\boldsymbol{A}_c\tau}\boldsymbol{B}_c[\boldsymbol{p}_k + \frac{\tau - t_k}{\Delta t}(\boldsymbol{p}_{k+1} - \boldsymbol{p}_k)] \quad d\tau \\
&= \int_{t_k}^{t_{k+1}} e^{-\boldsymbol{A}_c\tau} \quad d\tau\, \boldsymbol{B}_c\boldsymbol{p}_k \\
&+ \int_{t_k}^{t_{k+1}} e^{-\boldsymbol{A}_c\tau}\frac{\tau - t_k}{\Delta t} \quad d\tau\, \boldsymbol{B}_c(\boldsymbol{p}_{k+1} - \boldsymbol{p}_k)
\end{aligned}
\tag{A.0.6}
$$

First integral, right side of Eq. (A.0.6):

$$
\begin{aligned}
&\int_{t_k}^{t_{k+1}} e^{-\boldsymbol{A}_c\tau} \quad d\tau \\
&= -\boldsymbol{A}_c^{-1}[e^{-\boldsymbol{A}_c\tau}]_{t_k}^{t_{k+1}} \\
&= -\boldsymbol{A}_c^{-1}[e^{-\boldsymbol{A}_c(t_k+\Delta t)} - e^{-\boldsymbol{A}_c t_k}] \\
&= -\boldsymbol{A}_c^{-1}e^{-\boldsymbol{A}_c t_k}[e^{-\boldsymbol{A}_c\Delta t} - \boldsymbol{I}]
\end{aligned}
\tag{A.0.7}
$$

Second integral, right side of Eq. (A.0.6):

$$
\begin{aligned}
&\int_{t_k}^{t_{k+1}} e^{-\boldsymbol{A}_c\tau}\frac{\tau - t_k}{\Delta t} \quad d\tau \\
=&\frac{1}{\Delta t}\left[-\int_{t_k}^{t_{k+1}} e^{-\boldsymbol{A}_c\tau}\boldsymbol{A}_c^{-1} \quad d\tau - [e^{-\boldsymbol{A}_c\tau}(\tau - t_k)\boldsymbol{A}_c^{-1}]_{t_k}^{t_{k+1}}\right] \\
=&\frac{-1}{\Delta t}[e^{-\boldsymbol{A}_c\tau}(\tau - t_k)\boldsymbol{A}_c^{-1} + e^{-\boldsymbol{A}_c\tau}\boldsymbol{A}_c^{-1}\boldsymbol{A}_c^{-1}]_{t_k}^{t_{k+1}} \\
=&\frac{-1}{\Delta t}e^{-\boldsymbol{A}_c t_k}[e^{-\boldsymbol{A}_c\Delta t}(\Delta t\boldsymbol{A}_c^{-1} + \boldsymbol{A}_c^{-1}\boldsymbol{A}_c^{-1}) - \boldsymbol{A}_c^{-1}\boldsymbol{A}_c^{-1}] \\
=&\frac{-1}{\Delta t}e^{-\boldsymbol{A}_c t_k}[\Delta t e^{-\boldsymbol{A}_c\Delta t}\boldsymbol{A}_c^{-1} + (e^{-\boldsymbol{A}_c\Delta t} - \boldsymbol{I})\boldsymbol{A}_c^{-1}\boldsymbol{A}_c^{-1}]
\end{aligned}
\tag{A.0.8}
$$

Integral left side of Eq. (A.0.6):

$$\begin{aligned}
&\int_{(\boldsymbol{x}_k,t_k)}^{(\boldsymbol{x}_{k+1},t_{k+1})} d(e^{-\boldsymbol{A}_c t}\boldsymbol{x}) \\
=&[e^{-\boldsymbol{A}_c t}\boldsymbol{x}]_{(\boldsymbol{x}_k,t_k)}^{(\boldsymbol{x}_{k+1},t_{k+1})} \\
=&e^{-\boldsymbol{A}_c t_{k+1}}\boldsymbol{x}_{k+1} - e^{-\boldsymbol{A}_c t_k}\boldsymbol{x}_k \\
=&e^{-\boldsymbol{A}_c t_k}[e^{-\boldsymbol{A}_c \Delta t}\boldsymbol{x}_{k+1} - \boldsymbol{x}_k]
\end{aligned} \tag{A.0.9}$$

All integrals in Eq. (A.0.6) assembled, forming a discretization:

$$\begin{aligned}
e^{-\boldsymbol{A}_c t_k}[e^{-\boldsymbol{A}_c \Delta t}\boldsymbol{x}_{k+1} - \boldsymbol{x}_k] &= -e^{-\boldsymbol{A}_c t_k}\boldsymbol{A}_c^{-1}[e^{-\boldsymbol{A}_c \Delta t} - \boldsymbol{I}]\boldsymbol{B}_c\boldsymbol{p}_k \\
&+ \frac{-e^{-\boldsymbol{A}_c t_k}}{\Delta t}[\Delta t e^{-\boldsymbol{A}_c \Delta t}\boldsymbol{A}_c^{-1} + (e^{-\boldsymbol{A}_c \Delta t} - \boldsymbol{I})\boldsymbol{A}_c^{-1}\boldsymbol{A}_c^{-1}]\boldsymbol{B}_c(\boldsymbol{p}_{k+1} - \boldsymbol{p}_k) \\
e^{-\boldsymbol{A}_c \Delta t}\boldsymbol{x}_{k+1} - \boldsymbol{x}_k &= -\boldsymbol{A}_c^{-1}[e^{-\boldsymbol{A}_c \Delta t} - \boldsymbol{I}]\boldsymbol{B}_c\boldsymbol{p}_k \\
&+ \frac{-1}{\Delta t}[\Delta t e^{-\boldsymbol{A}_c \Delta t}\boldsymbol{A}_c^{-1} + (e^{-\boldsymbol{A}_c \Delta t} - \boldsymbol{I})\boldsymbol{A}_c^{-1}\boldsymbol{A}_c^{-1}]\boldsymbol{B}_c(\boldsymbol{p}_{k+1} - \boldsymbol{p}_k) \\
\boldsymbol{x}_{k+1} &= e^{\boldsymbol{A}_c \Delta t}\boldsymbol{x}_k - \boldsymbol{A}_c^{-1}e^{\boldsymbol{A}_c \Delta t}[e^{-\boldsymbol{A}_c \Delta t} - \boldsymbol{I}]\boldsymbol{B}_c\boldsymbol{p}_k \\
&+ \frac{e^{\boldsymbol{A}_c \Delta t}}{\Delta t}[\Delta t e^{-\boldsymbol{A}_c \Delta t}\boldsymbol{A}_c^{-1} + (e^{-\boldsymbol{A}_c \Delta t} - \boldsymbol{I})\boldsymbol{A}_c^{-1}\boldsymbol{A}_c^{-1}]\boldsymbol{B}_c(\boldsymbol{p}_{k+1} - \boldsymbol{p}_k)
\end{aligned}$$

$$\begin{aligned}
&= e^{\boldsymbol{A}_c \Delta t}\boldsymbol{x}_k - \boldsymbol{A}_c^{-1}[\boldsymbol{I} - e^{\boldsymbol{A}_c \Delta t}]\boldsymbol{B}_c\boldsymbol{p}_k \\
&+ \frac{-1}{\Delta t}[\Delta t\boldsymbol{A}_c^{-1} + (\boldsymbol{I} - e^{\boldsymbol{A}_c \Delta t})\boldsymbol{A}_c^{-1}\boldsymbol{A}_c^{-1}]\boldsymbol{B}_c(\boldsymbol{p}_{k+1} - \boldsymbol{p}_k)
\end{aligned}$$

$$\begin{aligned}
&= e^{\boldsymbol{A}_c \Delta t}\boldsymbol{x}_k + [e^{\boldsymbol{A}_c \Delta t} - \boldsymbol{I}]\boldsymbol{A}_c^{-1}\boldsymbol{B}_c\boldsymbol{p}_k \\
&+ \boldsymbol{A}_c^{-1}[-\Delta t\boldsymbol{B}_c + (e^{\boldsymbol{A}_c \Delta t} - \boldsymbol{I})\boldsymbol{A}_c^{-1}\boldsymbol{B}_c]\frac{(\boldsymbol{p}_{k+1} - \boldsymbol{p}_k)}{\Delta t}
\end{aligned} \tag{A.0.10}$$

Final result:

$$\boldsymbol{x}_{k+1} = \boldsymbol{A}\boldsymbol{x}_k + \boldsymbol{B}\boldsymbol{p}_k + \boldsymbol{F}\frac{(\boldsymbol{p}_{k+1} - \boldsymbol{p}_k)}{\Delta t} \tag{A.0.11}$$

$$\boldsymbol{A} = e^{\boldsymbol{A}_c \Delta t} \quad , \quad \boldsymbol{B} = (\boldsymbol{A} - \boldsymbol{I})\boldsymbol{A}_c^{-1}\boldsymbol{B}_c \quad , \quad \boldsymbol{F} = \boldsymbol{A}_c^{-1}(\boldsymbol{B} - \boldsymbol{B}_c\Delta t) \tag{A.0.12}$$

Appendix B

Kalman filter steady state covariance and augmented system detectability

Covariance matrices $\boldsymbol{R}$ and $\boldsymbol{Q}_a$ are taken as time-invariant. The assumed asymptotic conditions are no change in covariance matrices over time steps, i.e. $\boldsymbol{P}_{k|k-1} \equiv \boldsymbol{P}_{k+1|k}$ and $\boldsymbol{P}_{k|k} \equiv \boldsymbol{P}_{k+1|k+1}$.

Covariance time update:

$$\begin{aligned} \boldsymbol{P}_{k+1|k} &= \boldsymbol{A}_a \boldsymbol{P}_{k|k} \boldsymbol{A}_a^T + \boldsymbol{Q}_a \\ \boldsymbol{P}_{k|k} &= \boldsymbol{A}_a^{-1} (\boldsymbol{P}_{k+1|k} - \boldsymbol{Q}_a) \boldsymbol{A}_a^{-T} \\ \boldsymbol{P}_{k|k} &= \boldsymbol{A}_a^{-1} (\boldsymbol{P}_{k|k-1} - \boldsymbol{Q}_a) \boldsymbol{A}_a^{-T} \end{aligned} \tag{B.0.1}$$

Covariance measurement update:

$$\boldsymbol{P}_{k|k} = (\boldsymbol{I} - \boldsymbol{L}_k \boldsymbol{G}_a) \boldsymbol{P}_{k|k-1} \tag{B.0.2}$$

Kalman gain:

$$\boldsymbol{L}_k = \boldsymbol{P}_{k|k-1} \boldsymbol{G}_a^T [\boldsymbol{G}_a \boldsymbol{P}_{k|k-1} \boldsymbol{G}_a^T + \boldsymbol{R}]^{-1} \tag{B.0.3}$$

Setting Eq. (B.0.1) and (B.0.2) equal, inserting Eq. (B.0.3):

$$\begin{aligned}
\boldsymbol{A}_a^{-1}(\boldsymbol{P}_{k|k-1} - \boldsymbol{Q}_a)\boldsymbol{A}_a^{-T} &= (\boldsymbol{I} - \boldsymbol{P}_{k|k-1}\boldsymbol{G}_a^T[\boldsymbol{G}_a\boldsymbol{P}_{k|k-1}\boldsymbol{G}_a^T + \boldsymbol{R}]^{-1}\boldsymbol{G}_a)\boldsymbol{P}_{k|k-1} \\
\boldsymbol{P}_{k|k-1} - \boldsymbol{Q}_a &= \boldsymbol{A}_a(\boldsymbol{I} - \boldsymbol{P}_{k|k-1}\boldsymbol{G}_a^T[\boldsymbol{G}_a\boldsymbol{P}_{k|k-1}\boldsymbol{G}_a^T + \boldsymbol{R}]^{-1}\boldsymbol{G}_a)\boldsymbol{P}_{k|k-1}\boldsymbol{A}_a^T \\
\boldsymbol{P}_{k|k-1} - \boldsymbol{Q}_a &= \boldsymbol{A}_a\boldsymbol{P}_{k|k-1}\boldsymbol{A}_a^T - \boldsymbol{A}_a\boldsymbol{P}_{k|k-1}\boldsymbol{G}_a^T[\boldsymbol{G}_a\boldsymbol{P}_{k|k-1}\boldsymbol{G}_a^T + \boldsymbol{R}]^{-1}\boldsymbol{G}_a\boldsymbol{P}_{k|k-1}\boldsymbol{A}_a^T
\end{aligned} \tag{B.0.4}$$

Arriving at the final result, the discrete-time algebraic Riccati equation (DARE):

$$\boldsymbol{0} = \boldsymbol{Q}_a - \boldsymbol{P}_{k|k-1} + \boldsymbol{A}_a\boldsymbol{P}_{k|k-1}\boldsymbol{A}_a^T - \boldsymbol{A}_a\boldsymbol{P}_{k|k-1}\boldsymbol{G}_a^T[\boldsymbol{G}_a\boldsymbol{P}_{k|k-1}\boldsymbol{G}_a^T + \boldsymbol{R}]^{-1}\boldsymbol{G}_a\boldsymbol{P}_{k|k-1}\boldsymbol{A}_a^T \tag{B.0.5}$$

which can be solved in MATLAB by the syntax

$$[P_p, Z_1, Z_2] = \text{dare}(A_a^T, G_a^T, Q_a, R)$$

where P_p contains the steady state values of the covariance matrix $\boldsymbol{P}_{k|k-1}$. The asymptotic $\boldsymbol{P}_{k|k}$ (and the converging value of $\text{tr}(\boldsymbol{P}_{k|k})$) can preferably be found from Eq. (B.0.2), alternatively by Eq. (B.0.1) but avoiding explicit inversion, as this commonly shows to give large numerical errors. The steady Kalman gain is given from Eq. (B.0.3).

The existence of a DARE solution requires the augmented pair $(\boldsymbol{A}_a, \boldsymbol{G}_a)$ to be detectable. This can be validated by the Popov-Belevitch-Hautus (PBH) rank test [1]:

$$\text{rank } \boldsymbol{\Lambda}_{PBH} \equiv \text{rank} \begin{bmatrix} \boldsymbol{A}_a - \lambda \boldsymbol{I} \\ \boldsymbol{G}_a \end{bmatrix} = n_s + n_p \tag{B.0.6}$$

or expanded and denoted with dimension for convenience:

$$\text{rank} \begin{bmatrix} \boldsymbol{A}_{n_s \times n_s} - \lambda \boldsymbol{I}_{n_s \times n_s} & \boldsymbol{B}_{n_s \times n_p} \\ \boldsymbol{0}_{n_p \times n_s} & (1-\lambda)\boldsymbol{I}_{n_p \times n_p} \\ \boldsymbol{G}_{n_d \times n_s} & \boldsymbol{J}_{n_d \times n_p} \end{bmatrix} = n_s + n_p \tag{B.0.7}$$

for all complex valued λ. We argue that detectability for the augmented system is equivalent to satisfaction of the following three criteria:

[1] J. P. Hespanha. *Linear Systems Theory.* Princeton University Press, Princeton, New Jersey, 2009.

1. The pair $(\boldsymbol{A}, \boldsymbol{G})$ must be detectable, i.e. rank $\begin{bmatrix} \boldsymbol{A} - \lambda \boldsymbol{I} \\ \boldsymbol{G} \end{bmatrix} = n_s$, where λ is an eigenvalue of $\boldsymbol{A}$ and $|\lambda| \geq 1$.

2. The system $(\boldsymbol{A}, \boldsymbol{B}, \boldsymbol{G}, \boldsymbol{J})$ must have no transmission zero equal to 1.

3. $n_d \geq n_p$

The argument, inspired by sensor fault detection in cybernetics [2], goes as follows:

For all $\lambda \notin$ eigenvalue of $\boldsymbol{A}_a$:

$$\text{rank} \begin{bmatrix} \boldsymbol{A}_{n_s \times n_s} - \lambda \boldsymbol{I}_{n_s \times n_s} & \boldsymbol{B}_{n_s \times n_p} \\ \boldsymbol{0}_{n_p \times n_s} & (1-\lambda)\boldsymbol{I}_{n_p \times n_p} \end{bmatrix} = n_s + n_p$$

if

$$\text{rank} \begin{bmatrix} \boldsymbol{A}_{n_s \times n_s} & \boldsymbol{B}_{n_s \times n_p} \\ \boldsymbol{0}_{n_p \times n_s} & \boldsymbol{I}_{n_p \times n_p} \end{bmatrix} = n_s + n_p$$

which is true if rank $\boldsymbol{A} = n_s$ or equivalently $\boldsymbol{A}$ has n_s distinct eigenvalues, which is follows from the last result in this appendix. For all $\lambda \in$ eigenvalue of $\boldsymbol{A}_a$, rank $[\boldsymbol{A}_a - \lambda \boldsymbol{I}] \neq n_s + n_p$. Specifically if $\lambda \neq 1$, the submatrix $[\, \boldsymbol{0} \quad (1-\lambda)\boldsymbol{I} \,]$ has n_p columns mutually independent and independent of the first n_s columns in $\boldsymbol{\Lambda}_{PBH}$. The first criterion implies:

$$\text{rank} \begin{bmatrix} \boldsymbol{A}_{n_s \times n_s} - \lambda \boldsymbol{I}_{n_s \times n_s} \\ \boldsymbol{G}_{n_d \times n_s} \end{bmatrix} = n_s$$

thus giving $\boldsymbol{\Lambda}_{PBH}$ rank $n_s + n_p$. In the case of $\lambda = 1$, which can be shown to always be an eigenvalue of $\boldsymbol{A}_a$, $[\, \boldsymbol{0} \quad (1-\lambda)\boldsymbol{I} \,]$ vanishes. The PBH test is then only fulfilled if:

$$\text{rank} \begin{bmatrix} \boldsymbol{A}_{n_s \times n_s} - \boldsymbol{I}_{n_s \times n_s} & \boldsymbol{B}_{n_s \times n_p} \\ \boldsymbol{G}_{n_d \times n_s} & \boldsymbol{J}_{n_d \times n_p} \end{bmatrix} = n_s + n_p \tag{B.0.8}$$

[2] S. M. Joshi, O. R. González, and J. M. Upchurch. Identifiability of additive actuator and sensor faults by state augmentation. *Journal of Guidance, Control, and Dynamics*, 37(3):941–946, 2014.

This is only true if 1 is not a transmission zero of the system $(\boldsymbol{A}, \boldsymbol{B}, \boldsymbol{G}, \boldsymbol{J})$. If it is not, the matrix above will have full rank, i.e. $n_s + \min(n_d, n_p)$, necessitating the third criterion $n_d \geq n_p$.

Furthermore, we claim in the following that the first criterion always will be satisfied in an ordinary structural dynamic system. Let $\alpha_j = a + bi$ be an arbitrary eigenvalue of $\boldsymbol{A}_c \Delta t$ and $\lambda_j = c + di$ be an arbitrary eigenvalue of $\boldsymbol{A}$. Let $\boldsymbol{D} = \text{diag}(\alpha_1 \dots \alpha_{n_s})$ advocating the eigen decomposition $e^{\boldsymbol{A}_c \Delta t} = \boldsymbol{P} e^{\boldsymbol{D}} \boldsymbol{P}^{-1}$, with $\boldsymbol{P}$ composed of the eigenvectors of $\boldsymbol{A}_c \Delta t$. The eigenvalue problem for $\boldsymbol{A}$ is:

$$\begin{aligned}
\det(\boldsymbol{A} - \lambda_j \boldsymbol{I}) &= 0 \\
\det(e^{\boldsymbol{A}_c \Delta t} - \lambda_j \boldsymbol{I}) &= 0 \\
\det(\boldsymbol{P} e^{\boldsymbol{D}} \boldsymbol{P}^{-1} - \lambda_j \boldsymbol{I}) &= 0 \\
\det(e^{\boldsymbol{D}} - \lambda_j \boldsymbol{I}) &= 0
\end{aligned}$$

which implies the intermediate result $e^{\alpha_j} = \lambda_j$ for singularity. We further look into the condition $|\lambda_j| < 1$:

$$\begin{aligned}
|\lambda_j| &< 1 \\
|c + di| &< 1 \\
|e^{a+bi}| &< 1 \\
|e^a(\cos b + i \sin b)| &< 1 \\
e^a \sqrt{\cos^2 b + \sin^2 b} &< 1 \\
e^a &< 1 \\
a &< 0
\end{aligned}$$

meaning $\boldsymbol{A}_c \Delta t$ must have strictly negative real part eigenvalues. We hereafter omit the positive factor Δt and inspect the eigenvalues β_j of $\boldsymbol{A}_c$:

$$\det(\boldsymbol{A}_c - \beta_j \boldsymbol{I}) = 0$$

$$\det \begin{bmatrix} -\beta_j \boldsymbol{I} & \boldsymbol{I} \\ -\boldsymbol{M}^{-1}\boldsymbol{K} & -\boldsymbol{M}^{-1}\boldsymbol{C} - \beta_j \boldsymbol{I} \end{bmatrix} = 0$$

$$\det(\beta_j \boldsymbol{M}^{-1}\boldsymbol{C} + \beta_j^2 \boldsymbol{I} + \boldsymbol{M}^{-1}\boldsymbol{K}) = 0$$

$$\det(\beta_j^2 \boldsymbol{M} + \beta_j \boldsymbol{C} + \boldsymbol{K}) = 0$$

recognized in the frequency domain as the damped eigenvalue problem associated with the complex solution of n_{DOF} conjugate pairs [3]:

$$\beta_j = -\zeta_j \omega_j \pm i\omega_j \sqrt{1 - \zeta_j^2}$$

where ω_j and ζ_j are the undamped natural frequency and critical damping ratio is mode j, respectively. $\zeta_j > 0$ and $\omega_j > 0$ for all j implies $a < 0$, which was to be shown. Therefore, all eigenvalues of $\boldsymbol{A}$ lie within the unit circle, automatically satisfying the first criterion.

[3] G. Lallement and D. J. Inman. A tutorial on complex eigenvalues. In *Proceedings - SPIE The International Society For Optical Engineering*, pages 490–490, 1995.

Appendix C

Calculation of ice load on Hanko channel marker

ISO19906[1] provides guidance for determining ice loads. The static global ice load expressed in Eq. (C.0.1) is an empirical formula based on full scale measurements and gives an upper bound.

$$F_G = C_R(\frac{h}{h_1})^n(\frac{w}{h})^m hw \tag{C.0.1}$$

where

C_R [MPa] is an ice strength coefficient

w [m] is the projected width of the structure

h [m] is ice sheet thickness

$h_1 = 1$ [m] is the reference thickness

$m = -0.16$ is a coefficient

$$n = \begin{cases} -0.5 + h/5 & \text{if } h < 1.0 \text{ m} \\ -0.3 & \text{if } h \geq 1.0 \text{ m} \end{cases}$$ is a thickness dependent coefficient

The Hanko channel marker has diameter $w = 0.8$ m. For a winter of moderate severity, the expected ice thickness is $h = 0.15$ m according to regional specific guidelines in

[1] *ISO/FDIS 19906:2010, Petroleum and natural gas industries - Arctic offshore structures*, 2010.

ISO19906. C_R is taken as 2.8 MPa, a conservative estimate. This yields $F_G = 626$ kN.

The code stipulates a simplified method for determining dynamic response. A sawtooth ice load function (see Fig. C.1) with frequency f, assumed equal to the natural frequency $f_n \leq 10$ Hz is applied. The amplitude of the fluctuating component, ΔF, is defined in Eq. (C.0.2). The peak value F_{max} can be set equal to global ice load F_G from equation Eq. (C.0.1). q is here set to 0.5 for simplicity.

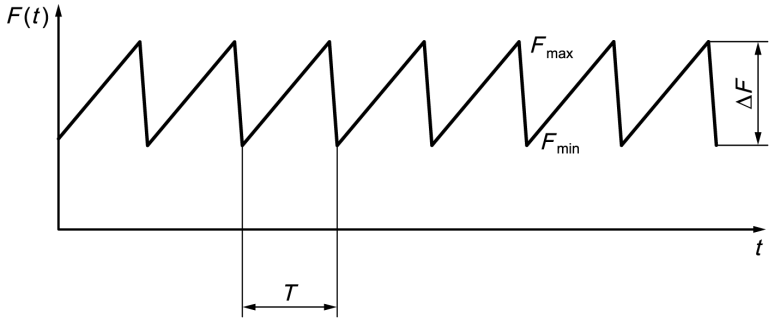

Key

t	time
F	ice action
F_{max}	maximum value of ice action
F_{min}	minimum value of ice action
ΔF	difference between maximum and minimum values of ice action
T	period of ice action

Figure C.1: Load history given in ISO19906.

$$\Delta F = qF_{max} = qF_G \tag{C.0.2}$$

This resembles idealized load conditions during *frequency lock-in*, a dynamic phenomena in ice-structure interaction. The corresponding ice sheet velocity v_t can be approximated as:

$$v_t = \frac{\dot{u}_{ca}}{\beta} \tag{C.0.3}$$

with $\dot{u}_{ca}$ as the structural velocity amplitude at ice level and $\beta = 1.4$ as a factor of proportionality[2].

[2]T. Kärnä. Simplified modeling of ice-induced vibrations of offshore structures. In *Proceedings of 16th International Symposium on Okhotsk Sea & Sea Ice*, pages 114–122, 2001.